

University of Montana

ScholarWorks at University of Montana

Graduate Student Theses, Dissertations, &
Professional Papers

Graduate School

2002

Modeling the impact of the direct emission of oxygenated organic species on biomass combustion smoke plume photochemistry

Sherri A. Mason

The University of Montana

Follow this and additional works at: <https://scholarworks.umt.edu/etd>

Let us know how access to this document benefits you.

Recommended Citation

Mason, Sherri A., "Modeling the impact of the direct emission of oxygenated organic species on biomass combustion smoke plume photochemistry" (2002). *Graduate Student Theses, Dissertations, & Professional Papers*. 9422.

<https://scholarworks.umt.edu/etd/9422>

This Dissertation is brought to you for free and open access by the Graduate School at ScholarWorks at University of Montana. It has been accepted for inclusion in Graduate Student Theses, Dissertations, & Professional Papers by an authorized administrator of ScholarWorks at University of Montana. For more information, please contact scholarworks@mso.umt.edu.

INFORMATION TO USERS

This manuscript has been reproduced from the microfilm master. UMI films the text directly from the original or copy submitted. Thus, some thesis and dissertation copies are in typewriter face, while others may be from any type of computer printer.

The quality of this reproduction is dependent upon the quality of the copy submitted. Broken or indistinct print, colored or poor quality illustrations and photographs, print bleedthrough, substandard margins, and improper alignment can adversely affect reproduction.

In the unlikely event that the author did not send UMI a complete manuscript and there are missing pages, these will be noted. Also, if unauthorized copyright material had to be removed, a note will indicate the deletion.

Oversize materials (e.g., maps, drawings, charts) are reproduced by sectioning the original, beginning at the upper left-hand corner and continuing from left to right in equal sections with small overlaps.

Photographs included in the original manuscript have been reproduced xerographically in this copy. Higher quality 6" x 9" black and white photographic prints are available for any photographs or illustrations appearing in this copy for an additional charge. Contact UMI directly to order.

**ProQuest Information and Learning
300 North Zeeb Road, Ann Arbor, MI 48106-1346 USA
800-521-0600**

UMI[®]



**Maureen and Mike
MANSFIELD LIBRARY**

The University of
Montana

Permission is granted by the author to reproduce this material in its entirety,
provided that this material is used for scholarly purposes and is properly cited in
published works and reports.

****Please check "Yes" or "No" and provide signature****

Yes, I grant permission

 X

No, I do not grant permission

Author's Signature: Sherril Mason

Date: 12/19/01

**Any copying for commercial purposes or financial gain may be undertaken only with
the author's explicit consent.**

**MODELING THE IMPACT OF THE DIRECT EMISSION
OF OXYGENATED ORGANIC SPECIES ON
BIOMASS COMBUSTION
SMOKE PLUME PHOTOCHEMISTRY**

by

Sherri A. Mason

B.S. University of Texas, Austin, 1995

presented in partial fulfillment of the requirements

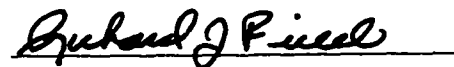
for the degree of

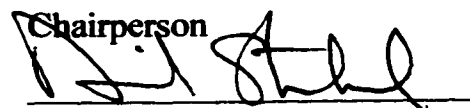
Doctorate of Philosophy

The University of Montana

September 2001

Approved by:



Chairperson


Dean, Graduate School

1-04-02

Date

UMI Number: 3034898

**Copyright 2002 by
Mason, Sherri Ann**

All rights reserved.

UMI[®]

UMI Microform 3034898

**Copyright 2002 by ProQuest Information and Learning Company.
All rights reserved. This microform edition is protected against
unauthorized copying under Title 17, United States Code.**

**ProQuest Information and Learning Company
300 North Zeeb Road
P.O. Box 1346
Ann Arbor, MI 48106-1346**

Modeling the Impact of the Direct Emission of Oxygenated Organic Species on Biomass Combustion Smoke Plume PhotochemistryDirector: Richard J. Field *R. J. F.*

Oxygenated volatile organic species (oxygenates), including: HCOOH, H₂CO, CH₃OH, HOCH₂CHO (hydroxyacetaldehyde), CH₃COOH, and C₆H₅OH, have recently been identified by FTIR measurements as a significant component of the direct emissions from biomass combustion. These oxygenates have not generally been included in the hydrocarbon-based initial emission profiles used in previous photochemical simulations of biomass combustion smoke plumes. We explore the effects of oxygenates on this photochemistry by using an established initial-emission hydrocarbon profile and comparing simulation results obtained both with and without addition of the above six oxygenates.

Simulations are conducted using a model developed to account for the horizontal expansion of a Lagrangian smoke plume. These simulations start at noon and are carried out for 30 hours. After an initial transient period during which [NO_x] falls rapidly, conditions within the oxygenated smoke plume are found to be strongly NO_x-sensitive, and the simulated final species profile is thus strongly dependent upon the $\Delta[\text{NO}]/\Delta[\text{CO}]$ initial-emission profile. Oxygenate addition results in very significant and complex effects on net O₃ production, as well as on the relative amounts of long-lived HO_x and NO_x reservoir species (H₂O₂, organic hydroperoxides, HNO₃, and PANs) that are mixed into the surrounding atmosphere. Oxygenates may either increase or decrease net O₃ production (depending upon the initial $\Delta[\text{NO}]/\Delta[\text{CO}]$). However, they always increase H₂O₂ and organic hydroperoxide production as a result of increased rates of radical + radical reactions. These effects spring largely from accelerated removal of NO_x from the smoke plume due to increased radical concentrations resulting both from photolysis of oxygenates (mainly CH₂O) and from their relatively high reactivity.

Urban environments represent a primary source of tropospheric NO_x and could, therefore, replenish NO_x resources within a smoke plume under the circumstance that the plume is advected into an urban airshed. Using the Montana fires of 2000 and the Missoula valley as a representative example, we investigate the effects of the mixing of an advected smoke plume with an urban environment. The production of O₃ is found to increase both within the urban airshed and within the biomass combustion smoke plume due to their mixing. This has important implications for regional and global tropospheric chemistry as the increase in O₃ production within an urban region can impact vegetative and human health, while the increase in the oxidizing capacity within the smoke plume leads to an increase in the production of global NO_x and HO_x reservoir species.

Acknowledgments

All things in nature are interconnected and interdependent. I would not be here, would not have completed this work, without the love, support, guidance and assistance of many others. I have been very blessed by all the family, friends and colleagues who have touched my life. It is to these people that I am indebted.

I extend my deepest gratitude to my mother (Susan Alexander) and father (James Mason) for giving me life and love, and instilling in me a passion for learning. I would also like to thank my 'additional' parents, Mary Mason and Monte Alexander, for giving my parents the love they deserve, and for guiding and advising me in my own growth. To my closest friend of many years, Christopher, I cannot express in words what is fully in my heart. I thank you for the love, support, and friendship you have so freely given. Life is full of transformations, but I hope we can always find support and friendship from one another; we have, after all, come together to create the most wonderfully amazing being in the world, our daughter, Francesca, who gives my life, and therefore my work, meaning.

In addition to my family and friends, I would like to thank Dr. Sasha Madronich at NCAR for his expertise and many helpful conversations, and the entire Chemistry Department at the University of Montana. All of the wonderful people in the department-from the secretaries (Bonnie, Gayle, Barbara, and Rosalyn), to the faculty, to the departmental chairs (Drs. George Woodbury and Ed Rosenberg)-help to make it a warm, friendly, homey place to be, and I am very thankful for the time I spent at UM.

Most importantly I would like to thank my committee-Professors Michael DeGrandpre, Leonid Kalachev, Donald Kiely, and Robert Yokelson-for their kindness, their interest, their time, and their never-ending assistance. And last, but certainly not least, I would like to thank my advisor, Professor Richard J. Field, for being more than just an advisor-for also being a friend and a father-figure-for giving me room to grow while making sure I didn't wander to far off track, and simply for allowing me to 'play in his sandbox.'

Table of Contents

List of Tables	vii
List of Figures	viii
Chapter 1. Introduction	1
Chapter 2. Biomass Combustion	
2.A. Introduction	3
2.B. The Process of Combustion	4
2.B.1. Heat Transfer	4
2.B.2. Stages of Combustion	5
2.B.3. Temporal Behavior of Fires and their Emissions	6
2.C. Fuels	10
2.C.1. Types of Fuels and Fires	10
2.C.2. Fuel Properties	11
2.C.3. Fuel Inventories	14
2.D. Biomass Combustion Smoke Plume Measurements	15
2.D.1. Sampling Procedures	17
2.D.2. Instrumental Techniques	17
2.D.3. Near-Source Measurements	20
2.D.4. Downwind Measurements	22
2.E. Summary	26
Chapter 3. The Troposphere	
3.A. Introduction	27
3.B. Gas-Phase Chemistry	30
3.B.1. Basic Tropospheric Photochemical Cycle	31
3.B.2. Nighttime Chemistry	34
3.B.3. Radical-Chain Termination	35
3.C. VOC/ NO _x Sensitivity	37
3.C.1. VOC-Sensitive Tropospheric Processing State	38
3.C.2. NO _x -Sensitive Tropospheric Processing State	39
3.C.3. VOC- to NO _x -Sensitive Transition	40
3.D. Radical Autocatalysis/ Positive Feedback	40
3.E. Summary	43
Chapter 4. Atmospheric Modeling	
4.A. Introduction	44
4.B. Types of Atmospheric Chemical Transport Models	45
4.C. Box Models	47
4.C.1. The Eulerian Box Model	48
4.C.2. The Lagrangian Box Model	50
4.D. Summary	52
Chapter 5. Photochemical Kinetics	
5.A. Introduction	53

5.B. Photolytic Reactions and their Rates	54
5.C. Chemical Reactions, their Rates and the Rate Law	56
5.D. Solving Chemical Ordinary Differential Equations	59
5.D.1. Introduction to Numerical Techniques	59
5.D.2. Gear's Method	59
5.D.3. The Jacobian Matrix and Sparseness	61
5.E. Summary	62
Chapter 6. The Model	
6.A. Description of Components	63
6.B. Modifications to the MM Numerical Solver	66
6.B.1. Biomass-Combustion Smoke-Plume Modeling	67
6.B.2. Urban Modeling	70
6.C. Summary	76
Chapter 7. Results of Smoke Plume Simulations	
7.A. Overview	77
7.B. Non-Diluting Smoke Plume	78
7.B.1. Effects on [O ₃] and [OH] Maxima	80
7.B.2. Effect on [HO ₂] Maxima	83
7.B.3. Summary of Non-Diluting Smoke Plume Simulations	85
7.C. Diluting Smoke Plume	86
7.C.1. Overall VOC/NO _x Sensitivity	90
7.C.2. Plume Evolution: VOC- to NO _x - Sensitive Transition	93
7.C.3. Decrease in NO _x Lifetime	95
7.C.4. Removal of NO _x	96
7.C.5. Increase in Radical Species	99
7.C.6. Increase in Hydroperoxides	101
7.C.7. Net O ₃ Production	101
7.C.8. Complex Effects on O ₃ and OH	103
7.C.9. Comparison to Measurements	104
7.C.10. Summary of Diluting Smoke Plume Simulations	107
Chapter 8. Results of Urban Simulations	
8.A. Basis	110
8.B. Urban Modeling	111
8.B.1. Standard (VOC-Sensitive) Urban Model	112
8.B.2. O ₃ Isopleth	114
8.B.3. Scaled (NO _x -Sensitive) Model	117
8.B.4. Summary of Urban Modeling	118
8.C. 'Urban plus Smoke' Modeling	118
8.C.1. Effect of Smoke on the Urban Airshed	119
8.C.1.a. Smoke Plume Time-of-Travel	120
8.C.1.b. Smoke Plume Time-of-Arrival	122
8.C.1.c. Summary of the Effect of Smoke on the Urban Airshed	124

8.C.2. Effect of the City on the Smoke Plume	124
8.C.2.a. Simulated Effects	126
8.C.2.b. Summary of the Effect of the City on the Smoke Plume	128
Chapter 9. Conclusions	
9.A. Summary	129
9.B. Biomass Combustion Smoke Plume Simulations	130
9.B.1. Conclusions	130
9.B.2. Further Work	130
9.C. 'Urban plus Smoke' Simulations	131
9.C.1. Conclusions	131
9.C.2. Further Work	132
9.D. Closing Remarks	132
Bibliography	134

List of Tables

Table 2.1. Near-Source Biomass Combustion Emission Measurements	21
Table 2.2. Comparison of Near-Source Biomass Combustion Emission Ratios	22
Table 2.3. Downwind Biomass Combustion Measurements.	23
Table 2.4. Measurements of the Downwind Evolution of Biomass Combustion Emissions	25
Table 3.1. Volume Percentage Composition of Dry Air	30
Table 6.1. Ambient Air Concentrations	69
Table 6.2. Deposition Rates Used in the Urban Model	72
Table 6.3. Scaling of VOCs for Urban Emission Speciation	73
Table 6.4. Hourly Car Counts for Six Sites across Missoula, MT.	74
Table 7.1. Non-Diluting Smoke Plume Initial Concentrations.	79
Table 7.2. Diluting Smoke Plume Initial Concentrations.	87
Table 7.3. Simulated Species Concentrations in an Aged, Diluting Smoke Plume.	88
Table 7.4. Effect of a Given Increase on Maximum Production	90
Table 7.5. Lifetime of NO _x	96
Table 7.6. Average Reaction Rates over a 30-Hour Simulation	98
Table 7.7. Average Concentrations over a 30-Hour Simulation	100
Table 7.8. Average O ₃ Destruction, O ₃ Production, and Net O ₃ Production Rates	102

List of Figures

Figure 2.1. Modified Combustion Efficiency versus Time	8
Figure 3.1. Temperature Variation with Altitude	27
Figure 3.2. Schematic of Basic Tropospheric Photochemical Reaction Cycle	32
Figure 4.1. Types of Atmospheric Chemical Transport Models	45
Figure 4.2. Schematic of Model Dimensionality	47
Figure 4.3. Schematic of Eulerian Box Model	48
Figure 4.4. Schematic of Expanding Lagrangian Box Model	51
Figure 6.1. Planetary Boundary Layer Height Diurnal Variation.	72
Figure 6.2. Diurnal Variation of Vehicular Emissions.	75
Figure 7.1. [O ₃] and [OH] Maxima for Non-Diluting, No Oxy, Smoke Plume Simulations	81
Figure 7.2. [O ₃] and [OH] Maxima for Non-Diluting, All Oxy, Smoke Plume Simulations	82
Figure 7.3. [HO ₂] Maxima for Non-Diluting Smoke Plume Simulations	84
Figure 7.4. Simulated [O ₃] Temporal Profile within Diluting Smoke Plume	89
Figure 7.5. Temporal Profile for Fraction of Radical Removal	92
Figure 7.6. Reaction Rate of HNO ₃ versus Radical + Radical Reactions.	94
Figure 7.7. Simulated [Total Hydroperoxide] Temporal Profile within Diluting Smoke Plume.	95
Figure 7.8. Component Reaction Rates of the Radical + NO _x Reactions.	97
Figure 7.9. Temporal Profiles for O ₃ Destruction Rates	103
Figure 8.1. Diurnal Variation of the Relative Source Strength	111
Figure 8.2. Diurnal Variation of Concentrations in the Standard Urban Model	112
Figure 8.3. O ₃ Isopleth Diagram	115
Figure 8.4. Isopleth Diagram for the Time of [O ₃] Maximum.	116
Figure 8.5. Diurnal Variation of Concentrations in the Scaled Urban Model.	117
Figure 8.6. Diurnal Variation of 'Smokey' Concentrations.	121
Figure 8.7. Urban [O ₃] Maximum as a Function of Smoke Plume Time-of-Arrival ..	123
Figure 8.8. Schematic of Model Scenario for the Effect of the City upon the Smoke Plume	125
Figure 8.9. Concentrations Profiles for the Effect of the City upon the Smoke Plume.	127

Chapter 1

Introduction

Biomass combustion has long been known to inject significant quantities of carbon dioxide (CO₂), carbon monoxide (CO), methane (CH₄), nitrogen oxides (NO_x = NO + NO₂), nonmethane hydrocarbons (NMHCs), and particulates into the atmosphere [*Crutzen and Andreae, 1990; Crutzen and Carmichael, 1993*]. However, recent ground-based and airborne Fourier transform infrared (FTIR) spectroscopic measurements have identified oxygenated organic compounds as being important additional components of biomass combustion smoke, at levels comparable to NMHCs [*Griffith et al., 1991; Yokelson et al., 1996a, 1996b, 1997, 1999a; Goode et al., 1999, 2000*]. Other studies have confirmed the original FTIR results [*McKenzie et al., 1995; Worden et al., 1997; Holzinger et al., 1999*]. The primary members of these oxygenated species [formaldehyde (CH₂O), methanol (CH₃OH), acetic acid (CH₃COOH), formic acid (HCOOH), hydroxyacetaldehyde (HOCH₂CHO), and phenol (C₆H₅OH)] have not generally been included as substantial initial components in previous smoke modeling efforts [*Chatfield and Delany, 1990; Richardson et al., 1991; Keller et al., 1991; Jacob et al., 1992; Crutzen and Carmichael, 1993; Jacob et al., 1996; Thompson et al., 1996; Chatfield et al., 1996; Koppmann et al., 1997; Mauzerall et al., 1998; Lee et al., 1998*], particularly at the levels observed in the FTIR measurements,

largely because they are not easily measured by traditional analytical methods. Thus we have conducted a series of simulations designed to elucidate the impact of directly emitted oxygenated organic compounds on the early photochemistry within a biomass combustion smoke plume. The results of these simulations lead us to further investigate the effect of a biomass combustion smoke plume mixing with an urban environment. Hence, we present here background, model development, and results for both of these primary simulation investigations.

We begin by presenting an overview of biomass combustion (chapter 2) and the troposphere (chapter 3). We then delve into the more specific areas of photochemical kinetics (chapter 5) and atmospheric modeling (chapter 4), including the presentation of the fundamental modeling approximations and differential equations that must be solved in each of the modeling scenarios (*i.e.*, the smoke plume and the urban environment). In chapter 6 we present an overview of the particular atmospheric model used in the work reported here, including a description of required modifications. Finally, we present the results of our modeling work in chapters 7 and 8; chapter 7 focusing on our fundamental modeling objective, that of simulating the impact of the direct emission of oxygenated organic species upon biomass combustion smoke plume photochemistry, while chapter 8 describes our secondary modeling inquiry of the effect of the mixing of a smoke plume with an urban environment.

Chapter 2

Biomass Combustion

2.A. Introduction

Fire and life form a necessary kind of symbiosis. Fire has been used by humans as a tool to manipulate the environment for over one million years. Today, fire is an integral part of increasingly common agricultural practices, such as conversion of forest to pasture, shifting cultivation, removal of dry savanna vegetation, weed control, domestic cooking and heating, and waste-burning methods [*Crutzen and Carmichael, 1993*]. Fire is also the main natural disturbance factor of nearly every ecosystem. Many ecosystems and some flora and fauna species have adapted so as to seize upon the properties of combustion; some species of trees, for example, have serotinous cones that open to release seeds only after violent heating [*Pyne, 1982*]. Fire breaks down the matter that organisms have assembled using captured sunlight, nutrients and water; its natural function is to recycle nutrients and thus it plays a significant role in the dynamic equilibrium between the production and decomposition of biomass. The burning of biomass is currently particularly prominent in the tropics and subtropics during the dry season (*i.e.*, July to October in the southern hemisphere and January to April in the northern hemisphere) [*Crutzen and Carmichael, 1993*], but, nevertheless, every day biomass in some part of the world is on fire.

We will begin our overview of biomass combustion by describing the process of combustion including a basic description of the temporal evolution of combustion emissions. The exact emission profiles are essentially determined by the available fuels (*i.e.*, their characteristics and properties), which will be the second topic of discussion. Finally, we conclude with a review of biomass combustion measurements including quantitative values, which will later be used for comparison to our own modeling results.

2.B. The Process of Combustion

2.B.1. Heat Transfer

Fire involves the process of combustion, that is, the rapid oxidation of a fuel accompanied by the production of heat and light. Combustion is a chain of chemical reactions and, in order to sustain it, more heat must be generated than is absorbed [Pyne, 1982]. The transfer of heat within the combustion process can occur in several ways [Fuller, 1991; Gaylor, 1974]. *Radiation* transmits heat through space by means of infrared rays emanating from a heat source. *Convection* is the circulating upward movement of a heated gas (or liquid) resulting from a decrease in density. Convection forms a vertically buoyant column of hot molecules that spread heat in any direction, depending upon the movement of the surrounding fluid. Biomass combustion smoke plumes often form these *convection columns*, due to the intense heating within the flaming front, causing a noticeable in-draft of surrounding air to replace the buoyant fire emissions. This draft accounts for the ‘roar’ associated with large, fast-burning fires [Gaylor, 1974]. Finally, *conduction* moves heat from one molecule to another by direct contact. In the case of wildland fires, this method of heat transfer is least effective due to wood being a poor conductor of heat.

2.B.2. Stages of Combustion

In the classic model for combustion, the process advances by three stages: a preheating phase, a period of flaming combustion, and a state of smoldering combustion [Fuller, 1991; Pyne, 1982; Gaylor, 1974]. During preheating, the fuel is being brought to its ignition point, which is roughly between 260°C and 430°C for most wildfire fuels [Gaylor, 1974]. The time required to reach the ignition temperature will depend on the characteristics of the fuel, *i.e.*, its size, moisture content and curing stage [Gaylor, 1974]. Two things happen during preheating: first, the fuel is dried, via the distillation of volatile substances, such as water; and second, the heat causes a thermal ‘cracking’ (pyrolysis) of the molecular bonds within the biomass (fuel), releasing gaseous pyrolysis compounds [Yokelson *et al.*, 1996a; Pyne, 1982]. With the ignition of these distillation and pyrolysis gases, the period of flaming combustion begins [Pyne, 1982]. Hence, flaming results from the burning of volatile gases, not from the direct combustion of the fuel itself. The emissions from flaming combustion tend to be highly-, if not completely- (*i.e.*, CO₂), oxidized.

Flaming combustion is an ephemeral state, varying with the fuel properties and the local fire environment. It advances as a wave front, and its energy release is the greatest of any stage in the combustion process [Pyne, 1982]. This second stage propagates the heat flux needed to sustain pyrolysis in advance of the flame front. What limits the duration of the flaming state is primarily the slowness of conduction through large diameter wood, which can slow the production of gases when the smaller, more-easily burned fuels are gone [Pyne, 1982]. Wood surfaces may be heated by radiation and convection and hence are readily pyrolyzed, but the interior of the larger diameter forest fuel can only be broken down by the

relatively ineffective transfer of heat by conduction. By the time conduction has allowed pyrolysis of the biomass interior, the flaming front has already passed and with it the energy needed to sustain flaming combustion. The retarding effect of conduction accounts for the large quantities of charred debris left after a major fire and serves as a reminder that not all fuel is available for combustion [Pyne, 1982].

Once the flaming front has passed, the remainder of combustion reverts to a smoldering state. Smoldering combustion involves two non-flaming processes: pyrolysis (as previously defined) and gasification (or glowing combustion). Gasification refers to the oxidation that occurs on the surface of the charcoal residue left from the flaming phase; the carbon burns but as a solid rather than as a gas [Fuller, 1991]. The chemisorption of O₂ onto the char is exothermic, supplying the energy to drive glowing combustion and the heat needed to pyrolyze adjacent fuel, leading to the formation of even more char. Nevertheless, smoldering combustion produces much lower temperatures than flaming, leading to the emission of less-oxidized (*i.e.*, CO) and even reduced (*e.g.*, CH₄ and NH₃) pyrolytic products. In the case of forest fires, the smoldering phase may be protracted but, regardless, the combustion of forest fuels is rarely total [Pyne, 1982].

2.B.3. Temporal Behavior of Fires and their Emissions

Free-burning fires are generally more complex than this simple model of combustion suggests. Specifically the concept of fire stages separated in time is less useful than a more general concept of fire processes which may coexist in time [Yokelson *et al.*, 1996a]. That is, within a burning area there are an infinite number of points, all of which will not be temporally in-phase with one another. Pyrolysis and glowing combustion occur in all stages

and, hence, pyrolytic and glowing emissions may be detected throughout the duration of a fire with a high degree of variability [Yokelson *et al.*, 1996a]. The large amount of heat released during flaming combustion may pyrolyze more fuel than during smoldering combustion, accounting for the peak often measured in pyrolysis products either before, during or immediately after the peak in flaming products [Yokelson *et al.*, 1996a]. However, the majority of pyrolysis products would normally be oxidized in the presence of vigorous flaming, and hence they have a higher probability of escaping the fire (to be detected in the smoke) during smoldering combustion. Thus, the quantity of pyrolysis products detected per unit fuel consumption is generally higher during times dominated by smoldering combustion [Yokelson *et al.*, 1996a].

For a given fire there may be an initial, transient period in which the emissions profile is dominated by the products of flaming combustion, such as CO₂ and NO_x (emitted primarily as NO), but glowing and pyrolysis emissions will also be evident. Eventually, the products of pyrolysis and glowing combustion, such as CO and NH₃, will be the most prevalent within the emission profile. However, at any point between these two extremes there is generally a transition period as the area behind the (initial) flaming front shifts towards intermittent pockets of smaller flames mixed with smoldering combustion. Hence throughout the lifetime of a given fire, the emissions will tend to be mixtures of products from both flaming and smoldering combustion, as well as unmodified pyrolysis compounds.

The oxidative efficiency of combustion decreases as the fire proceeds in time and can be monitored via the combustion efficiency (CE), or the percent of fuel carbon (FC) that is released as CO₂. Often the CE is approximated by the modified combustion efficiency (MCE)

given as $\Delta\text{CO}_2 / (\Delta\text{CO}_2 + \Delta\text{CO})$, where the Δ refers to the difference between the smoke-plume and the background concentrations (*i.e.*, the ‘excess’ concentration). Figure 2.1 illustrates the temporal behavior of MCE for two laboratory fires conducted by *Yokelson et al.* [1996a]. Under conditions dominated by flaming combustion, the fire burns with high (typically MCE \sim 99%) efficiency (see Figure 2.1a- first 10 min; Figure 2.1b- first 5 min). After the flames have completely died-out, the combustion efficiency decreases and is observed to range between 80 and 88 % until the fire ceases to burn, as illustrated at the end of both fires in Figure 2.1.

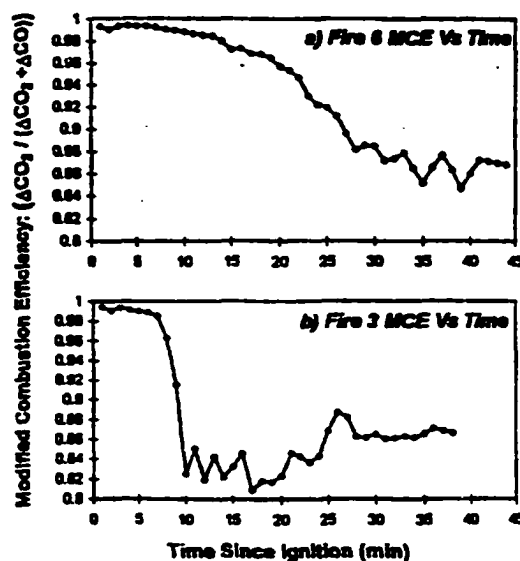


Figure 2.1 Modified combustion efficiency versus time for two laboratory fires, illustrating the concept of (coexisting) fire processes. (a) broadcast fire and (b) pine needle fire. [From *Yokelson et al.*, 1996a]

The midsection of Figure 2.1 a depicts the transition period in which there exist areas of both flaming and smoldering combustion and during which the emissions will contain products from all three combustion processes (flaming, smoldering and pyrolysis). This transition

period between purely flaming and purely smoldering combustion represents an important deviation from the simple, temporally-separated phases of combustion typically employed in biomass burning analysis [e.g., *Lobert et al.*, 1991].

In order to gain some insight into the temporal emissions from biomass burning it is helpful to understand how the constituents of biomass decompose upon heating, in the absence of flames. Vegetative material is composed of cellulose, hemicellulose, lignin, protein, nucleic acids, amino acids, and volatile substances [*Koppmann et al.*, 1997]. Hence, the elemental constituents of biomass are mostly carbon, hydrogen, oxygen, and nitrogen. Initial heating of biomass releases volatile distillation products, such as terpenes, and oxygenated pyrolysis products, such as methanol and acetic acid [*DeGroot et al.*, 1988]. Due to the emission of these oxygenated compounds the weight percent of carbon within the residual biomass increases, and leads to the formation of low temperature char, which is rich in aliphatic components [*Yokelson et al.*, 1996a]. Continued heating at increased temperatures releases light-weight hydrocarbons, such as methane, forming high temperature char, which is predominantly composed of aromatic components [*Lephardt and Fenner*, 1980]. The high temperature char participates in gasification, which supplies the necessary energy for the concurrent glowing combustion processes, producing, for example, CO and CO₂ [*Yokelson et al.*, 1996a]. CO and CO₂ are major products throughout all of these processes, initially due to simple pyrolysis, but later due also to gasification of char [*Lephardt and Fenner*, 1980]. These processes create the time variation of emissions due to pyrolysis and glowing combustion and also create the fuel that drives the turbulent, diffusion flames, which act to (further) oxidize these emission products.

2.C. Fuels

For any flame, fuel, oxygen, and heat must come together in the right mixture. Collectively, these make up the fire environment and their interrelationship is called the fire triangle [Fuller, 1991; Gaylor, 1974]. Eliminate any one of the three, and the flame goes out. For confined fire, these elements can be closely regulated and the properties of the fire rigidly prescribed. Free-burning, natural fire is vastly more complex. It responds to an ensemble of grossly arranged fuel complexes, it is propagated by a variety of erratic and turbulent thermal mechanisms, it must follow broad topographic configurations, and it must deal with traveling air masses superimposed over microclimates [Fuller, 1991]. Complete understanding and prediction of wildland fire behavior involves quantification and modeling of each of these components within the natural fire environment. However, investigation of the nature and fate of fire emissions requires only the characterization of the fuels.

2.C.1. Types of Fuels and Fires

Fuels are comprised of any organic matter (*i.e.*, any of the various components of vegetation), either live or dead, that occur on a site. Fuels are classified by location into ground, surface, and aerial fuels. *Ground fuels* include the decayed organic matter, called duff or humus, on the forest floor below the surface litter, in addition to buried debris [Fuller, 1991]. Fuels lying on top of the duff up to about 4 to 6 feet are classified as *surface fuels* [Fuller, 1991]. These include the *surface litter*, *e.g.*, dead needles, leaves, twigs, bark, cones, and small branches, as well as dead logs, stumps, large branches, herbaceous plants, shrubs and small trees. *Aerial fuels* consist of material in the tree or shrub canopy higher than 4 to 6 feet above ground [Fuller, 1991]. They are physically separated from the earth and from

each other, and air can circulate around the fuel particles [Gaylor, 1974]. Aerial fuels include snags, mosses, conifer needles, lichens, and tree branches and leaves.

Fires which burn through aerial fuels are known as *crown fires* [Fuller, 1991]. Fine fuels within the aerial category carry the fire, but crown fires are generally sustained by a *surface fire* that erupts into the canopies of forest fuels, often with violent and discontinuous surges [Pyne, 1982]. Surface fires are those which spread through surface fuels via a flaming front, followed by an area subject to smoldering combustion [Fuller, 1991]. Fires which propagate largely through creeping, burning ground fuels and surface litter, and sustained by glowing combustion are termed *ground fires* [Fuller, 1991]. Ground fires can be problematic in that they can go largely undetected, traveling via buried materials, to start a surface fire yards away from their source, and also because they can be difficult to extinguish, as ground fuels tend to repel water as they dry out [Fuller, 1991].

Within the ground, surface, and aerial categories, fuels are evaluated for their arrangement, size, compactness, continuity, and moisture content, *i.e.*, their properties. It is the properties of the fuel that will largely determine the profile of biomass combustion emissions [Lobert *et al.*, 1991].

2.C.2. Fuel Properties

The moisture content of a fuel is an important factor in determining its burning capability [Lobert *et al.*, 1991; Fuller, 1991; Gaylor, 1974]. The *fuel moisture* is calculated as the amount of water a fuel contains as a percentage of its oven-dry weight; hence, it can take on a value greater than 100 % [Hoffa *et al.*, 1999; Fuller, 1991]. The time required for a fuel to gain or lose 63 % of its moisture is known as the time-lag period [Fuller, 1991;

Anderson, 1982]. Temperature, humidity, precipitation, wind, season, solar flux, and topography all have a direct or indirect influence on the moisture content and time-lag period of a fuel at a given time [*Gaylor, 1974*]. Since small fuels (with a greater surface area to volume ratio) absorb moisture and dry out faster than larger fuels, moisture response can also be ascribed according to their *fuel size* (*i.e.*, fuel diameter). Fuels of less than a quarter of an inch in diameter (a.k.a *fine fuels*) are characterized by a 1-hour time-lag, while those between a quarter of an inch and 1-inch diameter are called '10-hour fuels' [*Fuller, 1991; Anderson, 1982*]. Mosses, lichens, and dry grasses, herbs and needles are examples of fuels belong to the former classification, with dead twigs and small branches exemplifying the second category. Larger dead branches between 1 and 3 inches in diameter are classified as 100-hour fuels, with fuels greater than 3 inches in diameter being characterized by a 1000-hour time-lag [*Fuller, 1991; Anderson, 1982*]. The degree to which a particular fuel will undergo complete combustion is also attributed to fuel size; smaller, fine fuels, such as dry grass, will tend to burn completely while larger fuels, such as logs, tend to leave unburned remains [*Ward et al., 1992*]. This is due to small fuels having a larger surface area which pyrolyze easier, is in contact with the air allowing them to dry out quicker (*i.e.*, shorter time-lag, as mentioned above), and which is also available to carry the fire.

While fuel moisture influences flammability, the amount of available fine fuel is a key factor in determining how vigorously a fire will burn [*Fuller, 1991*]. The oven-dry weight of all the fuel in an area defines the *fuel load* [*Fuller, 1991*]. Often the fuel load for an area is sub-classified according to time-lag fuels in order to account for the fuel sizes and moisture contents which comprise the total load [*Anderson, 1982*]. Intricately connected to fuel load

is the *fuel-bed depth*, the height of the fuel load above the forest floor. Grass and brush fuels rapidly increase in fuel-bed depth with increasing loading, while timber litter and logging slash only slowly increase in depth as the load is increased [Anderson, 1982]. Taken together, the fuel load and fuel-bed depth describe the total amount of fuel available.

Other very important properties of fuels that affect fire behavior are *fuel spacing* and *fuel continuity* [Fuller, 1991; Gaylor, 1974]. These both attempt to describe the distribution of fuels over an area, however fuel spacing does so on a more microscopic level than fuel continuity. The proximity of fuel particles to one another, *i.e.*, the fuel spacing, determines how well air circulates within the fuel and whether particles are close enough to ignite each other readily [Fuller, 1991]. Fuel continuity deals with fuel distribution on a more macroscopic level, that is, any break in accessible fuels tend to stop a fire and, hence, horizontal and vertical continuity of the fuels within an area are important to fire spread [Fuller, 1991]. Rock outcrops, bare areas, streams, and lakes interrupt the horizontal continuity of a fuel, while the vertical continuity is disrupted by regions without ladder fuels such as shrubs, saplings, or lower branches, limiting fires to the surface or ground.

Fuel geometry, moisture, size, bed depth, and load, as well as the percentage of dead material, are the primary characteristics of fuels within a given area which determine fire behavior and, hence, the combustion emissions [see *e.g.*, Hoffa *et al.*, 1999; Trollope *et al.*, 1996; Stocks *et al.*, 1996; Fearnside *et al.*, 1993; Ward *et al.*, 1992]. Fuel moisture and size can be further combined by classifying fuels according to their time-lag periods [Anderson, 1982]. One of the main missions facing forest managers and fire scientists is describing and quantifying the spatially and temporally varying fuel types and properties for a given area.

2.C.3. Fuel Inventories

There are an infinite number of combinations of fuel type, amount, size, shape, position, arrangement and moisture content. Since it is not possible to classify, *i.e.*, cut-down, separate, dry and weigh, all of the fuels throughout a given forest, more or less throughout the world, the characterization of fuel properties involves conducting fuel inventories which rely heavily upon statistically justified sampling procedures. These procedures include: destructive sampling; the use of volumetric equations and measured or tabulated vegetative densities, with subsampling for fuel moisture; and comparison of photographs to well-characterized areas. Within these procedures quantification of the fuels can occur via pre- and post-burn analysis, burned versus unburned, or approximation of total biomass using a 'typical' combustion factor.

Typically [see *e.g.*, Hoffa *et al.*, 1999; Trollope *et al.*, 1996; Stocks *et al.*, 1996; Fearnside *et al.*, 1993; Ward *et al.*, 1992] large areas (*i.e.*, National Forests or Parks), which are subject to natural or prescribed burning and available for scientific investigation, are broken-down into smaller plots, generally based upon uniform vegetation and natural boundaries. Transect lines are made through each plot to be studied and small, equivalent quadrats along the transect are marked. Usually, a fraction of the quadrats are used for pre-burn analysis, with the remaining employed for post-burn analysis. For each quadrat, fuel-bed depths are recorded and, in destructive sampling procedures, all the above-ground (unburned) vegetation (including saplings, but excluding tree-trunks) is cut and collected. Standing fuels (*i.e.*, trees) are counted and their diameters measured. In post-burn subplots, ash of known volume and weight is also collected. Collected biomass is separated according to various

categories, dried and weighed to determine fuel moisture content and fuel loading. By comparing sampling pre- and post-burning, the total fuel consumption for the plot as a whole can be estimated. The total fuel consumption, fuel loading by category, and fuel moisture content are fundamental properties in understanding biomass combustion emissions, as well as extrapolating emission measurements on individual fires to global emissions estimates [Yokelson *et al.*, 1999; Crutzen and Carmichael, 1993; Lobert *et al.*, 1991].

Rather than conducting on-the-ground inventories, fire managers, scientists and modelers may instead use photographs representing various typical or important fuel complexes [Fuller, 1991]. Inventory crews gather fuel data, such as the sizes of downed woody fuels and the depth of the duff, along transects from each photo point in order to characterize the exemplary fuel complexes [*e.g.*, Fischer, 1981]. These so-called 'Photo projects' are not expected to have the same precision as an actual ground inventory, however they are much less labor-intensive and adequately specify fuel properties within the precision of most fuel models [Fuller, 1991; Anderson, 1982]. Land managers match the fire site to the closest photo rather than conducting full-scaling sampling procedures.

2.D. Biomass Combustion Smoke Plume Measurements

Trace gas emissions from biomass burning make substantial contributions to atmospheric CO₂, CO, CH₄, NO_x, NMHCs, oxygenated organics, and particulates [Crutzen and Andreae, 1990]. Available evidence increasingly indicates that these emissions from biomass burning, in its various forms, represents a major perturbation of atmospheric chemistry [Crutzen and Andreae, 1990]. For example, biomass fires may be responsible for up to 20% of the recent atmospheric build-up of CO₂ and CH₄, both of which taken together

account for 80-95% of the fuel carbon (FC) and are greenhouse gases [*Crutzen and Carmichael, 1993*]. In addition, the photochemical oxidation of CO (~ 5-10% FC), HCs (~ 2% FC), and oxygenated organics (~ 1% FC), in the presence of NO_x (~ 0.5-2% of the fuel mass), produces ozone (O₃) (to be described in more detail in chapter 3). Tropospheric O₃ has both detrimental and advantageous effects. It is an oxidant which is damaging to vegetation and human health, and in the upper troposphere it is an important greenhouse gas. However, it is also the key precursor of the hydroxyl radical (·OH), which is the primary oxidant in the troposphere, responsible for the removal of reactive pollutants released into the atmosphere by anthropogenic and natural processes. Particulate matter emitted from fires (~ 1% FC) are highly effective catalytic pollutants, as well as condensation nuclei [*Seinfeld and Pandis, 1998*]. Additionally, they both absorb and scatter light, with the latter effect likely dominating and thus contributing to cooling of the atmosphere, possibly temporarily masking the effects of greenhouse gas buildup [*Penner et al., 1992*].

Due to the importance of the above-mentioned trace gases on the chemistry within the troposphere, it is necessary to quantify and elucidate the speciation within biomass combustion emissions in order to understand and, ideally, predict their influence upon local, regional, and global atmospheres. The analysis of representative emissions from fires is difficult due to the temporal variation of fire behavior, the high temperatures within smoke plumes, the reactive nature of many of the smoke constituents, and the extensive range of emitted species concentrations. Owing to the difficulty inherent in analyzing fire emissions a number of different instrumental techniques and sampling platforms have been employed.

2.D.1. Sampling Procedures

Aircraft probe large areas of potentially well-mixed integrated emissions, and can investigate secondary chemistry and transport [Goode *et al.*, 2000]. However, it is difficult to monitor a single fire continuously from beginning to end using airborne sampling, and specific knowledge of the fuels and fire types are difficult to correlate with measurements [Yokelson *et al.*, 1996a]. Ground-based measurements provide the opportunity for more detailed analysis of the fire and fuels [Delmas *et al.*, 1991], but may tend to incorrectly estimate the emissions in the convective column above the fire [Andreae *et al.*, 1988]. In order to monitor a more representative sampling of near-ground emissions, tower-based measurements have been employed [Ward *et al.*, 1992]. In addition to these field methods, there are a number of advantages to studying biomass fires in the laboratory. In situ studies allow burning under controlled conditions, where the chemical and physical properties of the fuel and environment may be known in detail, and the ability to monitor all of the smoke for the entire course of the fire so that emission factors for measurable species can be accurately determined [Yokelson *et al.*, 1996a]. Each of these above procedures intrinsically contain certain assets and liabilities, thus it is important to perform studies using each of these sampling platforms and intercompare results in order to obtain a more complete representation of actual fire emissions.

2.D.2. Instrumental Techniques

In addition to the obstacles faced in trying to sample representative fire emissions, there is also the challenge of choosing an appropriate measurement technique. The majority of biomass combustion emissions have been characterized via 'grab sampling' in which fire-

integrated (samples taken over the lifetime of the fire) emissions are drawn into canisters to be analyzed at a later time. Typically the analysis is conducted using gas chromatographic (GC) (possibly with flame ionization (FID) or electron capture (ECD) detection) and/or mass spectrometric (MS) techniques [see, for example, *Lobert et al.*, 1991; *Nance et al.*, 1993; *Mckenzie et al.*, 1995; *Hao et al.*, 1996; *Koppmann et al.*, 1997; and *Mauzerall et al.*, 1998]. Grab (point) sampling is open to emission profile misrepresentation due to temporal or spatial variations in species concentrations and, perhaps more importantly, due to the possible reaction of emitted gases both during the sampling procedure and in storage. More recently Fourier-transform infrared (FTIR) spectroscopy has been shown to be well-suited for biomass combustion emission analysis [*Griffith et al.*, 1991; *Yokelson et al.*, 1996, 1997, 1999; *Goode et al.*, 1999, 2000]. Both open-path (OP-FTIR) and airborne (AFTIR) FTIR methods allow simultaneous measurements of a wide variety of species, whose concentrations vary considerably, to be made pseudo-continuously in real-time so there is no need to take samples and little possibility of sampling- or storage-related artifacts, thus allowing reactive gases to be quantified. Additionally, measurements are integrated over the path length of the instrument, thereby averaging over small-scale local variations and reducing the susceptibility of recorded values to spatial variability.

The earliest work characterizing biomass burning emissions normally featured detection of CO₂, CO, and NO_x [*e.g.*, *Ryan and McMahon*, 1976]. The experimental laboratory fires of *Lobert et al.* [1991] (using GC/FID) and *Griffith et al.* [1991] were the first to characterize a wide variety of emission products of particular importance to atmospheric chemistry, including CO₂, CO, CH₄, NMHCs, and a variety of nitrogenous

species. Unfortunately, one suite of compounds not easily measured by the more traditional analytic methods, such as were used in these early works, are oxygenated organic compounds, such as aldehydes, alcohols, and acids. The pioneering work of *Griffith et al.* [1991] and *Yokelson et al.* [1996, 1997] (using the OP-FTIR technique) yielded results which compared well with measurements from more established analytic methods, but included the measurement of oxygenated organics, particularly CH₂O, CH₃COOH, and CH₃OH. In general, oxygenated compounds were found to be emitted at levels comparable to the much more heavily studied NMHCs.

The quantity and rate of species emissions from biomass combustion will depend upon the fuel being burned, the fuel loading (or, more specifically, the total fuel consumption) and the relative weighting of fire processes (*i.e.*, flaming and smoldering, glowing and pyrolysis). Plotting emission factors versus MCE can represent how well emissions vary with fuel type or fire combustion characteristics [*Yokelson et al.*, 1997]. Generally, a single, highly correlated, linear model fits the fire-integrated data for the emissions factors of smoldering and pyrolysis compounds versus MCE [*Yokelson et al.*, 1996, 1997, 1999; *Goode et al.*, 1999, 2000]. (Since MCE is an index of the relative amount of flaming versus smoldering combustion, as the combustion efficiency decreases, the emission rate of CO₂ and NO_x decrease, while the emission rate of more-reduced compounds increases). This trend is approximately the algebraic equivalent to the assumption that the compound is emitted at a constant ratio relative to CO, independent of MCE [*Yokelson et al.*, 1997]. Hence a compact ratio format is often used for reporting elevated concentrations within a smoke-plume. These fire-averaged emission (enhancement) ratios are expressed as $\Delta X/\Delta CO$, where ΔX is the

excess concentration of a compound either emitted directly by the fire or produced within the smoke-plume. An exception to this rule is the $[\text{NO}_x]$, which is usually reported as an excess ratio against CO_2 since they are both “flaming compounds.” Emission ratios are generally calculated from the slope of the least squares line in a plot of one set of excess mixing ratios versus the other.

2.D.3. Near-Source Measurements

The majority of biomass combustion smoke plume analysis has focused on characterizing the emissions produced directly from the fire. Table 2.1 summarizes some of these near-source measurements using the concise enhancement ratio format and encompassing a variety of instrumental techniques, as well as sampling platforms.

In order to use a single, consistent data set that accounts for the presence of oxygenated organic compounds the modeling work presented here uses initial concentrations within the biomass combustion smoke plume as recommended by *Yokelson et al.* [1996, 1997]. While we chose a specific data set, the enhancement ratios used herein compare well with the average of the measurements recorded in Table 2.1 (Table 2.2).

Table 2.1 Excess mixing ratios, as a percentage of CO (except CO, NO, and NO₂ which are given as percentages of CO₂), from published studies of measurements taken directly above or near the source of biomass fires^a.

Study	F/L ^b	Method	CO ^c	NO ^c	NO ₂ ^c	CH ₄	C ₂ H ₆	C ₃ H ₈	C ₄ H ₁₀	C ₂ H ₄	C ₂ H ₂	C ₂ H ₄	C ₂ H ₂	CH ₃ CHO	CH ₃ COOH	CH ₃ COH	C ₂ H ₅ OH	NH ₃ ^d	HCN ^d
Talbot <i>et al.</i> , [1988]	L	MIST	0.01	0.09
Lobert <i>et al.</i> , [1991]	L	GC/FID	7.3	0.15	0.05	9.11	0.68	1.21	0.01	0.15	0.49	1.55	1.13
Griffith <i>et al.</i> , [1991]	F	OP-FTIR	...	0.10	0.05	7.61	1.27	3.24	0.12
Nance <i>et al.</i> , [1993]	F	GC/MS/EC	5.70	0.73	...	0.35	0.42	1.30	...
Hurst <i>et al.</i> , [1994]	F	MI-FTIR	4.50	0.07	...	0.25	2.60	0.03
McKenzie <i>et al.</i> , [1995]	L	GC/MS	2.90	0.25	1.20	0.15	0.74	1.10	0.03
Hao <i>et al.</i> , [1996]	F	GC/FID	7.1	2.93	0.41	1.18	0.34	0.15	0.52
Yokelson <i>et al.</i> , [1996a]	L	OP-FTIR	...	0.18	0.05	10.86	1.42	1.71	0.98	...	1.60	0.73	2.32	1.61	...	1.91	0.44
Koppmann <i>et al.</i> , [1997]	F	GC/FID/EC	5.3	6.81
Worden <i>et al.</i> , [1997]	F	AES	1.55	...	3.10	...	4.30	...
Yokelson <i>et al.</i> , [1997]	L	OP-FTIR	6.55	0.45	0.98	0.17	0.65	2.33	1.08	...	1.09	2.20	1.98	0.84	2.66	0.65
Yokelson <i>et al.</i> , [1998]	L	OP-FTIR	...	0.13	...	6.43	...	1.49	1.55	0.58	1.12	1.21	...	1.42	...
Holzinger <i>et al.</i> , [1999]	L	CIMS	2.21	0.64	0.12
Goode <i>et al.</i> , [1999]	L	OP-FTIR	...	0.15	...	8.06	...	1.97	0.37	1.14	...	1.80	0.51	1.12	1.47	1.21	...	1.31	...
Yokelson <i>et al.</i> , [1999a]	CL1	AFTIR	8.2	7.70	2.60
Yokelson <i>et al.</i> , [1999a]	WF1	AFTIR	1.40	3.30	1.20	1.60	2.40	...	2.60	...
Yokelson <i>et al.</i> , [1999a]	CL2	AFTIR	7.9	11.40	...	1.50	2.60	0.85	1.80	2.10	...	1.10	...
Goode <i>et al.</i> , [2000]	B320	AFTIR	8.1	0.20	...	6.95	...	3.84	1.12	...	2.64	1.16	1.58	1.53	...	1.47	0.69
Goode <i>et al.</i> , [2000]	B280	AFTIR	9.2	6.01	...	2.49	0.27	...	2.07	0.58	1.65	1.32	...	2.57	...
Goode <i>et al.</i> , [2000]	B349	AFTIR	7.6	0.14	...	4.89	...	1.39	0.28	...	1.72	0.52	0.87	1.33	...	1.22	...
Goode <i>et al.</i> , [2000]	B309	AFTIR	9.1	0.13	...	5.45	...	1.88	0.25	...	1.78	0.77	1.15	1.40	...	1.22	...

^aThree dots indicate that the compound was below detection limits or it was not measured. Abbreviations are: OP-FTIR, open-path Fourier transform infrared spectroscopy; GC, gas chromatography; MS, mass spectrometry; EC, electron capture; MIST, mist chamber (see reference); FID, flame ionization detection; MI-FTIR, matrix isolation FTIR; AES, airborne emission spectrometer (operates in the infrared region); CIMS, chemical ionization MS; AFTIR, airborne FTIR.

^bHighly dependent on fuel nitrogen content.

^cFire location: L, laboratory; F, field.

Table 2.2 Comparison of enhancement ratios, as a percentage, used in the work presented here to the average of the near-source measurements reported in Table 2.1.

Enhancement Ratio	Average of Table 2.1	Value used herein
CO/CO ₂	7.76	7.00
NO/CO ₂	0.15	0.15
NO ₂ /CO ₂	0.05	0.04
NH ₃ /CO	2.03	2.15
HCN/CO	0.45	0.22
CH ₄ /CO	6.70	8.72
C ₂ H ₄ /CO	0.66	0.68
C ₂ H ₂ /CO	1.71	2.15
C ₂ H ₂ /CO	0.38	0.68
C ₃ H ₄ /CO	0.50	0.15
C ₃ H ₂ /CO	0.51	0.48
CH ₂ O/CO	1.98	2.15
CH ₂ (OH)CHO/CO	0.80	0.80
HCOOH/CO	0.79	0.80
CH ₃ COOH/CO	1.38	2.15
CH ₃ OH/CO	1.61	2.15
C ₆ H ₅ OH/CO	0.44	0.80

2.D.4. Downwind Measurements

The speciation and quantification of components within biomass combustion smoke plumes downwind of their source has been studied, in general, to a far lesser degree than the near-source emissions. The limited data which are available are summarized in Table 2.3, roughly ordered according to the reported plume age. Please note that values reported by *Mauzerall et al.* [1998] are consistently higher (by a factor of ~ 10) than would seem reasonable based on those reported by other sources. Nevertheless, we include these numbers in order to accurately present a review of previously reported values.

Table 2.3 Excess mixing ratios, as a percentage of CO or CO₂, from published studies of measurements taken downwind of a biomass combustion source^b.

Study	Plume		Emission as % of CO																					
	Age ^a	CO/CO ₂	O ₃	CH ₄	C ₂ H ₆	C ₂ H ₄	C ₂ H ₂	C ₃ H ₈	C ₃ H ₆	C ₄ H ₁₀	C ₄ H ₈	C ₄ H ₆	HCOOH	CH ₃ COOH	(CH ₃) ₂ O	H ₂ O	CH ₃ OOH	NO _x	PAN	HNO ₂	NH ₃			
Goode <i>et al.</i> , [2000] B280	1.5 hr	1.50	1.90	1.20	
Goode <i>et al.</i> , [2000] B309	1.7 hr	...	8.9	2.60	1.30	1.80	
Goode <i>et al.</i> , [2000] B280	2.1 hr	1.30	1.60	0.70	
Goode <i>et al.</i> , [2000] B309	2.3 hr	...	6.4	1.60	2.80	
Goode <i>et al.</i> , [2000] B309	2.4 hr	...	8.4	
Goode <i>et al.</i> , [2000] B280	2.8 hr	2.40	
Mauzerall <i>et al.</i> , [1998]	< 12 hr	4.74	15	16	0.75	0.69	0.42	0.24	0.12	0.95	1.47	1.65	...	1.18	0.25	0.52	0.60	0.22	
Mauzerall <i>et al.</i> , [1998]	< 1 day	2.32	32	37	0.59	0.13	0.34	0.10	...	0.18	4.31	10.65	1.03	6.80	1.55	0.38	0.75	0.58	
Andreane <i>et al.</i> , [1992]	< 1 day	...	14	2.80	1.20	2.80	1.60	
Andreane <i>et al.</i> , [1994]	< 1 day	...	5.6	
Andreane <i>et al.</i> , [1994]	< 1 day	...	6	
Wofsy <i>et al.</i> , [1992]	< 1 day	...	9.5	
Mauzerall <i>et al.</i> , [1996]	< 1 day	...	13	
Mauzerall <i>et al.</i> , [1998]	< 5 day	2.13	71	60	0.71	...	0.26	0.12	...	0.23	2.84	1.82	0.77	3.91	1.63	0.27	0.53	0.51	
Andreane <i>et al.</i> , [1994]	> 1 wk	...	46

^aEstimated age of smoke plume as reported in each reference.

^bThree dots indicate that the compound was below detection limits or it was not measured.

It is difficult to build any generalized trends based upon these data due in part to the sparsity of the measurements, but also because it is more meaningful to analyze the chemical transformations occurring within a specific individual plume rather than in collection of smoke plumes which span a variety of fuel types and processing conditions. Two studies [*Mauzerall et al.*, 1998 and *Goode et al.*, 2000] have attempted to monitor the chemistry occurring within an individual smoke plume by characterizing the concentration profiles at various locations downwind of the plume source. These specific studies have been separated from the above and are summarized according to the individual plumes and their ages (Table 2.4). Again we note that the values reported by *Mauzerall et al.* [1998] seem rather high, but will use them simply to develop some general trends in species concentrations versus plume age.

Based on Table 2.4, the enhancement ratios for individual NMHCs, CH₂O, NO_x and NH₃ tend to generally decrease as the plume ages due to the direct production of these species from the fire and the more rapid disappearance of these reactive species as compared to CO [*Mauzerall et al.*, 1998; *Goode et al.*, 2000]. Meanwhile, the enhancement ratio of O₃ seems to increase in time, presumably due to photochemical production of O₃ within the smoke-plume, in addition to photochemical loss of CO [*Mauzerall et al.*, 1998]. The $\Delta\text{NO}_y/\Delta\text{CO}$ ratio ($\text{NO}_y \approx \text{NO}_x + \text{PANs} + \text{HNO}_3$) tends to stay relatively constant, most likely sustained by redistribution of NO_x between its reservoir species, *e.g.*, PANs and HNO₃ [*Mauzerall et al.*, 1998]. The enhancement ratios of formic and acetic acid tend to generally increase downwind of the fire source, indicating a secondary, photochemical source of organic acids within the smoke-plume, in addition to their previously reported direct emission [*Goode et al.*, 2000].

Table 2.4 Excess mixing ratios, as a percentage of CO or CO₂, from measurements taken downwind of a specific, individual biomass combustion source^b.

Study	Plume Age ^c	Emission as % of CO																	
		CO/CO ₂	O ₃	CH ₄	C ₂ H ₆	C ₃ H ₈	C ₄ H ₁₀	C ₂ H ₄	C ₂ H ₂	CH ₃ CHO	HCOOH	CH ₃ COOH	(CH ₃) ₂ O	H ₂ O	CH ₃ OOH	NO	PAN	HNO	NH ₃
Mauzerall <i>et al.</i> , [1998]	< 12 hr	4.74	15	16	0.75	0.69	0.42	0.24	0.12	0.95	1.47	1.65	...	1.18	0.25	0.52	0.60	0.22	...
Mauzerall <i>et al.</i> , [1998]	< 1 day	2.32	32	37	0.59	0.13	0.34	0.10	...	0.18	4.31	10.65	1.03	6.80	1.55	0.38	0.75	0.58	...
Mauzerall <i>et al.</i> , [1998]	< 5 day	2.13	71	60	0.71	...	0.26	0.12	...	0.23	2.84	1.82	0.77	3.91	1.63	0.27	0.53	0.51	...
Goode <i>et al.</i> , [2000] B280	initial ^a	9.2	...	6.0	...	2.49	0.27	2.07	0.58	1.65	2.57
Goode <i>et al.</i> , [2000] B280	1.5 hr	3.00	1.50	1.90	1.20
Goode <i>et al.</i> , [2000] B280	2.1 hr	3.00	1.30	1.60	0.70
Goode <i>et al.</i> , [2000] B280	2.8 hr	1.80	2.40
Goode <i>et al.</i> , [2000] B309	initial ^a	9.1	...	5.5	...	1.88	0.25	1.78	0.77	1.15	0.13	1.22
Goode <i>et al.</i> , [2000] B309	1.7 hr	8.9	...	1.40	2.60	1.30	1.80
Goode <i>et al.</i> , [2000] B309	2.3 hr	6.4	...	1.60	1.60	2.80
Goode <i>et al.</i> , [2000] B309	2.4 hr	8.4

^aEstimated age of smoke plume as reported in each reference.

^bThree dots indicate that the compound was below detection limits or it was not measured.

^cSame as data in Table 2.1.

Likewise, hydroperoxide enhancement ratios generally increase during plume evolution, but in the absence of evidence for their direct production, indicating a net photochemical source within the smoke plume.

Models attempting to depict the chemistry occurring within biomass combustion smoke plumes should be able to reproduce these general trends. In addition to the general trends, modeled enhancement ratios should be comparable to the absolute values measured in these campaigns. We will address both of these comparisons in relation to the work reported here after our results are presented.

2.E. Summary

The purpose of this chapter is to present an introduction into the nature of biomass combustion, its properties, and the important factors which affect biomass combustion emissions. We have additionally presented a brief overview of the primary species emitted from biomass combustion, as well as providing a partial review of their reported emission factors. These emissions are released directly into the atmosphere, and the goal of the work presented here is to model the chemical transformations that occur within biomass combustion smoke plumes in order to gain some understanding of the impact of these emissions on the local, regional, and perhaps even global atmospheric environment. The purpose of the following four chapters is to introduce the fundamental concepts and tools required in order to perform this modeling task.

Chapter 3

The Troposphere

3.A. Introduction

The Earth's atmosphere is divided into four layers according to the variation of temperature with altitude (Figure 3.1).

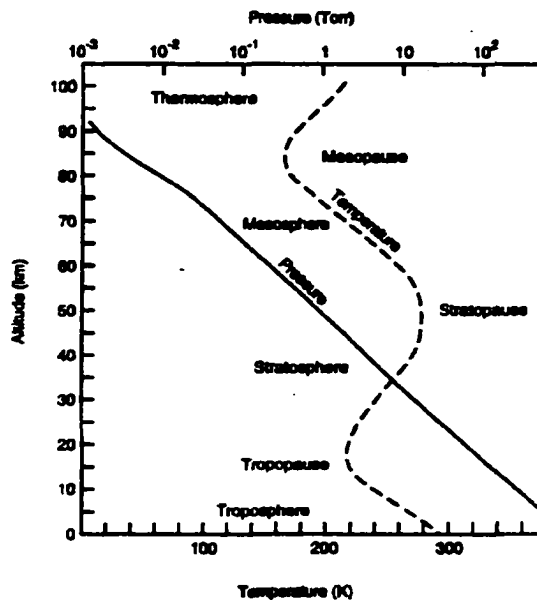


Figure 3.1 Typical variation of temperature with altitude at mid-latitudes as a basis for the divisions of the atmosphere. Also shown is the variation of total pressure with altitude (top scale, base 10 logarithms). [From Finlayson-Pitts and Pitts, 2000]

The lowest layer of the atmosphere, in which temperature generally decreases with increasing altitude, is called the troposphere and extends from the Earth's surface up to ~ 10 - 15 km,

depending upon latitude and time of year [*Seinfeld and Pandis, 1998*]. The height of the tropopause, which separates the troposphere from the next highest atmospheric layer, the stratosphere, is a maximum over the tropics and decreases moving towards the poles [*Seinfeld and Pandis, 1998*].

The troposphere can be subdivided into two layers: the planetary boundary layer (PBL), extending from the Earth's surface up to ~ 200 - 2000 m, and the free troposphere, extending from the PBL to the tropopause [*Jacobson, 1999*]. The PBL is that part of the troposphere that is directly influenced by the presence of the Earth's surface, and responds to surface forcings on the time scale of about an hour or less [*Stull, 1988*]. It is within this level of the atmosphere that the transport and dispersion of pollutants released at the surface is controlled [*Seinfeld and Pandis, 1998*]. The movement of air parcels within the PBL is influenced by the frictional drag of the surface and by energy transfer processes, such as conduction, radiation, advection and mechanical and thermal turbulence [*Jacobson, 1999*]. The combination of these effects and surface heating during the day causes the height of the PBL to increase, allowing air from the free troposphere to be mixed in. Conversely, at night radiative cooling leads to a decrease in the PBL height, thereby releasing air from within the boundary layer to be mixed into the free troposphere [*Fishman and Carney, 1984*]. Hence significant mixing occurs between the free troposphere and the PBL, but on time scales longer than mixing within the boundary layer itself [*Jacobson, 1999*].

The troposphere as a whole is, thus, a region of continual turbulence and rapid vertical mixing. This convective flow within the troposphere arises in part owing to the transfer of heat from the sun-warmed Earth to air in contact with the surface, which subsequently rises

due to decreases in its density [*Finlayson-Pitts and Pitts, 2000*]. As an air parcel adiabatically rises, its temperature decreases in response to the local pressure. While the troposphere accounts for only a small fraction of the atmosphere's total height (Figure 3.1), it contains about 80% of its total mass, including almost all of the atmosphere's water vapor [*Seinfeld and Pandis, 1998*]. This predominance of water vapor within tropospheric air parcels has the effect that as an air parcel rises and its temperature decreases, it can be accompanied by a substantial increase in relative humidity due to the strong dependence of saturation vapor pressure on temperature [*Seinfeld and Pandis, 1998*]. As a result, upward air motions of a few hundreds of meters can cause the air to reach saturation, and even supersaturation, leading to the formation of clouds. Interestingly, even though a rising air parcel cools due to changes in pressure, the condensation of water vapor can provide sufficient heating of the parcel to maintain its temperature above that of the surrounding air [*Jacobson, 1999*]. When this occurs, the air parcel remains buoyant and its upward movement is accelerated, leading to even more condensation [*Seinfeld and Pandis, 1998*]. Cumulus clouds are produced in this fashion, and the vertical convection associated with cumulus clouds is, in fact, another principal mechanism for transporting air from close to the Earth's surface to the free troposphere [*Seinfeld and Pandis, 1998*].

The strong vertical mixing within the troposphere, coupled to the temperature inversion above the tropopause (Figure 3.1) trapping air within the troposphere, allows it to act as a chemical reservoir distinctly separate from the stratosphere, such that chemical species with lifetimes less than ~ 1 year are destroyed within the troposphere itself [*Seinfeld and Pandis, 1998*]. Unreactive species and species with longer lifetimes, *e.g.*, N_2 , O_2 , CO_2 ,

CH₄ and Ar, tend to be well-mixed within the troposphere leading to globally sustained background concentrations and accounting for the majority of tropospheric composition by volume (Table 3.1) [Jacobson, 1999]. It is within the minor components of tropospheric gases, the so-called *trace gases*, that most tropospheric chemistry occurs.

Table 3.1 Volume percentage composition of dry air. ^avariable; ^batmospheric moisture varies. [From Whitten *et al.*, 1988].

Gas	% by Volume
N ₂	78.09
O ₂	20.94
Ar	0.93
CO ₂	0.03 ^a
He, Ne, Kr, Xe	0.002
CH ₄	0.00015 ^a
H ₂	0.00005
All others combined ^b (i.e., <i>trace gases</i>)	<0.00004

3.B. Gas-Phase Chemistry

The Earth's atmosphere is an oxidizing environment [Seinfeld and Pandis, 1998]. Hydrocarbons released from the surface eventually end up as carbon dioxide and water. Nitrogenous species are driven toward nitric acid, while sulfur-containing species cascade down their oxidative chain towards sulfuric acid. Thermodynamically, the oxidized products are generally lower in free-energy than their reduced counterparts, and this difference provides the driving force for their gas-phase oxidation. The formation of higher free-energy species, *e.g.*, O₃, may be photochemically driven by sunlight. Nevertheless, in general, chemical reactions need an input of energy to initiate the reaction process. This activation energy may be supplied thermally, but at normal atmospheric temperatures this is a slow process. Thus, in the atmosphere the energy of activation is often provided by the sun via photolytic reactions. Because the stratospheric ozone layer absorbs wavelengths less than

290 nm, only species which absorb lower-energy radiation are photochemically active in the troposphere [Finlayson-Pitts and Pitts, 2000]. For example, while the photolysis of molecular oxygen (O_2) provides the primary source of atomic oxygen [$O(^3P)$], and hence ozone (O_3), in the stratosphere, in the troposphere nitrogen dioxide (NO_2) photolysis (at wavelengths greater than 290 nm but less than 424 nm) fulfills that role via reactions 3.1 and 3.2 [Seinfeld and Pandis, 1998].



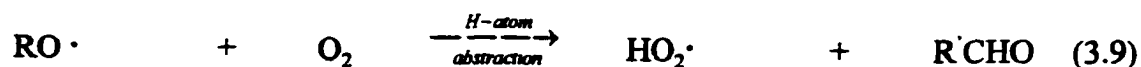
Just as the formation and destruction of O_3 is a well-known focus of stratospheric chemistry (*i.e.*, the ozone hole), the chemistry of O_3 is central to the troposphere as well [Crutzen, 1995].

The majority of photochemically active surface emission species can be categorized as nitrogen oxides ($NO_x = NO + NO_2$) or volatile organic compounds (VOCs). The term VOC is used to refer collectively to all hydrocarbon species (HCs), *i.e.*, ethane (C_2H_6), as well as oxygenated organic compounds, such as formaldehyde (H_2CO). NO_x emissions result from the oxidation of either atmospheric nitrogen (N_2) for industrial and vehicular sources, or fuel nitrogen in the case of biomass burning.

3.B.1. Basic Tropospheric Photochemical Cycle

Overall the gas-phase chemistry of the troposphere may be described as the photochemically driven, NO_x -catalyzed oxidation of carbon monoxide (CO) and VOCs with the coproduction of O_3 (Figure 3.2).

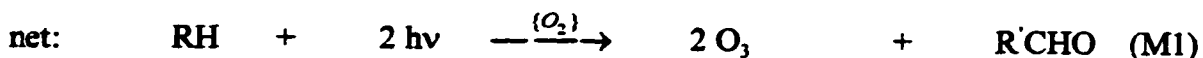
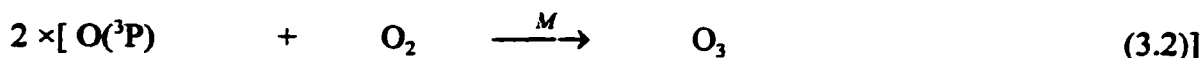
The higher-order oxy radical species (reactions 3.7 and 3.8) generally react with O₂ leading to the production of *additional* HO₂[·] and RO₂[·], as well as to the formation of an oxygenated organic compound, *e.g.*, reactions 3.9 and 3.10.



Carbonyl compounds (Reaction 3.9) add to the suite of VOCs that can be attacked by [·]OH, and in fact enhance the photochemical cycle (as discussed below), while the ‘fresh’ peroxy radicals are now available to convert more NO to NO₂. The subsequent photolysis of NO₂ regenerates NO and leads to the production of O₃ (Reactions 3.1 and 3.2).

The generalized mechanism presented above thus propagates via a free-radical chain in which VOCs are converted into more oxidized products. In the oxidation process multiple NO-to-NO₂ conversions occur, eventually regenerating [·]OH (and thus completing the photochemical cycle [Figure 3.2]), and leading to the production of O₃. For example,





Thus the propagation steps of the tropospheric photochemical reaction cycle oxidize hydrocarbons via a series of intermediate oxygenated organic species, to eventually form CO₂. The cycle being initiated and perpetuated through radical species.

Free radicals are introduced into the troposphere via, mainly photolytic, radical initiation steps [Seinfeld and Pandis, 1998]. For example, ·OH is primarily introduced via the photolysis (at wavelengths shorter than 325 nm) of O₃, in the presence of water, (reactions 3.11 and 3.12).



Since ·OH initiates most oxidative tropospheric reaction pathways, and because it is formed from the photolysis of O₃, the availability of O₃ is generally considered to determine the oxidizing capacity of the troposphere [Seinfeld and Pandis, 1998].

3.B.2. Nighttime Chemistry

At night, when photolytic free radical sources are not available, the principal oxidant of VOCs is the nitrate radical (NO₃·), often rivaling in magnitude the loss by reaction with ·OH during the day [Finlayson-Pitts and Pitts, 2000]. The prerequisite for NO₃· production is the simultaneous presence of NO₂ and O₃ in the same airmass, as the only primary source of NO₃· is via reaction 3.13 [Seinfeld and Pandis, 1998].



NO_3^\cdot is also formed via its equilibrium with N_2O_5 (reaction 3.14), an important feature of NO_3^\cdot chemistry.



During the day, NO_3^\cdot rapidly photolyzes (reactions 3.15 and 3.16), thereby restricting its chemistry to night,



and reacts with NO (reaction 3.17),

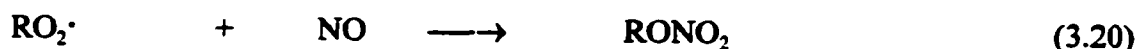


sufficiently rapidly that NO and NO_3^\cdot cannot coexist at mixing ratios of a few parts per trillion (ppt) or higher [Seinfeld and Pandis, 1998]. For typical daytime conditions, the maximum NO_3^\cdot mixing ratio will be 0.6 ppt. At nighttime, however, when NO concentrations drop near zero due to reaction with O_3 , and assuming the concurrent presence of sufficient quantities of both NO_2 and O_3 , the NO_3^\cdot mixing ratios can reach 100 ppt.

3.B.3. Radical-Chain Termination

Radical species, as well as NO_x , are removed (in many cases only temporarily) from the photochemical cycle via termination reactions, e.g., reactions 3.18- 3.22.





The first three reactions consume NO_x , as well as radical species, and will be referred to here as ‘Rad + NO_x ’ termination reactions, while the last two are radical-recombination reactions and will be referenced as ‘Rad + Rad’ termination reactions [*Kleinman, 1994*].

Rad + NO_x and Rad + Rad reactions were introduced above as consuming or removing radicals and NO_x from the photochemical cycle. However, they are also important because most of the products formed in reactions 3.18-3.22, and other similar reactions, are long-term pollutant reservoir species; they allow transport of photochemically-active species away from local events and into regional, possibly even global, atmospheres. For example, nitric acid (HNO_3) and peroxyacyl nitrates (PANs), formed in reactions 3.18 and 3.19, sequester NO_x , which can be released photochemically or thermally, respectively [*Seinfeld and Pandis, 1998*]. The hydroperoxide products (H_2O_2 and ROOH) of reactions 3.21 and 3.22 are reservoirs of HO_x ($\cdot\text{OH} + \text{HO}_2\cdot$), which may be released by photolysis, reaction with $\cdot\text{OH}$ or, for some peroxides, dissolution into cloud droplets [*Seinfeld and Pandis, 1998*]. Thus, on a local scale, termination reactions remove radicals, and sometimes also NO_x , from the photochemical cycle, but they also allow long-range transport of these photochemically important species, possibly to be reintroduced into the atmosphere at a later time. Hence,

while *NO_x-removal* will be used to refer to the local effect, the possible larger-scale implications of this process should not be overlooked.

The dominant termination reactions are determined by the relative availability of *NO_x* and radical species and, under limiting circumstances, are characteristic of the atmospheric processing state, either *VOC-* or *NO_x-sensitive* [Kleinman, 1994], as described below.

3.C. VOC/ *NO_x* Sensitivity

Three decades of tropospheric photochemical modeling have revealed the nonlinear relationship between *O₃* formation and its two primary precursors, *NO_x* and VOCs [Sillman, 1999, and references therein]. From these studies, including analysis of the underlying chemical equations [Kleinman, 1997], the troposphere has been found to have two fundamentally different processing states: one in which the rate of *O₃* formation increases with increasing [*NO_x*] and is largely independent of [*VOC*], known as *NO_x-sensitive (-limited)* or *low-NO_x*, and another in which the rate of *O₃* production decreases with increasing [*NO_x*] but increases with increasing [*VOC*], termed *VOC-sensitive (-limited)*, *NO_x-saturated*, or *high-NO_x* [Kleinman, 1994; Sillman, 1999, and references therein]. These two states reflect basic differences in the dominant photochemical reaction pathways and are directly related to the relative availability of *NO_x* and radical species. Tropospheric photochemical models are often run under differing constant emission fluxes of VOC and *NO_x* (occasionally keeping the VOC/*NO_x* ratio constant) in order to determine which processing state a particular simulated event represents.

The formation of *O₃* in the *VOC-* and *NO_x-sensitive* states of the troposphere can be viewed as a stoichiometry problem based upon the *NO*-to-*NO₂* conversion (reactions 3.6-

3.8). The majority of NO_x emissions into the atmosphere are in the form of NO [Finlayson-Pitts and Pitts, 2000]. However, O_3 production results from the photolysis of NO_2 (reactions 3.1 and 3.2). As such, in order to obtain net O_3 formation NO must be converted to NO_2 by a molecule other than O_3 itself. It is a primary role of peroxy radical species ($\text{HO}_2\cdot$, $\text{RO}_2\cdot$, and $\text{RC(O)O}_2\cdot$) to perform this conversion through reactions such as 3.6-3.8, and in these reactions either reactant may be in excess.

3.C.1. VOC-Sensitive Tropospheric Processing State

In the *VOC-sensitive (high- NO_x)* tropospheric state the emission of NO_x exceeds the production (via the photochemistry outlined in the previous section) of radical species. Radicals are thus rapidly removed from the system, via the $\text{Rad} + \text{NO}_x$ reactions, limiting their availability to perform the NO -to- NO_2 conversion and inhibiting O_3 production. Hence an increase in $[\text{NO}_x]$ causes a decrease in $[\text{O}_3]$ due to both radical destruction and reaction of O_3 with NO (reaction 3.23).



Conversely, an increase in $[\text{VOC}]$, increases peroxy radical production via reaction with $\cdot\text{OH}$ (reactions which compete with reaction 3.18) and therefore increases O_3 formation. Overall the *VOC-sensitive* state is characterized by a decrease (as compared to the *NO_x -sensitive* state) in the oxidizing capacity of the troposphere due to reduced radical species concentrations [Sillman, 1999]. This leads to the accumulation of primary pollutants such as NO_x and VOCs (as alternate removal processes are slow), and a suppression of hydroperoxide formation via the $\text{Rad} + \text{Rad}$ reactions [Kleinman, 1994]. The diminished role of the $\text{Rad} + \text{Rad}$ termination reactions, as well as the abundance of NO_x , leads to the

dominance of $\text{Rad} + \text{NO}_x$ termination reactions in the removal of radical species from the photochemical cycle under *VOC-sensitive* conditions [Sillman, 1990; Poppe et al., 1993]. Urban atmospheres are typically found to be VOC-sensitive due to the significant source of NO_x from vehicular, as well as industrial, emissions.

3.C.2. NO_x -Sensitive Tropospheric Processing State

The *NO_x -sensitive (low- NO_x)* tropospheric processing state occurs under stoichiometric conditions (in reactions such as 3.6-3.8) opposite to those of the *VOC-sensitive* state. Rather than the NO -to- NO_2 conversion reactions being limited by radical availability, in the *NO_x -sensitive* state O_3 production is limited by the availability of NO_x itself. Under such conditions O_3 formation increases with increasing $[\text{NO}_x]$ because radical species are readily available to convert NO to NO_2 [Kleinman, 1994]. Previous studies also have concluded that O_3 production in this state is largely independent of $[\text{VOC}]$, presumably due to a saturation effect in which an increase in radical species, which are already more available than NO_x , does not lead to an increase in NO -to- NO_2 conversion rate and hence little effect on O_3 production [Sillman, 1999]. (However, the simulations presented here illustrate that net O_3 production can sometimes be VOC-dependent under NO_x -sensitive conditions owing to VOC-induced removal of NO_x leading to reductions in both O_3 destruction and production).

The *NO_x -sensitive* state is, thus, characterized by abundant radical species, which rapidly remove NO_x via $\text{Rad} + \text{NO}_x$ termination reactions, and increased hydroperoxide concentrations due to ‘excess’ radicals reacting among themselves in $\text{Rad} + \text{Rad}$ termination reactions. Under certain conditions, the availability of excess radical species can even lead

to the dominance of the Rad + Rad termination reactions for removal of radical species from the photochemical cycle. However, it is important to mention that while in general *VOC-sensitive* conditions are dominated by the Rad + NO_x termination reactions and *NO_x-sensitive* conditions by the Rad + Rad termination reactions, there are circumstances under which the troposphere is in an *NO_x-sensitive* state but radical removal by the Rad + NO_x termination reactions is still favored over the Rad + Rad reactions [Kleinman, 1994].

3.C.3. VOC- to NO_x-Sensitive Transition

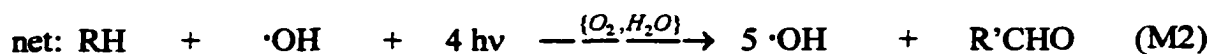
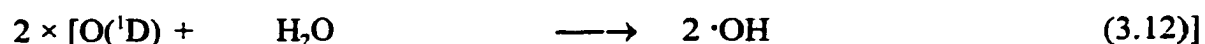
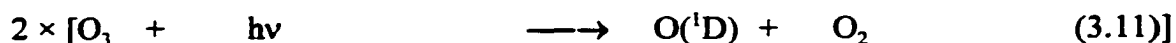
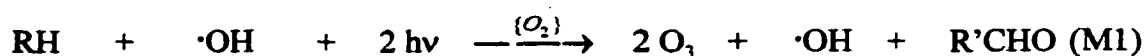
It has frequently been observed in previous VOC/NO_x models that urban plumes undergo a transition from *VOC-sensitive* to *NO_x-sensitive* photochemical processing as the plume moves downwind from the city source. That is, urban environments tend to be NO_x-rich due to vehicular and industrial emissions; however, rural environments tend to be characterized by fairly high VOC-to-NO_x ratios owing to the relatively rapid removal of NO_x from distant sources as compared to VOCs. The photochemical removal of NO_x from urban plumes is generally also coupled to the absence of strong, rural NO_x sources, as well as to the dilution of the plume by background concentrations [Sillman, 1999]. The depletion of NO_x concentrations within the urban plume cause the relative ratio of NO_x to radical species production to shift, leading to the transition between VOC- and NO_x-sensitive chemistry.

3.D. Radical Autocatalysis/ Positive Feedback

The inclusion of oxygenated organic species into a tropospheric model in which they had previously been ignored can have a significant impact upon the predicted photochemical processing. This influence is associated with two features of tropospheric gas-phase chemistry: radical-chain initiation and autocatalysis. Oxygenated organic compounds differ

from HCs in that their oxidation proceeds not only via $\cdot\text{OH}$ attack, but also through direct photolysis, especially for aldehydes. Thus oxygenated organic compounds act as an additional direct source of radical species by providing added photolytic radical-initiation steps.

Autocatalysis is a positive feedback process in which a chemical species becomes involved in a cycle whereby it catalyzes its own formation. Recall from the generalized mechanism presented earlier that in the propagation steps of the tropospheric reaction cycle (assuming the presence of high enough concentrations of NO_x) multiple NO-to- NO_2 conversions may occur for each oxidative step of a VOC (reaction scheme M1). Each of these NO_x conversions require an associated transformation, but not termination, in RO_x ($=\cdot\text{OH} + \text{HO}_2\cdot + \text{RO}_2\cdot + \text{RC}(\text{O})\text{O}_2\cdot$), implying that the general tropospheric cycle may, in fact, be autocatalytic in radical formation. This radical amplification can be visualized by completing the cycle of M1 to include the $\cdot\text{OH}$ -formation reactions:



An equivalent reaction cycle can be written based upon any of the general VOC-oxidation initiation steps (reactions 3.3- 3.5) and/or for the amplification of peroxy radicals, *e.g.* $\text{HO}_2\cdot$, instead of the $\cdot\text{OH}$ radical. The overall stoichiometry of M2 is autocatalytic in that one

radical leads to the production of more than one radical at a rate that is proportional to the concentration of the radical itself, indicating that the generalized tropospheric oxidation cycle may be autocatalytic under conditions where M1 is rapid as compared to reaction 3.18. The reaction cycle M2 is in fact an idealized maximum radical-multiplication scheme. Tropospheric chemistry is exceedingly complex in that there are many competing reactions occurring simultaneously, and the rate of change for any particular species is intricately coupled to the concentrations of other species. Hence, the reaction scheme M2 does not occur in isolation, *i.e.*, $\cdot\text{OH}$ radicals, as well as some O_3 , are lost due to reaction with NO_x , and each step in the cycle depends upon the relative concentrations of O_3 , radicals, NO_x and VOCs. As written, then, it is not completely realistic. However, the purpose in presenting this one possible reaction pathway is simply to illustrate that the general tropospheric photochemical cycle has the ability to be autocatalytic in radical production (albeit mediated by O_3), an important contingency in the modeling work presented here. Note also that the photolysis of O_3 to yield $\cdot\text{OH}$ (reactions 3.11 and 3.12) is both rate-determining and initiating for M2. Thus this chemistry appears as an autocatalysis in $[\text{O}_3]$, which *a priori* controls the oxidative capacity of the troposphere.

A similar positive feedback loop involving the $\cdot\text{OH}$ -mediated rate $d[\text{O}_3]/dt \propto [\text{VOC}][\text{O}_3]/[\text{NO}_2]$ has been proposed as a critical link in the nonlinear phenomena associated with tropospheric chemistry (*e.g.*, the high- NO_x / low- NO_x chemistry discussed earlier) and in oscillatory tropospheric chemical models [Kleinman, 1997; Field, *et. al.*, 2001; Tinsley and Field, 2001]. Both the positive feedback loop presented here and those proposed previously indicate that, providing there is sufficient NO_x available, an increase in VOC-loading will lead

to an increase in radical species production through the basic photochemical cycle itself. This effect is expected to be even more pronounced when the increase in VOC-loading results from the inclusion of oxygenated organic compounds since they tend to be more reactive with $\cdot\text{OH}$ in general than are HCs [Finlayson-Pitts and Pitts, 2000].

3.E. Summary

The goal of this chapter is to introduce the troposphere, describe some of its basic properties, and give an overview of the fundamental, and yet very complex, chemistry that occurs within it. As the lowest level of the atmosphere, it is the chemistry of the troposphere which is directly affected by surface emissions, such as biomass combustion and urban pollution. Modeling tropospheric chemistry requires the ability to mathematically describe the possible chemical transformations, as well as any physical processes which influence reactive species availability. The following two chapters aim to introduce the fundamental concepts upon which such mathematical models are based, as well as providing some details specific to the work presented here. Chapter 6 describes additional, more specific information on the exact modeling software employed in our research. Please note that in this chapter we attempted to explicitly indicated radical species (*e.g.*, $\text{HO}_2\cdot$) but from this point forward will avoid this precise, dot notation.

Chapter 4

Atmospheric Modeling

4.A. Introduction

The atmosphere is an extremely complex system in which numerous physical and chemical processes occur simultaneously. A major goal of the atmospheric sciences is to understand how these coincident processes lead to the behavior of trace atmospheric constituents on both the spatial and temporal levels. Atmospheric measurements give us insight into the instantaneous atmospheric conditions at a particular place at a particular time, but do not provide insight into the governing atmospheric processes that lead to the measured properties. Laboratory and theoretical studies yield specific atmospheric parameters and processes, but do not imply an understanding of the system as a whole. It is mathematical computer models which combine the theoretical equations of the individual atmospheric processes and impart an understanding of their interactions as a whole; they provide the causal relationship between emission fluxes, meteorology, chemical transformations and removal processes, and ambient concentrations.

There are of course many different types of models [*Seinfeld and Pandis, 1998*]. There are physical models which attempt to simulate a real area and/or event by building a small-scale replica of the situation. There are statistical models which use past data, along

with current measurements, as variables in a statistical analysis to predict near-future conditions. But both of these have limited usefulness because they are not based on a fundamental description of the atmosphere in terms of both its physical and chemical processes. In order to obtain an understanding of the interdependent relationships occurring in the atmosphere we need a mathematical model which is based upon these fundamental equations, a so-called atmospheric chemical transport model (ACTM).

In this chapter we will describe the different types of ACTMs including introducing the concept of their dimensionality. We will then detail the specific modeling approaches used within the work present here, focusing upon the derivation of the fundamental differential equations which describe the temporal evolution of species concentrations.

4.B. Types of Atmospheric Chemical Transport Models

There are two approximations under which ACTMs have been designed (Figure 4.1) [Seinfeld and Pandis, 1998].

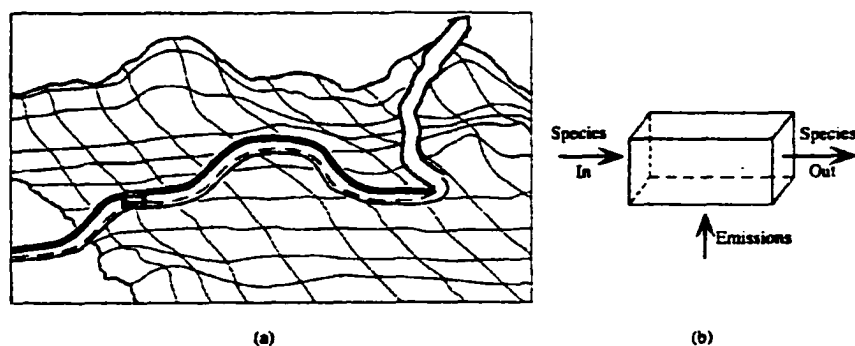


Figure 4.1 Schematic depiction of (a) a Lagrangian model and (b) an Eulerian model. [From Seinfeld and Pandis, 1998].

A *Lagrangian* model moves with the local wind so as to simulate changes in the chemical composition of a given air parcel(s) as it is advected through the atmosphere (Figure 4.1a).

As the air parcel moves, species emissions are allowed to enter and leave the parcel through its base, but otherwise there is, in general, no mass exchange between the parcel and the surroundings (unless the size of the air parcel is permitted to change in time). Since the air parcel moves continuously, the Lagrangian model actually simulates species concentrations at different locations as a function of time [*Finlayson-Pitts and Pitts, 2000*]. The Eulerian approach differs from the Lagrangian in that the modeling framework remains fixed in space (Figure 4.1b). As such, an Eulerian model describes the flux and chemical behavior of an air mass moving through of an array of stationary computational cells, which cover the entire modeling domain. Species enter and leave each cell through the walls (either to exchange between cells or between a given cell and the surroundings) with additional mass exchange, due to emission and deposition, through the cell base (Figure 4.1b). The Eulerian model simulates species concentrations at all locations as a function of time [*Seinfeld and Pandis, 1998*]. In the modeling work presented here, both the Lagrangian and Eulerian modeling approaches are employed depending upon the modeling intent.

The area that an atmospheric model describes varies from a few hundred square meters to thousands of square kilometers, of variable height, depending upon the goal of the modeling study [*Jacobson, 1999*]. The domain of the model usually consists of an array of computational cells, each having a uniform chemical composition [*Seinfeld and Pandis, 1998*]. The size of these cells, that is the volume (area \times height) over which the calculated species concentrations are averaged, determines the spatial resolution of the model, while the number and arrangement of the cells determines its dimensionality (Figure 4.2). The simplest atmospheric model, of dimension zero, consists of only one box which covers the entire

computational domain. In a so-called box model, concentrations are the same everywhere and therefore are a function of time only, $c_i(t)$.

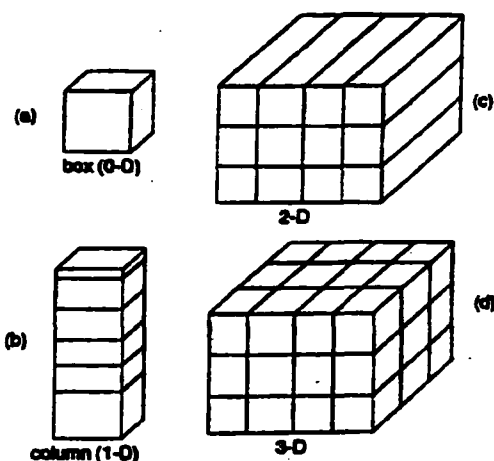


Figure 4.2 Schematic depiction of (a) a box model (zero-dimensional), (b) a column model (one-dimensional), (c) a two-dimensional model, and (d) a three-dimensional model. [From Seinfeld and Pandis, 1998].

As the dimensionality of an atmospheric model increases beyond the simple box model, species concentrations are allowed to be increasingly dependent upon spatial variables as well. As such, one-dimensional models, *i.e.* column models, assume that concentrations are a function of height and time, $c_i(z,t)$, while three-dimensional models simulate the full concentration dependence on latitude and longitude, as well as height and time, $c_i(x,y,z,t)$. The work presented here uses only the simplest modeling representation- the box model.

4.C. Box Models

Box models are closely related to more complex airshed models in that they are based on the conservation of mass equation (mass-action chemical kinetics) and include chemical submodels to represent the detailed photochemical kinetics [Finlayson-Pitts and Pitts, 2000].

However, they have the advantage that they do not require the detailed, temporally and/or spatially resolved emission and meteorological data needed for the more complex models, and hence require less computational time [Jacobson, 1999].

4.C.1. The Eulerian Box Model

The Eulerian box encompassing a region of the atmosphere usually is assumed to have a fixed length, x , a fixed width, y , but variable height, $h(t)$ (Figure 4.3).

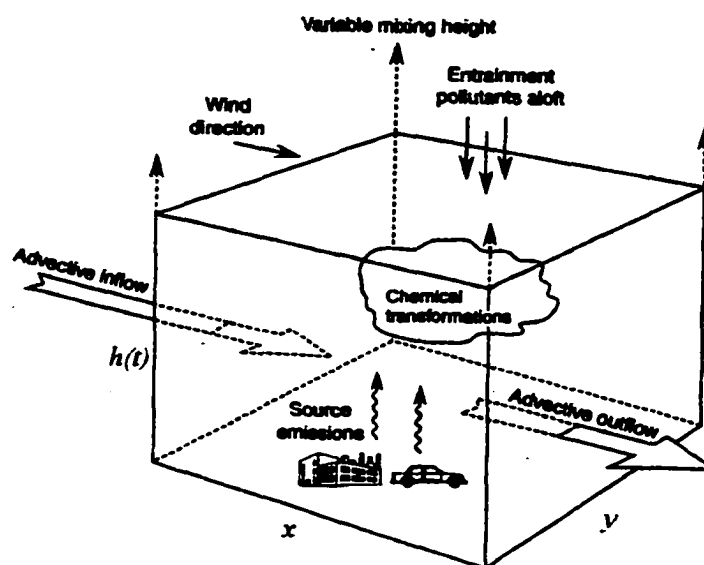


Figure 4.3 Schematic diagram showing the basic elements of a simple Eulerian box model. [From Finlayson-Pitts and Pitts, 2000].

Ambient species concentrations, c_i^a , are advected into the box, displacing species concentrations within the box, c_i , due to the wind, which is assumed to have a constant direction and speed, u . Additionally the chemical composition of species i within the box are affected by their emission rate, E_i , their deposition rate, D_i , and via their net chemical production (or destruction) rate, R_i . (Units are assumed as follows: concentrations in molecules cm^{-3} , wind speed in cm hr^{-1} , chemical production rate in molecules $\text{cm}^{-3} \text{hr}^{-1}$,

emission and deposition rates in molecules hr^{-1}). Assuming initially that the fixed Eulerian box has constant volume, xyh , then, the mass of a particular species i must be conserved such that [Seinfeld and Pandis, 1998],

$$\frac{d}{dt}(c_i xyh) = E_i - D_i + R_i xyh + uyh(c_i^a - c_i). \quad (4.1)$$

Dividing by the volume, simplifies the Eulerian box model governing equation, assuming a constant box height h , to

$$\frac{dc_i}{dt} = \frac{E_i}{xyh} - \frac{D_i}{xyh} + R_i + \frac{u}{x}(c_i^a - c_i). \quad (4.2a)$$

Now let us allow the height of the box to vary diurnally, $h(t)$, in order to simulate the evolution of the atmospheric mixing state, that is, the natural height variation of the PBL, which typically grows during the day due to increased thermal turbulence but falls at night [Jacobson, 1999]. Physically, when the mixing height decreases, there is no direct affect on the concentrations c_i within the boundary layer [Seinfeld and Pandis, 2000]. That is, as the box height decreases, air originally inside the box, which is modeled as having uniform composition, is left aloft but this does not impact the species concentrations remaining within the box. Of course, as the box becomes smaller, surface emissions and sinks have a greater effect. As the mixing height increases, however, the box entrains air from above, thereby impacting the chemical composition within the well-mixed box, c_i , by dilution with ambient air concentrations, c_i^a [Seinfeld and Pandis, 1998]. At time t , when the box has height $h(t)$, an increase in the box height of Δh yields the mass balance equation,

$$(c_i + \Delta c_i)(h(t) + \Delta h) = c_i h(t) + c_i^a \Delta h. \quad (4.3)$$

Neglecting the second-order term, $\Delta c_i \Delta h$, dividing by Δt , and taking the limit as $\Delta t \rightarrow 0$ yields

equation (4.4) for the instantaneous effect of an increasing box height on concentrations c_i ,

$$\frac{dc_i}{dt} = \frac{(c_i^a - c_i)}{h(t)} \frac{dh(t)}{dt} \quad (4.4)$$

Thus, if the mixing height is increasing, then the governing equation for the Eulerian box model must include an additional entrainment term [Seinfeld and Pandis, 1998].

Summarizing, the entraining Eulerian box-model equations are,

$$\frac{dc_i}{dt} = \frac{E_i}{xyh(t)} - \frac{D_i}{xyh(t)} + R_i + \frac{u}{x}(c_i^a - c_i) \quad \text{for } \frac{dh(t)}{dt} \leq 0, \quad (4.2b)$$

and,

$$\frac{dc_i}{dt} = \frac{E_i}{xyh(t)} - \frac{D_i}{xyh(t)} + R_i + \frac{u}{x}(c_i^a - c_i) + \frac{(c_i^a - c_i)}{h(t)} \frac{dh(t)}{dt} \quad \text{for } \frac{dh(t)}{dt} > 0. \quad (4.5)$$

These equations describe mathematically the concentration of species above a given area assuming that the corresponding airshed (box) is well-mixed. They account for emission, deposition, advection of material into and out of the airshed, entrainment of material during the growth of the mixed layer, and chemical reactions, assuming the use of a realistic gas-phase chemical mechanism for calculation of the R_i terms. Chapter 6 discusses, in part, the use of a variable height Eulerian box model to simulate an urban airshed.

4.C.2. The Lagrangian Box Model

The Lagrangian box model approximation is particularly suited for simulating a heavily polluted plume moving away from a near point-source where an initial profile of species react, essentially in a closed system, as the plume evolves. Hence, this model is used in the work presented here to describe the advection of an expanding air parcel containing biomass-combustion emissions. The Lagrangian box is assumed to behave as a point

identically following the wind patterns. Thus the mass balance for the Lagrangian box of fixed size is identical to that for the Eulerian approximation (equation 4.2a) with the exception that the advection terms are absent [Seinfeld and Pandis, 1998]. In this modeling work we assume that the box moves vertically with the mixing layer height, and hence has fixed height, h , but, in order to account for the atmospheric dilution of the plume, has variable width, $y(t)$ (Figure 4.4).

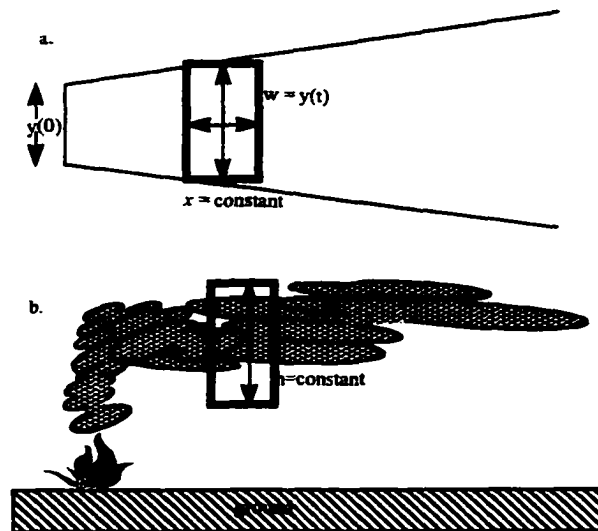


Figure 4.4 Schematic diagram of a diluting Lagrangian box model as used in the work presented here. (a) top view; (b) side view.

Following the same logic as before for the impact of changing height on species concentrations, the instantaneous effect of plume widening on species concentrations, c_i , is,

$$\frac{dc_i}{dt} = \frac{(c_i^a - c_i)}{y(t)} \frac{dy(t)}{dt} \quad (4.6)$$

Since the width of the smoke-plume is always increasing, and we assume its height is fixed, then the governing equation for the diluting Lagrangian box model is,

$$\frac{dc_i}{dt} = \frac{E_i}{xy(t)h} - \frac{D_i}{xy(t)h} + R_i + \frac{(c_i^a - c_i)}{y(t)} \frac{dy(t)}{dt}, \quad (4.7)$$

which is identical to those for the Eulerian model but for the missing advection terms and the assumed constant height but variable width. In the absence of emission and deposition terms, the time variation of species concentrations within the moving Lagrangian box model are affected solely by chemical reaction and the assumed plume-widening expression.

4.D. Summary

In this chapter we have developed the fundamental mathematical equations, which form the basis for atmospheric chemical transport models, under two different box-model approximations. This set of differential equations (one equation for each reacting species) describe, in essence, the temporal evolution of chemical species due to both physical (*i.e.*, emission, deposition, and advection) and chemical processes. However, the chemical transformations occurring within the atmosphere (*e.g.*, the R_i terms) require independent, detailed treatment, which has not been described here but is the focus of the next chapter.

Chapter 5

Photochemical Kinetics

5.A. Introduction

The chemical component of atmospheric chemical transport models is described by a set of mass-action differential equations. That is, species emitted at the Earth's surface are transformed within the atmosphere via thousands of simultaneously occurring, photochemically initiated reactions. Sunlight drives the chemistry through photolytic reactions that dissociate molecules into highly reactive fragments (radicals), and the reactions between these radical species and other trace atmospheric components perpetuates radical-chain reaction mechanisms, generally leading to the degradation (oxidation) of surface emissions. These photochemical reactions are, by definition, dynamic and the field of kinetics is focused on mathematically describing their time dependence. Based upon kinetic principals the temporal behavior of species concentrations due to chemical transformation is described by a set of coupled, often non-linear, differential equations. It is these fundamental time-differentials which describe the chemistry within mathematical, atmospheric models.

In this chapter we present the principals of photochemical kinetics and, thus, the set of differential equations used to describe the chemical transformations within an atmospheric chemical model. This will lead to a discussion of numerical techniques used in to solve large

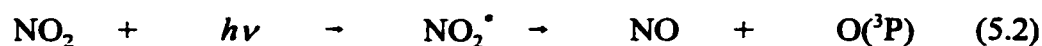
sets of chemical ordinary differential equations, focusing upon those techniques employed in the modeling work presented here. Since atmospheric chemistry is photochemically initiated, we will begin by discussing photolysis reactions and the computation of their reaction rates.

5.B. Photolytic Reactions and their Rates

The energy required to initiate atmospheric chemistry is provided by solar radiation through photolytic reactions [Seinfeld and Pandis, 1998]. Photolysis reactions are unimolecular processes involving the absorption of a single photon of energy $h\nu$, causing the excitation of a molecule to a higher electronic energy state (reaction 5.1) [Woodbury, 1997].



The electronically excited molecule, A^* , can undergo many different processes. It may return to the ground state either by radiative (*i.e.* fluorescence) or non-radiative (*i.e.* collisional) deactivation processes, or it may transfer its excess electronic energy to another molecule [Woodbury, 1997]. Another alternative (and the one that is of interest here) is that the electronically excited molecule may dissociate into fragments [Jacobson, 1999], such as with the photolysis of NO_2 (reaction 5.2).



The rate at which a photolytically-active molecule dissociates has the general form,

$$\text{rate} = j_A [A], \quad (5.3)$$

where j_A is the first-order photodissociation, or photolytic, rate constant of species A. This rate constant depends on the availability of photons of suitable energy, as well as the fractional yield of dissociation as compared to other electronically excited pathways.

In order to determine the availability of photons of suitable energy, it is first necessary

to determine the total photon flux (*i.e.* photons per second) on a given volume of air from all directions, *e.g.*, the *actinic flux* [Seinfeld and Pandis, 1998]. The actinic flux [$I(\lambda, t)$] is a function of wavelength (due initially to the wavelength distribution of solar radiation) and depends upon the absorption and scattering of light by atmospheric constituents, as well as the reflection of radiation from the Earth's surface [Seinfeld and Pandis, 1998]. The attenuation of solar radiation due to absorption and scattering depends upon the concentrations and nature of atmospheric gases and particles and upon the pathlength through which the solar beam passes. This pathlength is, in turn, dependent upon the angle of the sun, which is a function of location (latitude, longitude and altitude), time of day, and date. Thus, computation of the actinic flux, as a function of wavelength and time of day, for a given date and location requires the provision of a surface albedo, to describe the extent of radiative reflection, and a vertical profile of atmospheric gases and particulates, to determine the solar attenuation. In general the actinic flux is calculated within an atmospheric chemical-transport model via a separate radiative transfer submodel which divides the atmosphere into layers and the radiative spectrum into wavelength intervals.

The actinic (photon) flux is the fundamental quantity that is pertinent to all photochemical reactions. However, the photodissociation rate constant depends not only upon the photon flux, but also upon the energy of light which is available, as well as the nature of the molecule itself [Seinfeld and Pandis, 1998]. More specifically, in computing the photolytic rate constant one needs to account for the probability of an encounter between a given molecule, A, and a photon of appropriate energy (*i.e.*, the *absorption cross section*, σ_A) and the probability that the molecule will actually dissociate for each photon that is

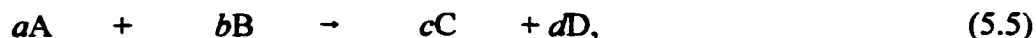
absorbed (*i.e.*, the *quantum yield*, ϕ). Thus, the photodissociation rate constant, j , for a given absorbing molecule, A, as a function of time of day is calculated by integrating over all wavelengths the product of the actinic flux, and the absorption cross section and quantum yield for the molecule of interest (equation 5.4) [Seinfeld and Pandis, 1998].

$$j_A(t) = \int \sigma_A(\lambda)\phi_A(\lambda)I(\lambda,t)d\lambda \quad (5.4)$$

For computational purposes this integral is often approximated by summing over small wavelength intervals. Since the values of $\sigma(\lambda)$ and $\phi(\lambda)$ may not be available on precisely the same intervals as for $I(\lambda, t)$, some interpolation may be necessary [Seinfeld and Pandis, 1998].

5.C. Chemical Reactions, their Rates and the Rate Law

The rate at which a given chemical reaction proceeds is described through the change in the concentrations of reactant and/or product species with time. For the general reaction,



the *rate of reaction* is defined [Woodbury, 1997] as,

$$rate = -\frac{1}{a} \frac{d[A]}{dt} = -\frac{1}{b} \frac{d[B]}{dt} = \frac{1}{c} \frac{d[C]}{dt} = \frac{1}{d} \frac{d[D]}{dt}, \quad (5.6)$$

where the first two differential terms describe the rate of consumption of the reactant species, A and B, and the last two terms describe the rate of formation for the product species, C and D. The relation between the reaction rate and the time-dependant species concentrations for any chemical reaction is known as the *rate law* [Woodbury, 1997] and has the general form,

$$rate = k(T) [A]^u [B]^v [C]^w [D]^x,$$

where u , v , w , and x are constants and $k(T)$ is known as the rate constant, which is constant

in the sense that it doesn't depend on species concentrations, but it does in general depend upon temperature [Woodbury, 1997]. It is important to note that for a given chemical reaction the exponents in the rate law (*e.g.*, u , v , w , and x) do not necessarily bear any relation to the stoichiometric coefficients of the reaction (*e.g.*, a , b , c , and d).

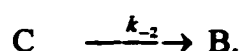
Most chemical reactions occur through a series of steps called *elementary reactions*, which generally involve only one or two reacting molecules [Woodbury, 1997]. (In the case of gas-phase chemistry there are a number of processes that involve a third participant—typically symbolized using the notation 'M'—whose role is simply to siphon off some of the excess energy and thereby stabilize an energy-rich intermediate or product, thus preventing dissociation back into reactants [Finlayson-Pitts and Pitts, 2000].) A reaction *mechanism* is composed of a set of elementary reactions that combine to give the overall observed stoichiometry and rate of reaction [Woodbury, 1997]. The rate law for any *elementary* reaction can be determined from the chemical reaction itself owing to the fact that the reaction rate is proportional to the concentration(s) of the reactant species raised to their stoichiometric coefficient(s) [Woodbury, 1997]. Assuming the general reaction (5.5) is elementary, the rate law for the reaction is,

$$\text{rate} = k(T) [A]^a [B]^b. \quad (5.7)$$

Combining the reaction rate (5.6) with the rate law (5.7) describes the rate of change of each species of a given elementary reaction in time.

$$\frac{d[A]}{dt} = \frac{d[B]}{dt} = -k[A]^a [B]^b$$
$$\frac{d[C]}{dt} = \frac{d[D]}{dt} = k[A]^a [B]^b$$

Hence the time derivatives of each species in a reaction mechanism (which is composed of elementary reactions) can be determined in terms of the rates of each reaction. For example, consider the mechanism,



The time derivatives for each species in terms of the elementary reaction rates are,

$$\frac{d[A]}{dt} = -k_1[A]^2$$

$$\frac{d[B]}{dt} = k_1[A]^2 - k_2[B] + k_{-2}[C]$$

$$\frac{d[C]}{dt} = k_2[B] - k_{-2}[C].$$

Thus, the time variation in the concentrations of each species in a reaction mechanism are generally dependent upon the other species (*i.e.*, they are coupled) and are individually described by nonlinear, homogeneous, ordinary differential equations (ODEs). In order to predict how species concentrations will change in time, we need only integrate the time derivative rate equations, *i.e.*, a set of coupled nonlinear ODEs. For most reaction mechanisms (including atmospheric applications) this requires simultaneously solving a set of equations equal to the number of reacting species, a daunting task which usually requires the implementation of numerical techniques since an analytical solution generally does not exist [Jacobson, 1999; Seinfeld and Pandis, 1998]. By using a sufficiently small integration

step (h) and accurate integration methods, the numerical solution can be made to *converge* upon the true solution [Gear, 1971].

5.D. Solving Chemical Ordinary Differential Equations

5.D. 1. Introduction to Numerical Techniques

Sets of photochemical ODEs are generally *numerically stiff* in that the chemical lifetimes of individual species vary by many orders of magnitude [Jacobson, 1999]. For example, the lifetime of an individual OH radical is on the order of milliseconds, while that for methane (CH_4) is on the order of years. When sets of ODEs are stiff, some classical (explicit) numerical methods are not useful for solving them [Jacobson, 1999; Olcese and Toselli, 1998] as the code will choose prohibitively small integration steps in order to preserve stability. A numerical method is defined to be stable if a fixed change in the starting values of an integration step produces a bounded change in the numerical solution [Gear, 1971]. Semi-implicit integrators can take time steps much longer than the lifetime of the shortest-lived species and remain stable and are therefore generally used in order to solve stiff sets of ODEs [Jacobson, 1999]. Solvers of stiff ODEs are semi-implicit in that their solutions at the end of a time step (c_{t-h}) depend upon time derivatives (c') evaluated at the end of the current time step ($t+h$), the beginning of the current time step (t), and the beginning of previous time steps ($t-nh$) [Jacobson, 1999]. The work presented here uses a semi-implicit solver based upon one of the more advanced, accurate and elegant methods of solving stiff ODEs, Gear's method [Jacobson, 1999].

5.D.2. Gear's Method

Gear's method is based upon the backward Euler approximation using a Newton-

Raphson predictor-corrector methodology. The following summary is based upon a description of the methods given by *Olcese and Toselli* [1998]. In the most simplistic terms, the backward Euler method solves stiff ODEs in the autonomous form,

$$\mathbf{c}' = \mathbf{f}(\mathbf{c}), \quad (5.8)$$

using a semi-implicit scheme involving the first two terms of the Taylor-series expansion, such that

$$\mathbf{c}_{t-h} = \mathbf{c}_t + h\mathbf{f}(\mathbf{c}_{t-h}). \quad (5.9)$$

(The bold notion is used to represent the array of differential equations, thereby avoiding the subscript i notion). By linearizing the equations, as in Newton's method, one obtains

$$\mathbf{c}_{t-h} = \mathbf{c}_t + h[\mathbf{f}(\mathbf{c}_t) + \mathbf{J}(\mathbf{c}_t) \times (\mathbf{c}_{t-h} - \mathbf{c}_t)], \quad (5.10)$$

where $\mathbf{J}(\mathbf{c}_t)$ is the Jacobian matrix, that is the matrix of partial derivatives of the rates of change of each species with respect to every species ($\partial f / \partial c$), evaluated at the current time step. After some manipulation equation 5.10 can be rearranged to,

$$\mathbf{c}_{t-h} = \mathbf{c}_t + h[1 - h\mathbf{J}(\mathbf{c}_t)]^{-1} \times \mathbf{f}(\mathbf{c}_t). \quad (5.11)$$

Hence, the first-order Gear's method numerically calculates future concentrations based upon the current concentrations, and involves the computation and inversion of the Jacobian matrix, in principal, at every time step. In practice numerical solvers based upon Gear's method use higher-order approximations, which are more accurate [*Jacobson*, 1999]. These involve the calculation of future concentrations based upon the current concentrations, previous concentrations, and a prediction of the future concentrations themselves. Within every time step the predicted future concentrations are corrected through a number of iterations (predictor-corrector methodology), based upon their rates of change with respect to each

species (*i.e.*, the Jacobian matrix), until the convergence criterion is met. It is through this iterative procedure, based upon mathematical approximations to the ODEs, that numerical solver routines calculate the time evolution of species concentrations within a chemical mechanism.

5.D.3. The Jacobian Matrix and Sparseness

The Jacobian matrix describes how quickly the differential equation for each species changes at the point at which it is evaluated, and therefore relates, locally, the lifetime of each species to every other species [Gear, 1971]. Because the Jacobian is a $N \times N$ matrix (where N is the number of solvable species), which in principal should be evaluated at every time step, it can be computationally expensive to solve. Fortunately, if the partial derivatives do not change much between time steps the Jacobian need not be re-evaluated at each iteration [Gear, 1971]. Furthermore, for a Newton-type method (such as Gear's method), if the numerical solution, in which the Jacobian matrix is not re-evaluated at each step, converges, it does so to a solution of the differential equation [Gear, 1971].

An additional feature of the Jacobian matrix that reduces computational expense, is the sparseness of the matrix. The Jacobian is the matrix of partial derivatives of the time rates of change of each species with respect to every species, that is,

$$\begin{bmatrix} \frac{\partial^2 c_i}{\partial c_i \partial t} & \dots & \frac{\partial^2 c_N}{\partial c_i \partial t} \\ \vdots & & \\ \frac{\partial^2 c_i}{\partial c_N \partial t} & \dots & \frac{\partial^2 c_N}{\partial c_N \partial t} \end{bmatrix}. \quad (5.12)$$

As it turns out many of these partial derivatives for chemical kinetic systems are zero [Jacobson, 1999; Olcese and Toselli, 1998]. This feature of the Jacobian to contain only a small fraction of nonzero entries is known as sparseness. Since multiplication by zero requires as much computational time as multiplication by any other number, a numerical technique which takes into account the sparseness of the Jacobian matrix, thereby avoiding unnecessary multiplications, can save enormous amounts of computational time [Jacobson, 1999; Olcese and Toselli, 1998].

The semi-implicit numerical solver routine used in the work presented here is based upon Gear's method, utilizing sparse Jacobian matrix techniques. Both the step-size (h) and the order of approximation are actually varied during the integration process, by use of estimates of the local error at each step, in relation to user-specified error tolerances.

5.E. Summary

In this chapter we have defined the rate law and the rate of reaction, and shown how they can be combined to form differential equations that describe the temporal evolution for all species concentrations within a given chemical reaction mechanism. Atmospheric reaction mechanisms tend to involve a large number of species that may react via several, different, simultaneously occurring pathways. Since each chemical species has its own descriptive differential equation, atmospheric chemistry models must be able to solve large sets of ODE's coincidentally. As such we have also discussed numerical techniques employed in atmospheric models. The photochemical kinetic principals and numerical techniques introduced in this chapter are used within the atmospheric chemistry model employed within the work presented here, as described in more detail in the following chapter.

Chapter 6

The Model

6.A. Description of Components

The modeling work presented here was conducted using a zero-dimensional tropospheric chemical mass-balance model developed at the National Center for Atmospheric Research (NCAR) and uniformly coded in FORTRAN 77. This so-called 'Master Mechanism' (MM) [Madronich and Calvert, 1989] is one of the most chemically detailed models available and consists of five separate components.

The photochemical component (directory MM/) contains a detailed description, in ~ 5000 kinetic reactions involving some 2000 chemical species, of the gas-phase photochemistry of alkanes and aromatics up to C₈, alkenes up to C₄, two biogenic hydrocarbons, isoprene and α -pinene, as well as oxygenated species produced in the degradation of these HCs. The only 'clumping' within the reaction mechanism involves the hundreds of peroxy-radical species, which all react among themselves. Explicit depiction of each of these self- and cross-reactions would require $N^2/2$ reactions, where N is the number of radicals (*e.g.*, for 200 peroxy radical species, 20,000 explicit reactions would be necessary). However, of the few of these reactions whose rates have been measured directly the results indicate similar behavior among the radicals grouped according to whether they

are primary, secondary, tertiary or acyl [Madronich and Calvert, 1990]. The rates of the methyl peroxy radical are sufficiently different to be treated separately [Madronich and Calvert, 1990]. Hence counters are used to keep track of each group of peroxy radicals and then, instead of $N^2/2$ reactions, one can write $5N$ reactions that have the same effect as the explicit reactions [Madronich and Calvert, 1990].

A subset of the full reaction mechanism may be selected by specifying an initial profile of chemical species (SHRINK.F). The software then selects a mechanism involving the reactions of these species and their derivatives. Thus, in order to keep the photochemical component of our modeling work somewhat manageable, we have restricted our HCs to C_3 and less. These lightweight HCs comprise ~ 75 % of those emitted from biomass combustion [Lobert et al., 1991; Hao et al., 1996], and this restriction reduces the complete mechanism to 702 reactions (79 photolytic) involving 267 species.

The radiative transfer model, the second component of the MM, computes the actinic flux as a function of time of day and wavelength for a given location and date (directory TUV/) [Madronich, 1987]. In order to perform this numerical calculation the height of the atmosphere must be divided into layers, and the radiative spectrum and day must be divided into intervals, according to user specification. The radiative spectrum between 185 nm and 730 nm is divided into irregularly-spaced intervals of 1 nm resolution initially, eventually increasing to 10 nm. The daily resolution was specified to be 15 minutes. The height of the computational box was approximated to be 1 km, the average height of the PBL, and the vertical grid spacing above this uses 50 levels of 1 km resolution with the uppermost layer comprising the whole of the atmosphere above 50 km. Within this altitude grid, the

distribution of atmospheric gases and particulates must be specified in order to account for the effect of absorption and scattering on incoming solar radiation.

Atmospheric conditions are based upon the US standard atmosphere (1976), which specifies the vertical profiles of temperature, air density, [O₂] and [O₃], assuming clear-sky conditions. (The assumed clear-sky conditions can only be strictly representative of the top of the smoke plume.) Aerosol optical depths are taken from Elterman [1968] at 340 nm and assumed to scale inversely with the first power of wavelength. Additionally, the reflection of radiation by the Earth's surface (*i.e.*, albedo) affects the total photon flux within a given volume of air. The surface albedo was specified to be 0.15, appropriate for a savanna covered surface [Finlayson-Pitts and Pitts, 2000], and is assumed to be Lambertian, *i.e.*, the reflected light is isotropic [Seinfeld and Pandis, 1998], and independent of wavelength or direction of incidence of light.

In order to represent photochemical processing occurring over Southern Africa during the tropical dry season, where 80% of global biomass combustion is reported to occur [Hao and Liu, 1994], the date and location was specified to be August 31 at 13°S and 27°E. All of the above user-supplied information allow the atmospheric, surface, and solar pathlength effects on the photon flux into the computational box to be determined via numerical summation across the altitude spacing and within the wavelength and daily resolution. This detailed algorithm to compute the actinic flux, coupled to the explicit photochemical mechanism, (*i.e.* the first two sub-models of the MM) are the real strengths of the MM, but are also computationally expensive and thereby restrict the use of the MM to the more simple atmospheric modeling applications.

The actinic flux, as a function of time of day and wavelength, is used as input for the third MM sub-model (directory JBLOCK/), which computes the photodissociation rate constants as a function of time of day. The photolytic cross-sections and quantum yields for absorbing species are additional necessary inputs for this computation. The photolytic rate constants are then compiled along with the reduced mechanism and the user-specified initial conditions (*e.g.* an array of initial concentrations, the time in which the simulation should begin and end, *etc.*) into a solver input file by the fourth component of the MM (directory PREP/). The final sub-model of the MM is the actual ODE solver (directory SOLV/), which reads in all the data and numerically integrates the kinetic differential equations to yield the time variations for all species concentrations. The overall rate for each reaction, which depends not only upon the supplied kinetic rate constant, but also upon the time-dependent reactant species concentrations, are also tabulated.

6.B. Modifications to the MM Numerical Solver

A number of modifications have been made to the MM numerical integration (a.k.a. 'solver') routine (directory SOLV/) in order to increase stability and adapt the model to our specific simulation needs. The MM originally used Gear's method [Gear, 1971] in order to solve the stiff system of chemical ODEs. While Gear's code was the original of the more advanced semi-implicit numerical methods, we had difficulty getting the solution to converge under highly polluted conditions. Hence, the MM 'solver' routine was adapted to use the Livermore solver for ordinary differential equations using sparse matrix techniques (LSODES) [Hindmarsh, 1983]. LSODES is based upon Gear's method, but uses revised algorithms for method, step-size and order adjustment [Seinfeld and Pandis, 1998]. It is

considered to be one of the most robust routines available to obtain solutions to stiff systems of ODEs and has been used to evaluate the precision of a number of other methods [Olcese and Toselli, 1998]. Implementation of LSODES required the sparse Jacobian matrix be supplied, as the system of chemical ODEs is stiff [Olcese and Toselli, 1998; Hindmarsh, 1983]. The sparseness of the Jacobian matrix is described via two arrays: IA, which delineates the number of nonzero elements (NNZ) in each column [e.g., the NNZ in column i is $IA(i+1) - IA(i)$], and JA, which specifies the specific row elements in each column that are nonzero. Using these arrays, a subroutine was written to compute the sparse Jacobian matrix by column, as required by LSODES, and by reaction, as required by the MM solver. (The MM can be used without the below additional changes by setting NDILUT \neq 1, NAMBT = 0 and NSR = 0.)

6.B.1. Biomass-Combustion Smoke-Plume Modeling

Additional minor modifications were made to the MM in order to more accurately model the evolution of a biomass-combustion smoke-plume. The modeling work presented here uses a Lagrangian box to represent the advection of an air parcel, initially containing biomass-combustion emissions, in time. We assume that species concentrations within the box are not affected due to further emission or deposition, and hence the governing equation (see equation 5.7) for a box of constant height and length but variable width, $y(t)$, is,

$$\frac{dc_i}{dt} = R_i + \frac{(c_i^a - c_i)}{y(t)} \frac{dy(t)}{dt}, \quad (6.1)$$

where R_i represents the net photochemical production (or destruction) rate of species i (as determined based upon the photochemical mechanism), and c_i^a and c_i are the associated

ambient and smoke-plume concentrations, respectively. The variable width term, $y(t)$, accounts for the atmospheric dilution due to expansion of the smoke-plume as it evolves, which has a substantial impact on predicted species concentrations [Kley, 1997; Mauzerall *et al.*, 1998; Poppe *et al.*, 1998]. The form of $y(t)$ is assumed to be,

$$y(t) = [y(0)^2 + 8K_y t]^{1/2}, \quad (6.2)$$

where $y(0)$ is the initial plume-width and K_y is the cross-flow (horizontal) diffusion coefficient. This equation was obtained with reference to the Gaussian solution to the Fickian diffusion equation, $d\sigma/dt = K_y/\sigma$ [Csanady, 1973], by setting the plume width, $y(t)$, equal to twice the Gaussian variance, σ [Sillman *et al.*, 1990]. Substitution of (6.2) into (6.1) yields,

$$\frac{dc_i}{dt} = R_i + \frac{4K_y}{[y(0)^2 + 8K_y t]} (c_i^a - c_i). \quad (6.3)$$

for the governing time-dependent equation of species concentration, c_i , in an expanding, Lagrangian box as incorporated into the modeling work presented here. The expansion term of (6.3) goes to zero as $t \rightarrow \infty$ and $(c_i^a - c_i) \rightarrow 0$, as is expected. The parameter K_y was determined here using an initial plume width, $y(0)$, of 1 km and fitting the dilution rates of excess (over ambient) CO and CO₂ mixing ratios (ΔCO and ΔCO_2) to those estimated from observations on large isolated plumes by Babbitt *et al.* [1998] and Goode *et al.* [2000]. Based upon this curve fitting K_y is set to $3.33 \times 10^{-3} \text{ km}^2 \text{ min}^{-1}$. Equation (6.3) is incorporated into the MM such that all species concentrations are diluted by their corresponding ambient concentrations, c_i^a , at every time step (assuming that a flag, NDILUT, is set to 1).

Diurnal variations in ambient concentrations, c_i^a , were estimated by running the MM (with NDILUT = 0 and NAMBT = 1) holding a profile of longer-lived species concentrations

(Table 6.1) typical of a rural environment [Finlayson-Pitts and Pitts, 2000; Seinfeld and Pandis, 1998] constant. All other species concentrations were allowed to vary.

Table 6.1. Ambient Concentrations Used in Smoke-Plume Dilution

Name	Formula	Total Concentration (ppbv)
Nitrogen	N ₂	7.8 × 10 ⁸
Nitrogen Dioxide	NO ₂	1
Nitric Oxide	NO	0.05
Nitrous Oxide	N ₂ O	320
Dinitrogen Pentoxide	N ₂ O ₅	0.005
Nitric Acid	HNO ₃	0.2
Nitrous Acid	HNO ₂	0.03
Ammonia	NH ₃	0.1
Peroxyacetyl Nitrate	PAN	0.05
Hydrogen Cyanide	HCN	0.19
Methane	CH ₄	1650
Ethane	C ₂ H ₆	13.50
Ethene	C ₂ H ₄	11.10
Ethyne (Acetylene)	C ₂ H ₂	8.65
Propane	C ₃ H ₈	18.70
Propene	C ₃ H ₆	2.6
Methanol	CH ₃ OH	0.5
Acetic Acid	CH ₃ COOH	2.1
Formic Acid	HCOOH	5.4
Formaldehyde	CH ₂ O	9.1
Carbon Dioxide	CO ₂	3.5 × 10 ⁵
Carbon Monoxide	CO	200
Carbonyl Sulfide	OCS	0.5
Sulfur Dioxide	SO ₂	0.2
Oxygen	O ₂	2.1 × 10 ⁸
Ozone	O ₃	29.30
Hydrogen Peroxide	H ₂ O ₂	0.690
Water	H ₂ O	1.0 × 10 ⁷
Hydrogen	H ₂	500

There are some species (~ 30, in our case) within the MM chemical mechanism which are product-only species (these can be determined using the program PRODUCT.FOR in directory PRODUCT/) and hence their concentrations continually increase in time. Therefore, the ambient simulation was run until all species, aside from product-only species, achieved a stable diurnal cycle (typically ~ 60 - 90 day simulation). Ambient profiles for a 24-

hour day were then tabulated (see directory PROFILE/) at 3-minute resolution and linear interpolation methods were used at intermediate times. It is important to note that as time increases the ambient concentrations become a more important component of the calculated smoke-plume concentrations.

One type of destruction term not explicitly represented within the kinetics of a chemical mechanism is loss due to heterogeneous chemistry, *i.e.*, aerosol formation. Due to the significant direct production of gaseous ammonia $[\text{NH}_3(\text{g})]$ in biomass combustion, the formation of ammonium nitrate aerosol $[\text{NH}_4\text{NO}_3(\text{s})]$ becomes important. This formation directly affects the plume concentrations of $\text{NH}_3(\text{g})$ and $\text{HNO}_3(\text{g})$, and indirectly affects the concentrations of many nitrogenous species, as well as O_3 and HO_x . Thus, for smoke-plume modeling, the MM solver was adapted to include two additional, conditional terms in the differential equations for $\text{NH}_3(\text{g})$ and $\text{HNO}_3(\text{g})$ in order to describe their loss due to $\text{NH}_4\text{NO}_3(\text{s})$ formation. The thermodynamic equilibrium constant for $\text{NH}_4\text{NO}_3(\text{s})$, defined as $K_{eq} = [\text{NH}_3(\text{g})]_{eq}[\text{HNO}_3(\text{g})]_{eq}$, is $3.07 \times 10^{-6} \text{ ppm}^2$ at 297 K [Seinfeld and Pandis, 1998]. The rate of removal of $\text{NH}_3(\text{g})$ and $\text{HNO}_3(\text{g})$ is assumed to be diffusion controlled, *e.g.*, the reaction rate constant, k , is $10.5 \text{ ppm}^{-1} \text{ min}^{-1}$ when $[\text{NH}_3(\text{g})][\text{HNO}_3(\text{g})] > K_{eq}$, and zero otherwise.

6.B.2. Urban Modeling

As a result of some of the effects occurring within a simulated biomass-combustion smoke-plume (to be discussed in detail later), we became interested in modeling the mixing of such a smoke-plume into an urban environment. As fate would have it, this very event occurred during the western US forest fires of 2000, in which smoke from fires in the

Bitterroot National Forest was blown (advected) into the Missoula valley urban airshed. Hence we chose to apply the results of our smoke-modeling studies to this particular occurrence. We simulate the localized urban environment (indicated via the flag NSR $\neq 0$) using a well-mixed, zero-dimensional box model employing the Eulerian approximation with source emissions from the surface. Recall from chapter 5, section C.1 (equations 5.2b and 5.5) that the governing equations for the time-dependent species concentrations within an Eulerian box including PBL-height variation are,

$$\frac{dc_i}{dt} = \frac{E_i}{xyh(t)} - \frac{D_i}{xyh(t)} + R_i + \frac{u}{x}(c_i^a - c_i) \quad \text{for } \frac{dh(t)}{dt} \leq 0, \quad (6.4)$$

and,

$$\frac{dc_i}{dt} = \frac{E_i}{xyh(t)} - \frac{D_i}{xyh(t)} + R_i + \frac{u}{x}(c_i^a - c_i) + \frac{(c_i^a - c_i)}{h(t)} \frac{dh(t)}{dt} \quad \text{for } \frac{dh(t)}{dt} > 0. \quad (6.5)$$

The photochemical mechanism (used to obtain the R_i terms) and ambient conditions, c_i^a , are the same as employed in the biomass-combustion smoke-plume simulations. Photolytic rate constants were computed for August 5 at 48°N and 114°W (*i.e.*, Missoula, MT), but found to have little effect upon predicted species concentrations as compared to the South African profile. Hence, for the purpose of comparison, the urban model employs the same photolytic rate constants as used in the smoke-plume modeling. In order to depict stagnant conditions, the wind speed, u , was specified to be 1 mile hr⁻¹. The area of the computational box was chosen to be 64 mile² [Schmidt], while the variation in the height of the PBL, $h(t)$, was taken from *Sillman et al.* [1990] (Figure 6.1).

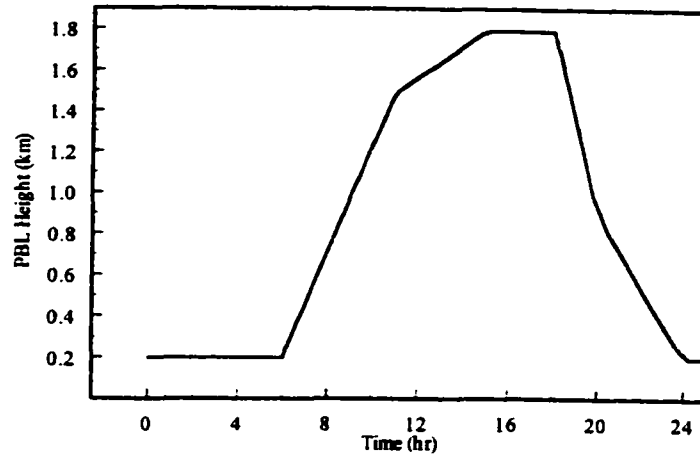


Figure 6.1 Planetary Boundary Layer (PBL) height, in kilometers, versus time of day, in hours, as used in the urban model. Midnight = 0 and 24 hours.

Standard deposition rates, D_p , (Table 6.2) were based on *Seinfeld and Pandis* [1998].

Table 6.2 Deposition rates, in seconds⁻¹, used in the urban model.

Chemical Species	Deposition Rate (sec ⁻¹)
O ₃	1.0×10^{-6}
NO	1.0×10^{-6}
NO ₂	1.0×10^{-6}
CO	1.0×10^{-7}
HNO ₃	1.0×10^{-5}

Urban emission rates, E_p , were obtained for the city of Missoula airshed as described below (directory SOURCE/). Total daily NO_x and CO emissions were taken from reports obtained through the Missoula County Environmental Health Department [*Schmidt*]. Within the Missoula city limits (a 64 mile² area), vehicles account for ~ 70% of yearly NO_x emissions, with the remaining being accounted for by the burning of natural gas and wood (~ 28%) and industrial sources (~ 2%) [*Schmidt*]. In this same region, vehicles account for ~ 78 % of average daily CO emissions, with the remaining being accounted for by the burning of natural gas and wood (~ 16%) and industrial, locomotive, and aviation exhaust (~ 6%) [*Schmidt*].

Thus, within the Missoula urban airshed the majority of NO_x and CO emissions result from vehicles. It is assumed that most natural gas and wood combustion occurs during the winter season [Schmidt], hence for the summertime urban modeling reported here we assume that the only emissions into the modeled urban airshed result from vehicular emissions. Based upon this assumption, the total daily NO_x and CO emissions are 3.1 and 36.1 metric tons, respectively [Schmidt]. The NO_x emissions are further assumed to be composed in a 9:1 ratio of NO to NO₂ [Finlayson-Pitts and Pitts, 2000].

Total daily VOC emissions were estimated to be 1/10 of CO emissions (3.6 metric tons) based upon a Missoula county emission inventory study [Schmidt]. Speciation of the VOCs was based on a program, called SPECIATE (version 3.0), obtained through the Environmental Protection Agency (EPA) website.

Table 6.3 Scaling of VOCs contained within both the MM reduced mechanism and the EPA vehicular-emission -speciation. Actual percentage is based upon the EPA SPECIATE program; adjusted percentage is that used in this work for speciation of the urban VOC emissions. Total emission per day is based upon the VOC total emissions of 3.6 metric tons and the weighted-average molecular weight of 25.32 grams mole⁻¹.

Chemical Species	Actual %	Adjusted %	Total Emission per Day (molecules)
CH ₄	10.97	38.82	3.33×10^{28}
C ₂ H ₆	1.79	6.33	5.42×10^{27}
C ₂ H ₄	8.41	29.76	2.55×10^{28}
C ₂ H ₂	2.25	7.96	6.82×10^{27}
C ₃ H ₆	2.88	10.19	8.73×10^{27}
CH ₂ O	1.42	5.03	4.31×10^{27}
CH ₃ CHO	0.49	1.73	1.48×10^{27}
CH ₃ CH ₂ CHO	0.05	0.18	1.54×10^{26}
Total	28.26	100.00	8.57×10^{28}

Unfortunately, within this EPA speciation of vehicular VOC emissions, only 8 species (accounting for ~ 28 % of total vehicular VOC emissions) are likewise present within the 267 chemical species of the (reduced) photochemical mechanism used here. Hence, in order to

use the same photochemical mechanism as used in the smoke-plume modeling, while fully representing the total daily VOC emissions (3.6 metric tons), these 8 vehicular VOC emissions were scaled to represent the whole (Table 6.3).

The diurnal variation of source emissions was approximated based upon an average daily traffic flow for the city of Missoula. Hourly car counts were obtained for six sites across Missoula (Table 6.4) [Segar, 2000].

Table 6.4 Hourly car counts for six sites across Missoula, MT [From Segar, 2000]. Time, in hours, starts at 1 am and ends at midnight (24 hours). Sites are as follows: 30- 6th street at the corner of Arthur and Maurice; 69- lower Miller Creek, 100 feet southwest of Y; 99- Mount road 300 feet west of Johnson; 136- Grant Creek north of I-90; 173- South avenue between Catlin and Washburn; 178- Russell street south of 34th.

Time (hr)	Number of Cars					
	Site 30	Site 69	Site 99	Site 136	Site 173	Site 178
1	58	22	67	21	79	53
2	45	7	34	8	43	40
3	37	3	31	10	28	18
4	21	7	15	6	14	18
5	25	9	14	12	32	28
6	129	32	68	41	67	81
7	256	126	203	90	211	230
8	930	319	848	380	713	647
9	1096	253	903	332	839	702
10	701	152	639	270	841	519
11	608	156	701	259	899	524
12	854	182	807	294	1039	618
13	944	202	856	365	1192	702
14	792	212	928	342	1151	720
15	899	209	941	277	1229	631
16	1095	268	1214	386	1332	877
17	1099	332	1375	443	1210	909
18	1213	421	1373	467	1172	966
19	898	330	857	401	841	853
20	662	203	542	282	593	625
21	557	228	436	216	438	523
22	412	144	329	155	350	437
23	250	76	214	101	212	237
24	125	39	135	68	105	142
Total	13706	3932	13530	5226	14630	11100

These hourly counts were divided by the total number of cars for the day in order to obtain

a fractional hourly traffic flow (Figure 6.2a). Despite the wide range of locations at which these counts were taken, there exists a high diurnal correlation between sites (Figure 6.2a). Thus, in order to approximate an average daily traffic flow across the entire city of Missoula, hourly car counts for all six locations were totaled and used to obtain a combined fractional hourly traffic flow (Figure 6.2b). Our diurnal variation (Figure 6.2b) compares quite well with that recommended by *Hough* [1986].

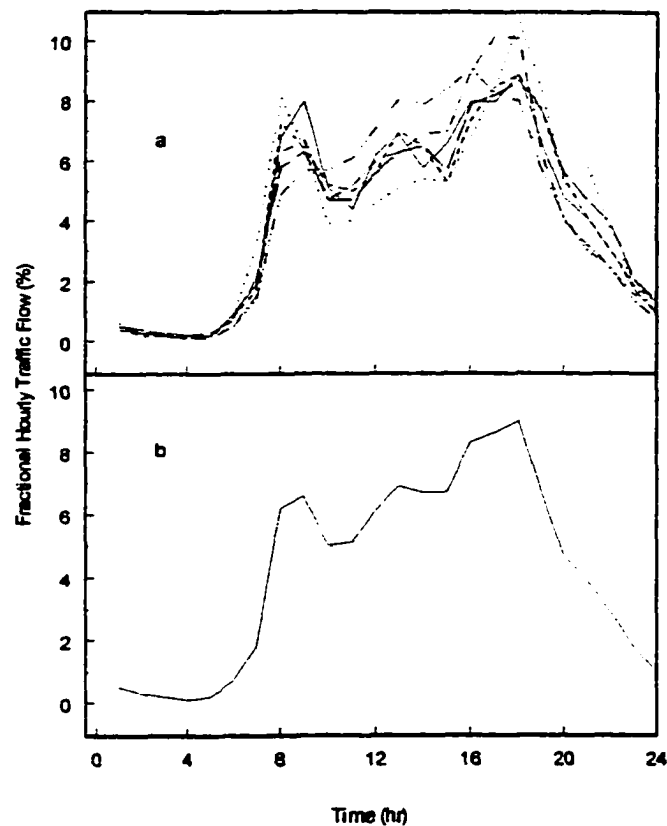


Figure 6.2 Fractional hourly traffic flow versus time of day. (a) Each of the six Missoula sites individually. Site 30 (solid); site 69 (dotted); site 99 (dash-dot); site 136 (dashed); site 173 (dash-triple dot); site 178 (long dash). (b) Fraction of the total for all six sites, as is used in the urban model.

Daily total emissions (DT_{*i*}) for NO_x, CO and VOCs (3.1, 36.1, and 3.6 metric tons, respectively) were scaled according to this fractional hourly traffic flow (*frac_{*i*}*) in order to obtain time-dependent source emission rates, *E_{*i*}* (equation 6.6).

$$E_i = DT_i * frac_i \quad (6.6)$$

Thus, the diurnal variation of source emissions within the MM follows basic traffic flow patterns (Figure 6.2b) and is determined at every time step using linear interpolation methods between hourly data points.

6.C. Summary

In this chapter we have provided a detailed description of the atmospheric chemistry model employed in this work. Additionally, we have specified chosen parameters, model implicit assumptions, and modifications required to conduct smoke-plume and urban airshed simulations. The following two chapters detail the results of these simulations using the atmospheric model as described above. Chapter 7 describes our biomass combustion smoke plume simulations designed to investigate the effect of the inclusion of oxygenated organic species, while chapter 8 reports our investigations on the mixing of an oxygenated smoke-plume with an urban environment.

Chapter 7

Results of Smoke Plume Simulations

7.A. Overview

In order to determine the impact of oxygenated organic species on smoke-plume photochemistry, and therefore on overall plume composition, two sets of simulations were conducted using the same photochemical mechanism but differing initial conditions (*i.e.*, *No Oxy* and *All Oxy* simulations). In general, initial concentrations within the smoke plume are chosen to approximate fire-averaged conditions ~ 1 km above a large biomass fire with a ΔCO_2 of 100 ppmv (parts per million by volume) and a $\Delta\text{CO}/\Delta\text{CO}_2 = 7\%$. Other initial concentrations were scaled to either ΔCO_2 or ΔCO depending upon whether a particular species results mainly from flaming or smoldering combustion [Yokelson *et al.*, 1996a]. Simulations using an initial species profile for fresh smoke based upon Lobert *et al.* [1991], not including oxygenated species and referred to here as *No Oxy*, are used as a standard. Other simulations were then conducted with the six primary oxygenated species (CH_2O , $\text{CH}_2(\text{OH})\text{CHO}$, CH_3OH , $\text{C}_6\text{H}_5\text{OH}$, CH_3COOH , HCOOH) added at the levels observed on average by Yokelson *et al.* [1996a] (except for phenol, whose concentration represents a high-end limit) in a profile referred to as *All Oxy*. The *No Oxy* profile is similar to that used in most previous smoke plume models, while the *All Oxy* profile includes the influence of

oxygenated organic compounds. Additionally, simulations were performed using perturbed initial values of VOCs and NO_x in order to evaluate VOC/NO_x sensitivity.

7.B. Non-Diluting Smoke Plume

We began our investigation of the photochemistry within biomass combustion smoke plumes using a simple (0-D) Lagrangian box model (assuming no emission or deposition terms), in the absence of plume dilution (*i.e.*, using the MM without any modifications). These preliminary, day-long simulations start at midnight and use a mechanism of 1222 chemical reactions, involving 452 species, owing to the inclusion of methyl chloride and α -pinene chemistry. It was later decided to exclude these latter compounds (reducing the mechanism to 702 reactions involving 267 species), in part to simplify the chemical mechanism, but also due to uncertainties in their smoke-plume concentrations.

For both initial species profiles (*i.e.*, *No Oxy* and *All Oxy*) twelve simulations were carried out in which the (initial) $\Delta[\text{NO}]_0/\Delta[\text{CO}]_0$ ratio was varied from 1 to 6 % for three different $\Delta[\text{CH}_2\text{O}]_0/\Delta[\text{CO}]_0$: 0 %, 2 % and 4 %. The variation in NO initial concentration exemplifies the range observed in real biomass fires. A 1 % $\Delta[\text{NO}]_0/\Delta[\text{CO}]_0$ emission ratio is representative of smoldering combustion, while flaming combustion yields an upper limit $\Delta[\text{NO}]_0/\Delta[\text{CO}]_0$ of 4-6% (a $\Delta[\text{NO}]_0/\Delta[\text{CO}]_0$ of 2 % describes an average combustion situation) [Yokelson *et al.*, 1999b]. Additionally, the variation of both $[\text{NO}]_0$ and $[\text{CH}_2\text{O}]_0$ puts their individual effects into perspective. NO drives the conversion of HO₂ to OH, forming a source of NO₂, which may then photolyze to give O₃. Some of this O₃ may then photolyze to yield additional OH. CH₂O, on the other hand, is well-known to provide a source of HO₂ radicals, either through its chemistry or through direct photolysis [Seinfeld and

Pandis, 1998]. Hence, one expects increasing [NO] will lead to an increase in [O₃] and [HO_x] (mostly in the form of OH), while increasing [CH₂O] will lead to an increase in [HO_x] (mostly in the form of HO₂) which does not depend on increased [O₃].

Initial concentrations used in these simulations are given in Table 7.1.

Table 7.1 Initial Concentrations (*i.e.*, at 12 pm) used in Various Non-Diluting Smoke-Plume Simulations.

Name	Formula	Total Concentration (ppbv)
Nitrogen	N ₂	7.7 × 10 ⁸
Nitrogen Dioxide	NO ₂	36.60
Nitric Oxide	NO	75.20 (1%), 150.4 (2 %), 300.8 (4 %), or 451.2 (6 %)
Ammonia	NH ₃	150.4
Hydrogen Cyanide	HCN	15.00
Methane	CH ₄	609.8
Ethane	C ₂ H ₆	47.60
Ethene	C ₂ H ₄	150.4
Ethyne (Acetylene)	C ₂ H ₂	47.60
Propane	C ₃ H ₈	10.20
Propene	C ₃ H ₆	33.20
Methanol	CH ₃ OH	150.4 (<i>All Oxy only</i>)
Phenol	C ₆ H ₅ OH	61.00 (<i>All Oxy only</i>)
Acetic Acid	CH ₃ COOH	150.4 (<i>All Oxy only</i>)
Formic Acid	HCOOH	48.80 (<i>All Oxy only</i>)
Formaldehyde	CH ₂ O	0 (0 %), 150.4 (2 %), or 300.8 (4 %)
Hydroxyacetaldehyde	CH ₂ (OH)CHO	48.80 (<i>All Oxy only</i>)
Carbon Dioxide	CO ₂	9.8 × 10 ⁴
Carbon Monoxide	CO	7320
Carbonyl Sulfide	OCS	48.80
Sulfur Dioxide	SO ₂	48.80
Oxygen	O ₂	2.0 × 10 ⁸
Ozone	O ₃	29.30
Hydroxyl Radical	OH	2.0 × 10 ⁻⁵
Hydroperoxyl Radical	HO ₂	0.020
Hydrogen Peroxide	H ₂ O ₂	0.690
Water	H ₂ O	1.0 × 10 ⁷
Hydrogen	H ₂	150.4
Methyl Chloride	CH ₃ Cl	11.70
α-Pinene	C ₁₀ H ₁₆	150.4

These concentrations differ from those used in later simulations in that they include methyl chloride and α-pinene, and in that we had not yet accounted for background (ambient) species

concentrations; hence, the smoke-plume concentrations used here represent only the excess mixing ratios for most species (exceptions being N_2 , O_2 , O_3 , and H_2O_2 whose concentrations result solely from ambient values).

These preliminary simulations strongly suggest that the oxygenated compounds identified by *Yokelson et al.* have a significant impact on smoke plume chemistry. In particular, the presence of the oxygenated species causes very different trends in the maximum concentrations of O_3 , OH, and HO_2 (Figures 7.1, 7.2, and 7.3), species of marked tropospheric importance.

7.B.1. Effects on $[O_3]$ and $[OH]$ Maxima

Maximum concentrations of O_3 and OH follow classic nonlinear behavior in the *No Oxy* simulations as $[NO]_0$ is increased. That is, as $[NO]_0$ is increased the maximum concentrations initially increase as well, but eventually, beyond a 'threshold' level, they decrease (Figure 7.1). Increasing $[CH_2O]_0$ acts to increase this 'threshold' level, *i.e.*, CH_2O acts as a 'buffer' of sorts (Figure 7.1). These results can be rationalized as follows. The nonlinear behavior is very likely attributable to a transition between NO_x - and VOC-sensitive photochemical processing as the initial $[NO_x]$ is increased. From studies of tropospheric chemistry models [*Sillman*, 1999, and references therein], it is known that as $[NO_x]$ is initially increased, $[O_3]$ and $[OH]$ likewise increase due to NO_x -sensitive atmospheric processing, in which radical species are more prevalent than is NO_x , leading to rapid conversion of NO-to- NO_2 and photochemical O_3 production [*Sillman*, 1999, and references therein]. However, beyond a certain level, increasing $[NO_x]$ causes $[O_3]$ and $[OH]$ to decrease; this signifies a transition to VOC-sensitive photochemical reaction pathways in which radicals are removed

via Rad + NO_x reactions, thus inhibiting both the conversion of NO-to-NO₂ and the production of O₃ [Sillman, 1999, and references therein]. An increase in the [VOC]/[NO_x] ratio (in this case, through the addition of CH₂O), increases the source of radical species relative to the source of NO_x, thereby increasing the ‘threshold’ level of initial [NO] that must be consumed before the transition between NO_x- and VOC-sensitive chemistry occurs (Figure 7.1).

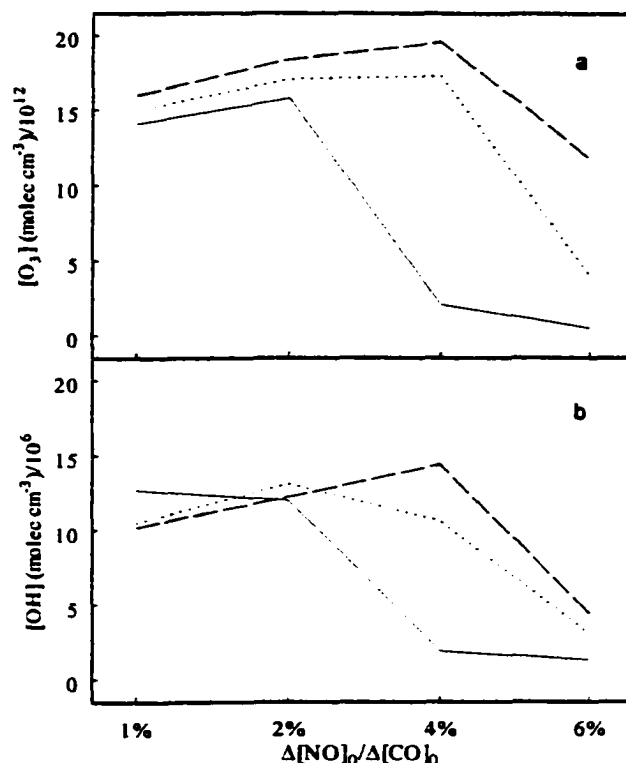


Figure 7.1 Simulated maximum concentrations under *No Oxy* conditions for (a) O₃ (molecules/cm³/10¹²) and (b) OH (molecules/cm³/10⁶). $\Delta[\text{CH}_2\text{O}]_0/\Delta[\text{CO}]_0 = 0\%$, solid lines; $\Delta[\text{CH}_2\text{O}]_0/\Delta[\text{CO}]_0 = 2\%$, dotted lines; $\Delta[\text{CH}_2\text{O}]_0/\Delta[\text{CO}]_0 = 4\%$, dashed lines.

Hence, in the *No Oxy* simulations increasing [NO]₀ causes a transition between NO_x- and VOC-sensitive photochemistry, while increasing [CH₂O]₀ acts to delay this transition.

This nonlinear behavior of [O₃] and [OH] maxima observed in the *No Oxy* simulations

is not apparent in the *All Oxy* simulations. The maximum concentrations of these species monotonically increase with increasing $[\text{NO}]_0$ within the range investigated here (Figure 7.2).

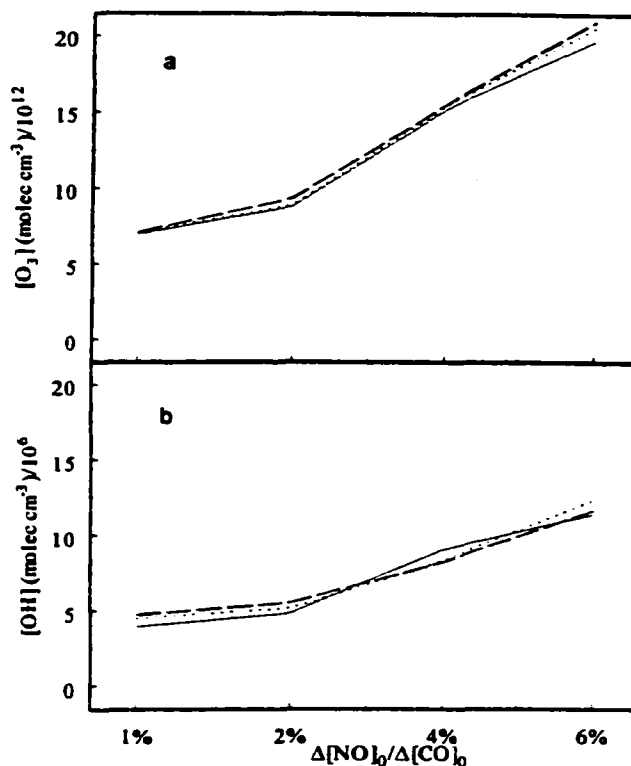


Figure 7.2 Simulated maximum concentrations under *All Oxy* conditions for (a) O_3 (molecules/ $\text{cm}^3/10^{12}$) and (b) OH (molecules/ $\text{cm}^3/10^6$). $\Delta[\text{CH}_2\text{O}]_0/\Delta[\text{CO}]_0 = 0\%$, solid lines; $\Delta[\text{CH}_2\text{O}]_0/\Delta[\text{CO}]_0 = 2\%$, dotted lines; $\Delta[\text{CH}_2\text{O}]_0/\Delta[\text{CO}]_0 = 4\%$, dashed lines.

Additionally, $[\text{O}_3]$ and $[\text{OH}]$ maxima show a remarkable stability to changes in $[\text{CH}_2\text{O}]_0$ under the *All Oxy* initial conditions, *e.g.*, increasing $[\text{CH}_2\text{O}]_0$ causes little variation in their maximum values. This monotonic increase in maxima for $[\text{O}_3]$ and $[\text{OH}]$ seems to be due to the increase in the $[\text{VOC}]/[\text{NO}_x]$ ratio through the addition of the oxygenated species, causing conditions within the *All Oxy* smoke plume to remain NO_x -sensitive for all values of $[\text{NO}]_0$ used here. Hence in these preliminary simulations conditions within the *No Oxy* smoke plume may either

be NO_x - or VOC-sensitive (as characterized $[\text{O}_3]$ and $[\text{OH}]$ maxima), while conditions within the *All Oxy* smoke plume are found to be dominated solely by NO_x -sensitive chemistry.

It is apparent (from traces of concentration versus time) that the OH radical has only one daytime peak in the *No Oxy* simulations that is well-known to occur due to photolysis reactions during the diurnal cycle. However, the addition of CH_2O , as well as the inclusion of oxygenates, causes a second, later, daytime peak to appear. This second peak is also due to photolytic reactions since both peaks disappear when the simulation is conducted in the absence of light. As $[\text{CH}_2\text{O}]_0$ is increased and oxygenated species are included, this second peak becomes more pronounced, indicating that it is due to transient species somehow related to the oxygenated species. Furthermore, while increasing the concentrations of oxygenates causes the second peak to become larger, increasing $[\text{NO}]_0$ decreases it.

An additional interesting difference between the *All Oxy* and *No Oxy* simulations is that at low- $[\text{NO}_x]_0$, the $[\text{O}_3]$ maxima are lower in the *All Oxy* case than in the *No Oxy* case, while at higher $[\text{NO}_x]_0$ these maxima are greater in the *All Oxy* case (Figures 7.1 and 7.2). This effect is repeated by $[\text{OH}]$ maxima and indicates not only a difference in dominant reaction pathways occurring within the two simulations, but it also reflects upon the overall level of photochemistry. These effects are investigated in much greater detail in our subsequent (diluting) smoke-plume simulations.

7.B.2. Effect on $[\text{HO}_2]$ Maxima

The maximum HO_2 concentrations decrease in all *No Oxy* simulations as $[\text{NO}]_0$ is increased, but they decrease less quickly as $[\text{CH}_2\text{O}]_0$ is increased (Figure 7.3a). The first result is consistent both with the conversion of NO -to- NO_2 , which is accompanied by an

associated conversion of HO₂-to-OH, and with the role of Rad + NO_x reactions. Rad + NO_x reactions dominate VOC-sensitive chemistry and occasionally dominate NO_x-sensitive chemistry (especially when close to the NO_x- to VOC-sensitive transition), thereby removing radicals from the system. The effect of CH₂O is compatible with its role as an HO₂ source [Seinfeld and Pandis, 1998].

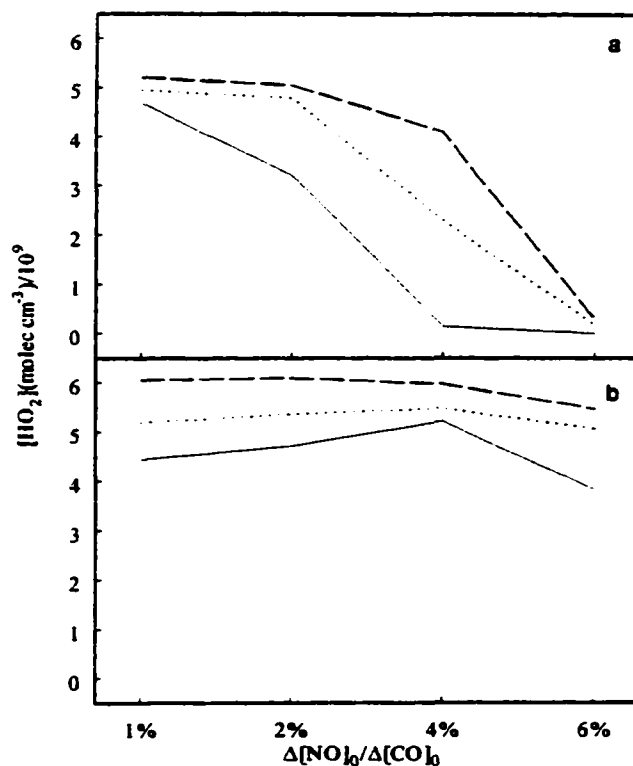


Figure 7.3 Simulated maximum concentrations for HO₂ (molecules/cm³/10⁹) under (a) *No Oxy* conditions and (b) *All Oxy* conditions. $\Delta[\text{CH}_2\text{O}]_0/\Delta[\text{CO}]_0 = 0\%$, solid lines; $\Delta[\text{CH}_2\text{O}]_0/\Delta[\text{CO}]_0 = 2\%$, dotted lines; $\Delta[\text{CH}_2\text{O}]_0/\Delta[\text{CO}]_0 = 4\%$, dashed lines.

The [HO₂] maxima in the *All Oxy* simulations, on the other hand, tend to increase with increasing [NO]₀ up to a ‘threshold’ level, beyond which they decrease (Figure 7.3b). We believe this increase in [HO₂], which is not observed in the *No Oxy* simulations, arises due to

a combination of intertwined effects. The oxygenates tend to be more reactive (with respect to OH) in general than are NMHCs, and hence they act as a source of HO₂ through the basic tropospheric photochemical cycle. This increase in peroxy radical production would have an associated increase in the conversion of NO-to-NO₂ (and HO₂-to-OH), especially as the initial [NO_x] is increased. This conversion could lead to a decrease in HO₂ concentration (as in the *No Oxy* simulations) if there were not an associated conversion of OH back to HO₂, a role fulfilled by the highly reactive oxygenated species. (Thus these two effects are intertwined-the first leads to the second which leads back to the first). Because the basic photochemical cycle can be autocatalytic in radical production, this increase in the photochemical processing can lead to an increase in radical species concentrations in general, and peroxy radicals in particular. (This autocatalysis is associated with O₃ production as well.) Keeping in mind that the *All Oxy* simulations occur under NO_x-sensitive conditions, it is possible that the increased production of radical species (due to the inclusion of the oxygenates) is swamping the system to a degree greater than the initial increase in [NO_x]₀. Since a particular Rad + NO_x reaction can at most remove only one radical per NO_x, the [NO_x] must be at a particular level in relation to the radical production in order to maintain or reduce radical concentrations. Thus, it is only beyond a certain initial concentration that an increase in [NO_x]₀ would cause a decrease in radical species via the Rad + NO_x reactions; this is the effect observed for the [HO₂] maxima in the *All Oxy* simulations.

7.B.3. Summary of Non-Diluting Smoke Plume Simulations

These initial, preliminary simulations indicate that inclusion of oxygenated species 'switched on' alternative reaction pathways which are not present under the *No Oxy*

conditions. These simulations gave first indication of the importance of the oxygenated organic species in smoke-plume photochemistry. They provide the motivation to further develop our smoke-plume model in order to more accurately simulate plume evolution and to investigate in more detail the differences in the fundamental chemical kinetics that lead to the overall simulated results.

7.C. Diluting Smoke Plume

As discussed in sections 6.B and 6.B.1, modifications were made to the original MM code (after the above preliminary simulations were conducted) in order to increase the stability of the numerical solver and to adapt the MM to our particular needs of simulating the temporal evolution of a biomass combustion smoke plume. Briefly, these alterations of the MM code were the conversion of the numerical solver from Gear's method to LSODES and the inclusion of: (1) ambient concentration profiles (for most species); (2) dilution of the smoke plume; and (3) formation of the ammonium nitrate aerosol. With these modifications in place we embarked upon a new collection of smoke plume simulations.

Two basic sets of simulations were conducted as discussed above (*No Oxy* and *All Oxy*) in order to determine the impact of the oxygenated organic species. Additionally each set of simulations was conducted at values of $\Delta[\text{NO}]_0/\Delta[\text{CO}]_0$ of both 1 and 2 % (representing a range of typical values for real biomass combustion) and with perturbed values of HCs (*moreHCs*) in order to evaluate the NO_x/VOC sensitivity. This design allows not only for analysis of the effect of changing initial [VOC] via the increase of initial HCs (as well as the addition of initial concentrations of oxygenated organic species to the smoke profile), but also for analysis of the effect of changing initial $[\text{NO}_x]$. The full span of actual initial

concentrations (*i.e.*, the smoke-plume enhancement concentration plus the ambient concentration) are given in Table 7.2. (Refer to Table 6.1 for ambient concentrations).

Table 7.2 Initial Concentrations in the Smoke Plume (*i.e.*, at 12:00 Noon of First Day) for the *No Oxy* and *All Oxy* Cases.

Name	Formula	Total Concentration (ppbv)
Nitrogen	N ₂	7.8 × 10 ⁸
Nitrogen Dioxide	NO ₂	37.60
Nitric Oxide	NO	75.25 (1%) or 150.5 (2%)
Nitrous Oxide	N ₂ O	335.0
Dinitrogen Pentoxide	N ₂ O ₅	0.005
Nitric Acid	HNO ₃	0.2
Nitrous Acid	HNO ₂	0.03
Ammonia	NH ₃	150.5
Peroxyacetyl Nitrate	PAN	0.05
Hydrogen Cyanide	HCN	15.20
Methane	CH ₄	2260 (<i>No Oxy; All Oxy</i>) or 2870 (<i>MoreHCs</i>)
Ethane	C ₂ H ₆	61.10 (<i>No Oxy; All Oxy</i>) or 108.6 (<i>MoreHCs</i>)
Ethene	C ₂ H ₄	161.6 (<i>No Oxy; All Oxy</i>) or 311.9 (<i>MoreHCs</i>)
Ethyne (Acetylene)	C ₂ H ₂	56.20 (<i>No Oxy; All Oxy</i>) or 103.8 (<i>MoreHCs</i>)
Propane	C ₃ H ₈	28.80 (<i>No Oxy; All Oxy</i>) or 39.03 (<i>MoreHCs</i>)
Propene	C ₃ H ₆	35.80 (<i>No Oxy; All Oxy</i>) or 69.02 (<i>MoreHCs</i>)
Methanol	CH ₃ OH	0.50 (<i>No Oxy</i>) or 150.9 (<i>All Oxy</i>)
Phenol	C ₆ H ₅ OH	0.00 (<i>No Oxy</i>) or 56.10 (<i>All Oxy</i>)
Acetic Acid	CH ₃ COOH	2.10 (<i>No Oxy</i>) or 152 (<i>All Oxy</i>)
Formic Acid	HCOOH	5.40 (<i>No Oxy</i>) or 61.5 (<i>All Oxy</i>)
Formaldehyde	CH ₂ O	9.10 (<i>No Oxy</i>) or 159.5 (<i>All Oxy</i>)
Hydroxyacetaldehyde	CH ₂ (OH)CHO	1.50 (<i>No Oxy</i>) or 57.6 (<i>All Oxy</i>)
Carbon Dioxide	CO ₂	4.5 × 10 ⁵
Carbon Monoxide	CO	7200
Carbonyl Sulfide	OCS	49.30
Sulfur Dioxide	SO ₂	49.00
Oxygen	O ₂	2.1 × 10 ⁸
Ozone	O ₃	29.30
Hydrogen Peroxide	H ₂ O ₂	0.690
Water	H ₂ O	1.0 × 10 ⁷
Hydrogen	H ₂	650.4

Smoke-plume simulations were started at 12:00 (noon) and run for 30 hours. The most dramatic changes occur within the first few hours when the sun is high and the plume

is relatively concentrated. Typical simulated time profiles for $[O_3]$ are shown in Figure 7.4, and the absolute concentrations of several species at 2 PM on days 1 and 2 are listed in Table 7.3 for each of the four emission scenarios. Insight into the effects of oxygenated organic compounds upon early smoke-plume photochemistry are made by comparing results from *All Oxy* simulations to those from *No Oxy* simulations.

Table 7.3 Simulated Species Concentrations (ppbv) in an Aged Smoke Plume at 14:00 on Day 1 and at 14:00 on Day 2

Species	Total Concentrations at 14:00 on Day 1				Total Concentrations at 14:00 on Day 2			
	$\Delta[NO]_0/\Delta[CO]_0 = 1\%$; $\Delta[NO]_0/\Delta[CO]_0 = 2\%$		$\Delta[NO]_0/\Delta[CO]_0 = 1\%$; $\Delta[NO]_0/\Delta[CO]_0 = 2\%$		$\Delta[NO]_0/\Delta[CO]_0 = 1\%$; $\Delta[NO]_0/\Delta[CO]_0 = 2\%$		$\Delta[NO]_0/\Delta[CO]_0 = 1\%$; $\Delta[NO]_0/\Delta[CO]_0 = 2\%$	
	<i>No Oxy</i>	<i>All Oxy</i>	<i>No Oxy</i>	<i>All Oxy</i>	<i>No Oxy</i>	<i>All Oxy</i>	<i>No Oxy</i>	<i>All Oxy</i>
NO ₂	26.6	1.25	57.3	6.24	0.52	0.37	0.68	0.61
NO	3.38	0.08	16.2	0.34	0.06	0.05	0.09	0.07
N ₂ O	328	328	327	328	322	322	322	322
N ₂ O ₅	0.03	0.00	0.02	0.01	0.00	0.00	0.00	0.00
HNO ₄	0.40	0.11	0.10	0.56	0.02	0.01	0.02	0.02
HNO ₃	0.38	0.08	0.38	0.33	0.38	0.23	2.95	0.63
NH ₃	54.5	53.7	56.9	32.8	8.36	13.8	1.04	5.11
NH ₄ NO ₃ (Aerosol)	24.7	32.3	21.2	60.6	43.8	37.4	58.7	70.2
PAN	4.49	6.08	1.58	8.78	2.30	1.65	2.63	2.55
Hydroxy-PAN	1.24	6.89	0.50	8.63	0.68	0.71	0.84	1.08
All PAN Species	6.85	22.1	2.58	28.7	3.61	3.03	4.20	4.77
Mono-substituted								
Nitrophenol	0.00	3.89	0.00	3.13	0.00	0.07	0.00	0.00
Di-substituted								
Nitrophenol	0.00	1.45	0.00	3.03	0.00	2.19	0.00	2.14
HCN	7.53	7.52	7.53	7.52	2.48	2.48	2.48	2.48
CH ₄	1947	1947	1948	1947	1742	1742	1742	1742
C ₂ H ₆	36.3	36.3	36.5	36.1	19.8	20.1	19.9	19.8
C ₂ H ₄	55.2	48.8	66.5	41.5	4.18	6.82	5.23	3.93
C ₂ H ₂	30.8	30.6	31.3	30.1	13.8	14.4	13.9	13.8
C ₃ H ₈	22.5	22.3	23.0	21.8	16.7	17.7	16.7	16.7
C ₃ H ₆	3.94	2.49	7.80	1.45	0.08	0.12	0.07	0.08
CH ₃ OH	0.48	70.1	0.49	68.8	0.57	20.3	0.51	19.0
C ₆ H ₅ OH	0.00	3.09	0.00	1.12	0.00	0.00	0.00	0.00
CH ₃ COOH	2.17	73.1	2.15	72.1	2.23	23.1	2.13	22.1
HCOOH	6.50	34.4	6.34	34.2	7.78	16.5	7.53	16.0
CH ₂ O	39.6	55.1	30.2	59.5	5.01	6.17	5.97	5.89
HOCH ₂ CHO	5.51	14.8	4.50	12.5	1.29	2.35	1.43	1.50
CO	3609	3688	3614	3691	1281	1335	1286	1329
OCS	24.3	24.3	24.3	24.3	7.97	7.97	7.97	7.97
SO ₂	21.7	20.8	22.7	20.1	4.67	5.26	4.98	4.53
O ₃	172	251	85.1	322	138	110	133	148
H ₂ O ₂	0.71	15.5	0.63	6.87	14.3	22.7	13.6	21.5
Organic Peroxides	4.38	9.23	5.08	5.26	7.28	10.7	6.32	8.33

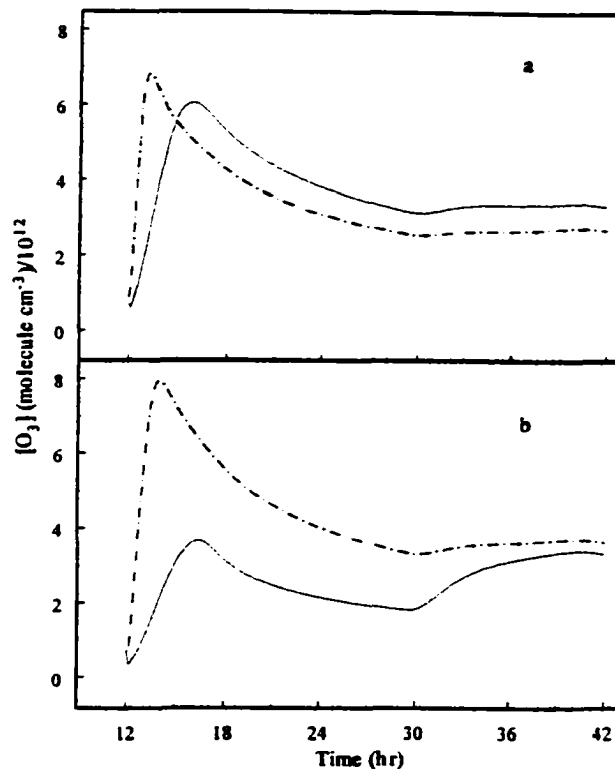


Figure 7.4 Simulated O_3 concentration (molecules/cm³/10¹²) versus time (hours). *No Oxy*, solid lines; *All Oxy*, dotted-dashed lines. (a) $\Delta[NO]_0/\Delta[CO]_0 = 1\%$; (b) $\Delta[NO]_0/\Delta[CO]_0 = 2\%$. Simulations were started at 12:00 (noon) and ran for 30 hours with sunset occurring at ~18 hours on the first day and sunrise occurring at ~6 am (30 hours) on the second day. The decline in concentration after ~16 hours is mainly associated with dilution of the smoke plume.

We report here the relative changes in overall average reaction rates, overall average concentrations, and total species production at the first-day maximum, the end of the first day and the final, 42-hr, values (obtained by multiplying the specified concentrations by the plume volume at that time). Exact numerical values are undoubtedly model dependent [Olson *et al.*, 1997], but we believe these relative values give a reliable account of the effect of the oxygenated organic species on smoke-plume photochemistry.

7.C.1. Overall VOC/NO_x Sensitivity

Addition of the direct emission of oxygenated organic species has a significant impact upon the dominant photochemical processing occurring within a smoke plume, as is observed in the previous, non-diluting photochemical simulations. Table 7.4 details changes in the *No Oxy* and *All Oxy* simulated O₃ and OH production at the first-day maximum owing to a perturbation of the initial concentrations of either hydrocarbons or NO_x.

Table 7.4 Effect of a Given Increase on Total Production (Plume Volume × Concentration) at the First Day Maximum

	Species	<i>No Oxy</i>	<i>All Oxy</i>
Increase NO _x	O ₃	-36%	38%
	OH	-52%	30%
Increase Hydrocarbons	O ₃	12%	7%
	OH	0.3%	-11%
Increase Oxygenated Organics	O ₃	-28%	N/A ^a
	OH	-13%	N/A ^a

^a N/A, not applicable.

The *No Oxy* simulations are characterized as VOC-sensitive owing to the decrease in production of both O₃ and OH as [NO_x]₀ is increased, together with comparable ([OH]) or increased ([O₃]) values resulting from an increase in hydrocarbon concentration. In contrast, the photochemistry within the *All Oxy* simulations is found to be dominated by NO_x-sensitive chemistry, as is demonstrated by a substantial increase in production of O₃ and OH with increasing initial [NO_x]. Thus, inclusion of oxygenated organics causes the dominant photochemistry within the smoke plume to change from VOC- to NO_x-sensitive, similar to the effect seen in the non-diluting smoke-plume simulations.

The source of dominance of VOC-sensitive processing can be understood by looking

at the fraction of radicals lost via reaction with NO_x , as opposed to reaction with other radicals ($\text{Rad} + \text{NO}_x$ and $\text{Rad} + \text{Rad}$ being the two primary pathways for radical loss in the troposphere). *Kleinman et al.* [1994, 1997] and *Daum et al.* [2000] have shown that the fraction of radicals lost via these two pathways provides a very good indication of the sensitivity of O_3 production to O_3 precursors. Their analyses indicate that when the fraction of radicals lost via reaction with NO_x (L_N/Q) takes on a high value and the fraction lost via $\text{Rad} + \text{Rad}$ reactions (L_R/Q) is small (≤ 0.15) VOC-sensitive photochemical processing is dominant. Likewise, when the L_N/Q fraction is low, and the L_R/Q fraction is high, then conditions are NO_x -sensitive.

Figure 7.5 shows both fractions for the simulations reported here. As expected all simulations show the dominance of $\text{Rad} + \text{NO}_x$ reactions at night (> 18 hours in Figure 7.5) due to the nighttime NO_3 chemistry and reduced radical concentrations. Though, by the second day all simulations show a diurnal variation of the classic VOC- to NO_x -sensitive transition that is expected as a plume evolves [*Sillman, 1999*]. An important difference among the traces, however, is the VOC- to NO_x -sensitive transition that occurs on the first day in the *All Oxy* simulations, but which is not present in the *No Oxy* simulations. Thus, while the *No Oxy* simulations are primarily VOC-sensitive, the *All Oxy* simulations are dominated by NO_x -sensitive photochemical processing.

This alteration of the dominate photochemical pathway has interesting consequences for O_3 and OH , as well as for other photochemically important species. While increasing the initial concentration of hydrocarbons in the *No Oxy* simulations leads to increased $[\text{O}_3]$ with little change in $[\text{OH}]$, typical of VOC-sensitive chemistry [*Sillman, 1999*], a comparable

increase in the initial concentrations of oxygenates (comparing the *All Oxy* simulation to the *No Oxy* simulation) leads to substantially decreased concentrations for both of these indicator species (Table 7.4).

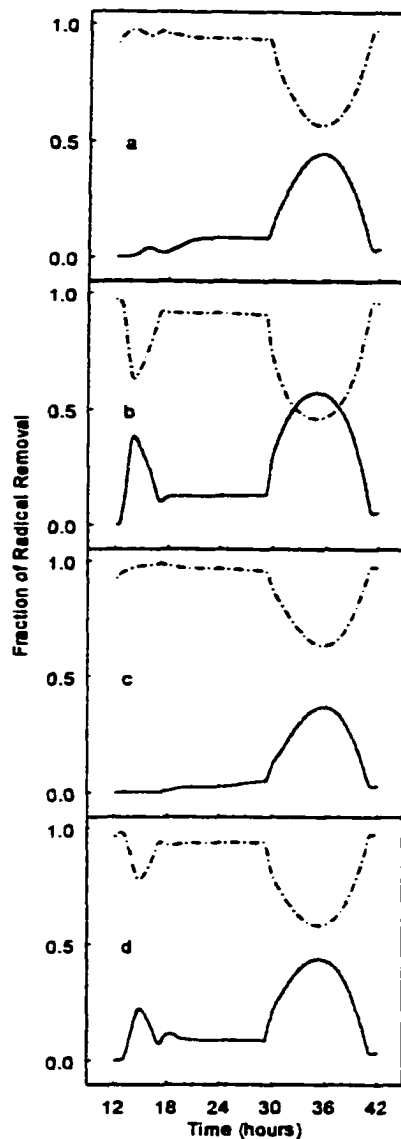


Figure 7.5 Simulated results for fraction of total radical removal via Rad + Rad reactions (solid lines) and Rad + NO_x reactions (dotted-dashed lines). Contributions from other radical removal pathways are not significant. (a) *No Oxy* with $\Delta[\text{NO}]_0/\Delta[\text{CO}]_0 = 1\%$. (b) *All Oxy* with $\Delta[\text{NO}]_0/\Delta[\text{CO}]_0 = 1\%$. (c) *No Oxy* with $\Delta[\text{NO}]_0/\Delta[\text{CO}]_0 = 2\%$. (d) *All Oxy* with $\Delta[\text{NO}]_0/\Delta[\text{CO}]_0 = 2\%$. Values of the Rad + Rad fraction greater than ~ 0.15 are indicative of NO_x sensitive conditions [Kleinman, 1994].

This effect seems to result from differences in the two photochemical processing regimes, and indicates that the more reactive and photochemically active oxygenated organics have a greater impact upon VOC/NO_x sensitivity than do pure hydrocarbons.

7.C.2. Plume Evolution: VOC- to NO_x- Sensitive Transition

Evidence of a transition from VOC- to NO_x- sensitive chemistry occurring during plume evolution, as has been reported for urban plumes, can be seen in the present simulations. *Sillman* [1995] recommends use of the [H₂O₂]/[HNO₃] ratio as a measurable (and therefore verifiable) indicator of VOC/NO_x sensitive chemistry in real atmospheres. This is because high concentrations of HNO₃ reflect VOC-sensitive conditions in which Rad + NO_x termination reactions dominate [*Sillman*, 1995], while H₂O₂ results from Rad + Rad reactions, which are suppressed under VOC-sensitive conditions, but increase linearly with respect to radical production in the NO_x-sensitive state [*Kleinman*, 1994].

In *All Oxy* simulations and the lower-NO_x *No Oxy* simulation, the formation rate of HNO₃ reaches a maximum and dominates Rad + Rad reaction rates (which lead to hydroperoxide production) during the first hours of the simulations (Figure 7.6). The transition takes longer for the *No Oxy* simulations (and does not even occur in the higher-NO_x *No Oxy* case) than for the *All Oxy* simulations. After the first few hours, however, the Rad + Rad reaction rates exceed the HNO₃ production rate (Figure 7.6) indicating a shift from VOC-sensitive to NO_x-sensitive photochemical processing.

The concentration profiles for total hydroperoxides also indicate that as the smoke-plume ages beyond the first few hours, the chemical processing tends to shift from VOC- (decreasing hydroperoxide concentration) to NO_x-sensitive (increasing hydroperoxide

concentration) chemistry (Figure 7.7)

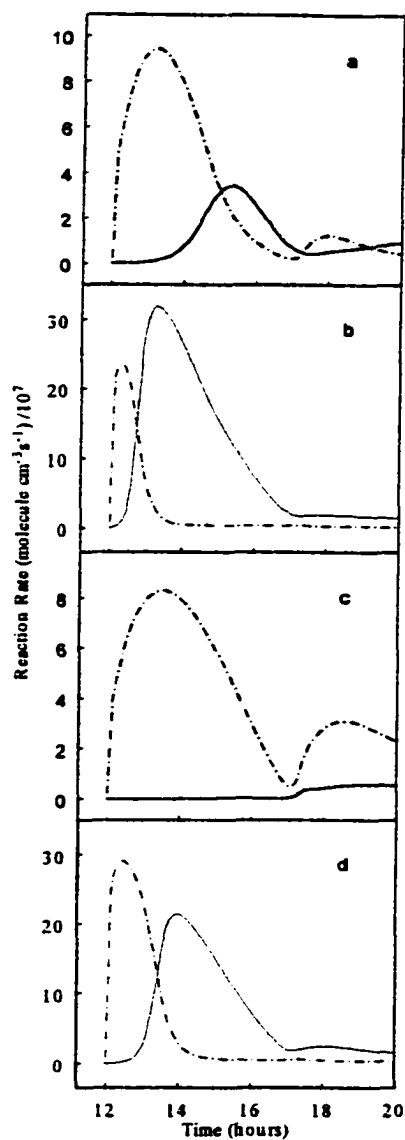


Figure 7.6 Calculated reaction rates ($\text{molecules}/\text{cm}^3 \text{s}/10^7$) versus time (hours) for Rad + Rad reactions (solid lines) and $\text{OH} + \text{NO}_2 - \text{HNO}_3$ (dotted-dashed lines). (a) *No Oxy* with $\Delta[\text{NO}]_0/\Delta[\text{CO}]_0 = 1\%$. (b) *All Oxy* with $\Delta[\text{NO}]_0/\Delta[\text{CO}]_0 = 1\%$. (c) *No Oxy* with $\Delta[\text{NO}]_0/\Delta[\text{CO}]_0 = 2\%$. (d) *All Oxy* with $\Delta[\text{NO}]_0/\Delta[\text{CO}]_0 = 2\%$. Most traces show HNO_3 formation to initially dominate, indicative of VOC sensitive conditions, but the radical recombination reactions eventually surpass HNO_3 formation, signifying a transition to NO_x sensitive conditions.

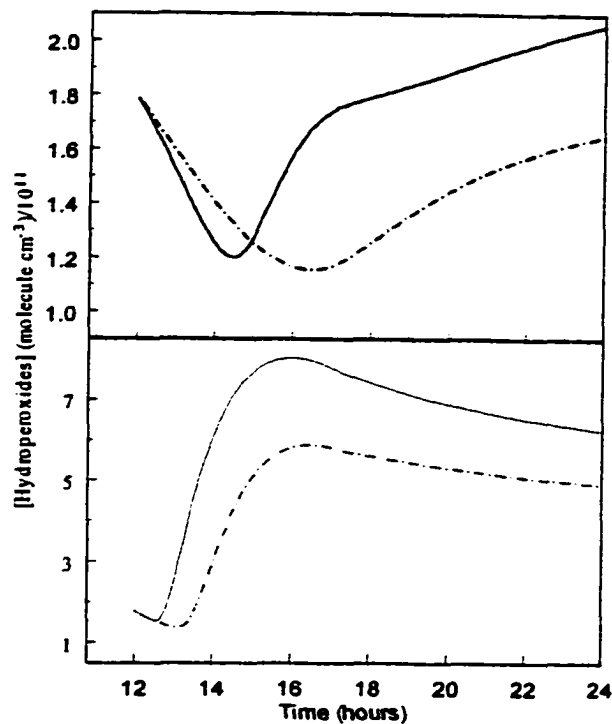


Figure 7.7 Simulated results for total hydroperoxide concentration (molecules/cm³/10¹¹) versus time (hours) for $\Delta[\text{NO}]_0/\Delta[\text{CO}]_0 = 1\%$, (solid line) and $\Delta[\text{NO}]_0/\Delta[\text{CO}]_0 = 2\%$ (dotted-dashed line). (a) *No Oxy*. (b) *All Oxy*. Traces show an initial decline in total hydroperoxide concentration, consistent with VOC-sensitive conditions, followed by a resurgence in their concentration corresponding to NO_x sensitive conditions. The [hydroperoxides] continue to increase on the second day (not shown).

Again this transition takes longer to occur in the *No Oxy* simulations than in the *All Oxy* simulations. While neither of the above conditions define the VOC-sensitive state, they both serve as indications that all of the simulated smoke-plumes are controlled by VOC-sensitive chemistry early in the simulation period (even though the *All Oxy* simulations are in total dominated by NO_x-sensitive photochemical processing).

7.C.3. Decrease in NO_x Lifetime

The passage from VOC- to NO_x- sensitive chemistry occurs due to the removal of

NO_x from the plume [Sillman, 1999]. The lifetime of NO_x, defined as the time over which [NO_x] falls to 1/e of its initial value, is decreased by a factor of ~ 2 due to the addition of oxygenates (Table 7.5).

Table 7.5 Lifetime of NO_x. Calculated as the Time Required for [NO_x] to Fall to 1/e of Its Initial Value

	Simulation	Lifetime (hours)
$\Delta[\text{NO}]_0/\Delta[\text{CO}]_0 = 1\%$	<i>No Oxy</i>	1.57
	<i>All Oxy</i>	0.57
$\Delta[\text{NO}]_0/\Delta[\text{CO}]_0 = 2\%$	<i>No Oxy</i>	2.17
	<i>All Oxy</i>	1.16

This dramatic decrease in the NO_x lifetime is perhaps the most important effect of the oxygenates on smoke-plume photochemistry because it limits the time that NO_x is available to catalyze the production of O₃, thereby affecting the overall oxidizing ability within the smoke-plume. As a side note, [NO_x] decreases in the simulations reported here as a result of dilution with ambient air, as well as by chemical reaction. Undoubtedly the results would differ if such a plume were to mix with NO_x-rich, urban air rather than the relatively NO_x-poor ambient air used here; thus providing the basic motivation for the final set of simulations reported here (chapter 8), that of a smoke plume mixing with an urban environment.

7.C.4. Removal of NO_x

The early dominance of the Rad + NO_x termination reactions (Figure 7.5) leads to rapid removal of NO_x from the smoke-plume. Figure 7.8 details the component reaction rates which make-up the Rad + NO_x reactions. HNO₃-formation is typically the dominant fate of NO_x in the troposphere [Seinfeld and Pandis, 1998], and for the smoke-plume simulations reported here the formation of HNO₃ (Reaction 3.13) is the dominant Rad + NO_x reaction

early in the plume lifetime (Figure 7.8).

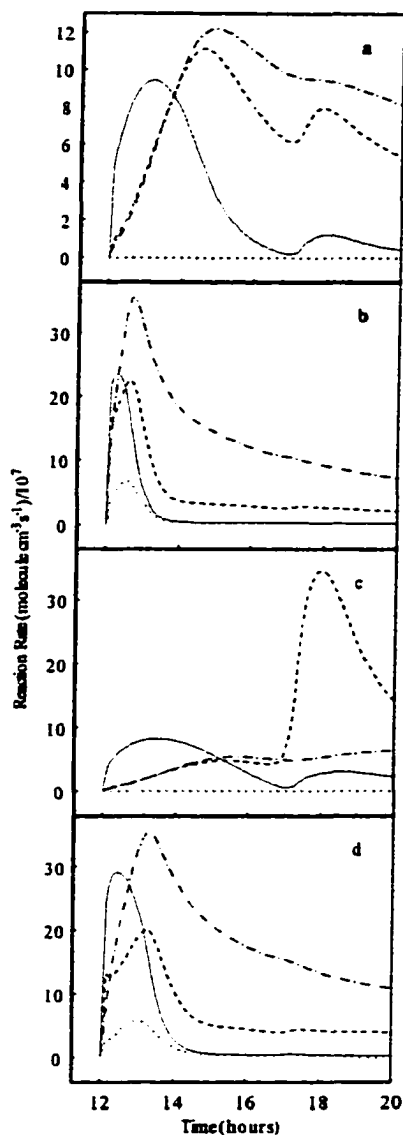


Figure 7.8 Component reaction rates (molecules/cm³ s/10⁷) of the Rad + NO_x reactions. RC(O)O₂ + NO₂ → PANs, dotted-dashed lines; Phenol + NO₂ → Nitrophenols, dotted lines; OH + NO₂ → HNO₃, solid lines; and RO₂ + NO → RONO₂, dashed lines. (a) *No Oxy* with $\Delta[\text{NO}]_0/\Delta[\text{CO}]_0 = 1\%$; (b) *All Oxy* with $\Delta[\text{NO}]_0/\Delta[\text{CO}]_0 = 1\%$; (c) *No Oxy* with $\Delta[\text{NO}]_0/\Delta[\text{CO}]_0 = 2\%$; (d) *All Oxy* with $\Delta[\text{NO}]_0/\Delta[\text{CO}]_0 = 2\%$. All traces show an initial dominance of HNO₃ formation which is eventually surpassed by the formation of PANs and RONO₂. There is an additional contribution to NO_x removal in the *All Oxy* simulations owing to the production of nitrophenols.

However the production of PANs (Reaction 3.14) and organic nitrates (RONO₂) (Reaction 3.15) becomes the dominant NO_x sink as the plume evolves (Table 7.6). The addition of oxygenates leads to a decrease in the formation rates of organic nitrates, while the preference for PANs-formation over HNO₃-production becomes more pronounced upon the addition of oxygenates (Figure 7.8, Table 7.6).

Table 7.6 Average Reaction Rates Over a 30-Hour Simulation and the Percent Change Between *No Oxy* and *All Oxy* Cases With $\Delta[\text{NO}]_0/\Delta[\text{CO}]_0 = 1\%$ and 2% (1% and 2% case).

Reactions	Average Reaction Rates, molecules/cm ³ s				Change, %	
	$\Delta[\text{NO}]_0/\Delta[\text{CO}]_0 = 1\%$		$\Delta[\text{NO}]_0/\Delta[\text{CO}]_0 = 2\%$		1% case	2% case
	<i>No Oxy</i>	<i>All Oxy</i>	<i>No Oxy</i>	<i>All Oxy</i>		
Rad + NO _x (Net) ^a	1.03 × 10 ⁸	9.84 × 10 ⁷	1.17 × 10 ⁸	1.47 × 10 ⁸	-5	26
RC(O)O ₂ + NO ₂ → PANs	5.47 × 10 ⁷	6.45 × 10 ⁷	4.63 × 10 ⁷	9.19 × 10 ⁷	18	98
HO + NO ₂ → HNO ₃	9.55 × 10 ⁶	7.29 × 10 ⁶	1.38 × 10 ⁷	1.45 × 10 ⁷	-24	5
RO ₂ + NO → RONO ₂	3.85 × 10 ⁷	2.36 × 10 ⁷	5.67 × 10 ⁷	3.72 × 10 ⁷	-39	-34
ROH + NO ₂ → Nitrophenols	0.0	3.10 × 10 ⁶	0.0	3.41 × 10 ⁶	N/A ^b	N/A ^b
NO-to-NO ₂ Conversion	1.12 × 10 ⁸	1.09 × 10 ⁸	1.02 × 10 ⁸	1.52 × 10 ⁸	-3	50
CH ₂ O + <i>hν</i>	1.75 × 10 ⁷	3.02 × 10 ⁷	1.66 × 10 ⁷	3.07 × 10 ⁷	72	85
Rad + Rad	2.63 × 10 ⁷	5.51 × 10 ⁷	2.14 × 10 ⁷	4.75 × 10 ⁷	110	122
HO ₂ + O ₃ → HO + 2O ₂	7.86 × 10 ⁶	1.26 × 10 ⁷	4.86 × 10 ⁶	1.43 × 10 ⁷	60	195

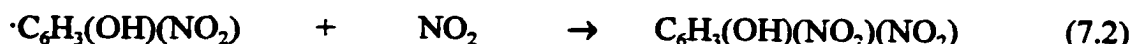
^a the HO₂ + NO₂ = HNO₃ reaction has been excluded because it occurs equally in both directions.

^b N/A, not applicable.

This latter effect has also been noted by *Tanner et al.* [1988] and by *Singh et al.* [1995]. It results, we believe, from an increase in RC(O)O₂ radicals due to the oxidation of aldehyde (and ketone) components of the oxygenates, as well as from a decrease in available OH

(which reacts with NO₂ to form HNO₃) due to increased VOC-loading (Table 7.7). The removal of NO_x into either PANs or HNO₃ is a local effect which has regional and possibly even global implications owing to their role as NO_x-reservoirs.

There is a significant added contribution to NO_x-removal via Rad + NO_x reactions in *All Oxy* simulations due to the formation of nitrophenols (Reactions 7.1 and 7.2).



Unlike PANs and HNO₃, the possibility of re-releasing NO_x from nitrophenols is uncertain [Seinfeld and Pandis, 1998] and they are simply a sink for NO_x in the present model. Nevertheless, their added contribution helps to offset decreases in the formation rates of HNO₃ (for the $\Delta[\text{NO}]_0/\Delta[\text{CO}]_0 = 1\%$ case only) and RONO₂ due to the addition of oxygenates (Table 7.6), and it is quite apparent that nitrophenols represent a significant addition to the product distribution profile within a biomass-combustion smoke-plume. These results suggest that the chemistry of these species should be considered further.

7.C.5. Increase in Radical Species

The addition of oxygenates causes an overall increase in the removal rate of NO_x (via the Rad + NO_x termination reactions) due to an increase in the concentrations of radical species, most notably HO₂ (Table 7.7). A portion of this increase in [HO₂] results from an increase in the photolysis of CH₂O (Table 7.6), which arises both from an increase in the initial concentrations of it and its precursors (*e.g.*, CH₃OH) and a decrease in its removal by OH (due to increased [VOC]-loading). Additionally, radical concentrations are increased because increasing [VOC] within the smoke-plume leads to an increase in the overall rate of

the tropospheric photochemical cycle outlined in chapter 3.B, and this cycle has the capability to produce more radicals than it consumes (see chapter 3.D) [Crutzen, 1995; Holzinger et al., 1999; Field et al., 2000].

Table 7.7 Average Concentrations over a 30-Hour Simulation Period, Total Number of Molecules Present (Plume Volume × Concentration) at the First Day Maximum and After 30 Hours, and Percent Change Between the *No Oxy* and *All Oxy* Cases With $\Delta[\text{NO}]_0/\Delta[\text{CO}]_0 = 1\%$ and 2% (1% and 2% case).

Species	$\Delta[\text{NO}]_0/\Delta[\text{CO}]_0 = 1\%$		$\Delta[\text{NO}]_0/\Delta[\text{CO}]_0 = 2\%$		Change, %	
	<i>No Oxy</i>	<i>All Oxy</i>	<i>No Oxy</i>	<i>All Oxy</i>	1% case	2% case
Concentration, ppbv						
[Total radical species]	0.079	0.113	0.084	0.105	44	25
[OH]	0.00010	0.00007	0.00009	0.00010	-30	13
[HO ₂]	0.043	0.067	0.035	0.062	55	75
[RO ₂ + RC(O)O ₂]	0.036	0.047	0.049	0.043	30	-11
[O ₃]	155	137	105	176	-11	68
[PANs]	6.12	7.04	5.23	10.1	15	93
Total Production at Day 1 Maximum, molecules						
H ₂ O ₂	2.28×10^{26}	1.41×10^{27}	7.90×10^{25}	1.09×10^{27}	519	1275
ROOH	9.24×10^{26}	2.19×10^{27}	7.42×10^{26}	1.68×10^{27}	137	126
HO ₂	4.90×10^{24}	1.04×10^{25}	1.29×10^{24}	1.02×10^{25}	113	690
OH	2.23×10^{22}	1.95×10^{22}	1.08×10^{22}	2.52×10^{22}	-13	135
O ₃	1.63×10^{28}	1.17×10^{28}	1.04×10^{28}	1.61×10^{28}	-28	54
PANs	7.96×10^{26}	1.06×10^{27}	7.67×10^{26}	1.44×10^{27}	34	88
Total Production at End of Day 1, molecules						
H ₂ O ₂	4.31×10^{26}	2.50×10^{27}	1.23×10^{26}	1.89×10^{27}	479	1437
ROOH	1.44×10^{27}	4.37×10^{27}	1.16×10^{27}	3.43×10^{27}	203	197
O ₃	2.67×10^{28}	2.16×10^{28}	1.50×10^{28}	2.81×10^{28}	-19	88
PANs	1.22×10^{27}	1.02×10^{27}	1.25×10^{27}	1.63×10^{27}	-16	30
Total Production at End of 42 Hours, molecules						
H ₂ O ₂	2.45×10^{27}	3.79×10^{27}	2.36×10^{27}	3.60×10^{27}	55	53
ROOH	3.62×10^{27}	5.48×10^{27}	3.38×10^{27}	4.91×10^{27}	51	45
O ₃	2.34×10^{28}	1.90×10^{28}	2.32×10^{28}	2.54×10^{28}	-19	9
PANs	5.03×10^{26}	4.29×10^{26}	5.80×10^{26}	6.64×10^{26}	-15	14

7.C.6. Increase in Hydroperoxides

The increased abundance of radical species due to the addition of oxygenates also increases the Rad + Rad termination reactions (Table 7.6) leading to an increase in overall and maximum hydroperoxide (H_2O_2 and ROOH) production via reactions 3.16 and 3.17 (Table 7.7). This dramatic increase in hydroperoxides represents another oxygenates-based alteration of the product distribution profile and has important implications for regional and global tropospheric chemistry. Hydroperoxides act as a reservoir of HO_x and transport of hydroperoxides from the lower to the upper troposphere has been postulated in order to provide an additional HO_x source required to sustain calculated $[\text{HO}_x]$ levels comparable to those actually measured [Wennberg *et al.*, 1998]. Our results indicate that biomass combustion may represent an important source of hydroperoxides due to photochemical processing within the smoke-plume. Increased H_2O_2 concentrations may have additional significance for heterogeneous chemistry by increasing sulphate aerosol formation and cloud condensation nuclei concentrations [von Salzen *et al.*, 2000].

7.C.7. Net O_3 Production

It has been previously reported that net O_3 -production is largely independent of [VOC] under NO_x -sensitive conditions [Sillman, 1999]. However, our simulations show that the net effect of directly-emitted oxygenates on overall O_3 production is quite complex due to an increase in radical-species concentrations and subsequent increase in the rate of removal of NO_x from the plume via Rad + NO_x reactions.

Because O_3 production ($\text{O}_2 + \text{O}^3\text{P} \rightarrow \text{O}_3$) results from the photolysis of NO_2 (to yield $\text{NO} + \text{O}^3\text{P}$), the decrease in NO_x lifetime due to the addition of oxygenates is mimicked by O_3

production (Table 7.8) under both NO emission scenarios.

Table 7.8 Average O₃ Destruction, O₃ Production, and Net O₃ Production Rates Over a 30-Hour Simulation, and the Percent Change between *No Oxy* and *All Oxy* Cases with $\Delta[\text{NO}]_0/\Delta[\text{CO}]_0 = 1\%$ and 2% (1% and 2% cases).

Reaction	Reaction Rates, molecules/cm ³ s				Change, %	
	$\Delta[\text{NO}]_0/\Delta[\text{CO}]_0 = 1\%$		$\Delta[\text{NO}]_0/\Delta[\text{CO}]_0 = 2\%$		1% case	2% case
	<i>No Oxy</i>	<i>All Oxy</i>	<i>No Oxy</i>	<i>All Oxy</i>		
O₃-Destruction						
Individual Reactions						
<i>hν</i> + O ₃ → O(³ P)	8.48 × 10 ⁸	8.31 × 10 ⁸	6.41 × 10 ⁸	1.04 × 10 ⁹	-2	62
<i>hν</i> + O ₃ → O(¹ D)	6.41 × 10 ⁷	6.63 × 10 ⁷	5.05 × 10 ⁷	8.06 × 10 ⁷	4	60
NO + O ₃ → NO ₂ + O ₂	9.63 × 10 ⁸	3.34 × 10 ⁸	1.92 × 10 ⁹	8.64 × 10 ⁸	-65	-55
NO ₂ + O ₃ → NO ₃ + O ₂	1.15 × 10 ⁷	5.49 × 10 ⁶	1.90 × 10 ⁷	1.22 × 10 ⁷	-52	-36
NO ₂ + O ₂ → NO + 2O ₂	3.48 × 10 ⁵	1.66 × 10 ⁵	5.76 × 10 ⁵	3.71 × 10 ⁵	-52	-36
HO + O ₃ → HO ₂ + O ₂	6.38 × 10 ⁵	4.46 × 10 ⁵	4.18 × 10 ⁵	7.83 × 10 ⁵	-30	88
HO ₂ + O ₃ → HO + 2O ₂	7.86 × 10 ⁶	1.26 × 10 ⁷	4.86 × 10 ⁶	1.43 × 10 ⁷	60	195
C ₂ H ₄ + O ₃ → ^a	2.89 × 10 ⁶	3.64 × 10 ⁶	2.40 × 10 ⁶	3.49 × 10 ⁶	26	46
C ₃ H ₆ + O ₃ → ^a	8.55 × 10 ⁵	1.20 × 10 ⁶	7.85 × 10 ⁵	9.83 × 10 ⁵	41	25
ud41 + O ₃ → ^{ab}	0.00	8.46 × 10 ²	0.00	6.54 × 10 ²	N/A ^c	N/A ^c
Combined Reactions						
Total Photolysis	9.12 × 10 ⁸	8.97 × 10 ⁸	6.92 × 10 ⁸	1.12 × 10 ⁹	-2	61
Total NO _x	9.75 × 10 ⁸	3.39 × 10 ⁸	1.94 × 10 ⁹	8.77 × 10 ⁸	-65	-55
Total HO ₂	8.50 × 10 ⁶	1.31 × 10 ⁷	5.28 × 10 ⁶	1.51 × 10 ⁷	54	187
Total VOC	3.75 × 10 ⁶	4.84 × 10 ⁶	3.18 × 10 ⁶	4.48 × 10 ⁶	29	41
Total O ₃ Destruction	1.90 × 10 ⁹	1.25 × 10 ⁹	2.64 × 10 ⁹	2.01 × 10 ⁹	-34	-24
Total O₃ Production						
From O ₂ +O(¹ P) → O ₃	1.98 × 10 ⁹	1.33 × 10 ⁹	2.69 × 10 ⁹	2.11 × 10 ⁹	-33	-22
Net O ₃ Production	7.56 × 10 ⁷	7.65 × 10 ⁷	5.22 × 10 ⁷	1.00 × 10 ⁸	1	92

^aFirst product is an epoxide leading eventually to carbonyl compounds.

^bHere ud41 = HCOCH = CHCHO.

^cN/A, not applicable.

Net O₃ production, however, takes into account changes in O₃-destruction, as well as O₃-production. In the MM there are a total of 20 O₃ destruction reactions. The primary O₃-destruction reaction rates, combined as in Table 7.8, are shown in Figure 7.9. Overall O₃-destruction decreases due to the addition of the oxygenates for both NO emission scenarios

(Table 7.8). This is mainly due to a decrease in the $\text{NO}_x + \text{O}_3$ reactions (Table 7.8), an effect that naturally follows from the decrease in NO_x lifetime. This decrease in O_3 -destruction due to reaction with NO_x is slightly counter-acted by an increase in O_3 -destruction due to reaction with HO_2 (Table 7.8). Both *Field et al.* [2000] and *Crutzen* [1995] have noted the importance of the $\text{HO}_2 + \text{O}_3$ reaction with respect to O_3 -depletion in NO_x -poor environments. Hence both O_3 -destruction and O_3 -production are reduced due to the addition of the oxygenated organic species, and net O_3 production results from a balancing of these two effects.

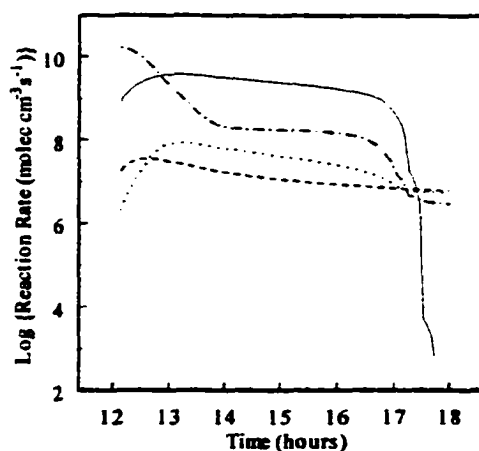


Figure 7.9 Log of combined O_3 destruction reaction rates (molecules/ $\text{cm}^3 \text{s}$) versus time (hours) for the *All-Oxy*, $\Delta[\text{NO}]_0/\Delta[\text{CO}]_0 = 1\%$, simulation. Total photolysis, solid line; total NO_x , dotted-dashed line; total HO_x , dotted line; total VOC, dashed line.

7.C.8. Complex Effects on O_3 and OH

In the lower initial- $[\text{NO}_x]$ simulations ($\Delta[\text{NO}]_0/\Delta[\text{CO}]_0 = 1\%$), the increased removal of NO_x due to the addition of oxygenates causes a decrease in the average NO -to- NO_2 conversion rates (Table 7.6) and thus a decrease in the concentrations and production of O_3 and OH (Table 7.7). However, in the higher initial- $[\text{NO}_x]$ models the increased removal of

NO_x is balanced by its increased initial concentration, and the average NO-to- NO_2 conversion rates are in fact increased (Table 7.6), and so are $[\text{O}_3]$ and $[\text{OH}]$ (Table 7.7). Therefore, unlike previous VOC- NO_x models which found little dependence of O_3 production upon VOC emissions under NO_x -sensitive atmospheric processing conditions [Sillman, 1999], the smoke-plume simulations reported here indicate a very complex relationship between O_3 formation and the initial concentrations of, at least, oxygenated organic compounds. Under certain conditions an increase in $[\text{VOC}]$ through the addition of oxygenated organic species leads to an overall decrease in net O_3 production, while under other circumstances an equivalent increase in $[\text{VOC}]$ leads to an increase in net O_3 production. The overall relationship between $[\text{VOC}]$ and O_3 production is dictated by the available NO_x , as might be expected from the NO_x -sensitive conditions that dominate the oxygenated smoke-plume photochemical simulations presented here. We believe the complexity that arises in the VOC- O_3 relationship due to the direct emission of oxygenated organic species occurs not only because of increased VOC-loading by highly reactive species to the system, but also because of the ability of oxygenates to photolyze, a pathway which is not available to hydrocarbons, leading to a direct source of radical species.

7.C.9. Comparison to Measurements

It is difficult to make valid quantitative comparisons between existing field measurements and our calculated species-concentrations. This is because of simplifications within our model and the rarity of appropriate measurements in isolated plumes only hours old. In order to keep the number of reactions manageable, while taking advantage of the detailed chemistry of the MM, we have restricted VOCs to lighter species containing three

or less carbon atoms. These lightweight compounds probably represent the majority (by molecule) of HC emissions [Lobert *et al.*, 1991; Hao *et al.*, 1996], but they do not account for the full range of typical emissions. Additionally, our assumed clear-sky conditions could only be strictly representative of the upper-levels of a smoke-plume. Finally, our model neglects aerosol chemistry, which undoubtedly is a significant perturbation considering the high water solubility of some product species (*e.g.*, hydroperoxides), as well as the high concentrations (up to milligrams/m³) of particulates and water vapor present in a smoke-plume.

In light of these and other assumptions, our main purpose then is to compare the results of smoke-plume simulations obtained using a standard initial profile of chemical species with and without added oxygenated organic species. The major result of added oxygenates is found to be increased production of nitrophenols and PANs (Table 7.7) leading to a decrease in NO_x lifetime within the smoke plume (Table 7.5). Validation of these results would require accurate measurements of these organic species in biomass-combustion affected air. We are aware of no such data, and our results suggest the need for measurement of these species, as well as investigation of their tropospheric chemistry.

Despite these difficulties, it is possible to make some comparisons. To begin with, our modeled enhancement ratios for the *All Oxy* simulations follow the general trends discussed in section 2.D.4. Enhancement ratios for individual NMHCs, CH₂O, NO_x, and NH₃ generally decrease as the plume ages, while ratios for O₃, hydroperoxides, and formic acid generally increase. These trends are discussed in more detail below, and some are compared to absolute measured values.

Goode et al. [2000] reported evidence of an initial, very rapid decrease in $\Delta[\text{NH}_3]/\Delta[\text{CO}]$ (with a lifetime of 2.5 hr) in downwind measurements of Alaskan smoke plumes. While our predicted lifetime for this ratio is somewhat longer than this, the initial rapid decline is clearly present, especially in *All Oxy* simulations. That is, while there is a decline in the NH_3 enhancement ratio in the *No Oxy* simulations, it is much more prolonged. Additionally, while both the *All Oxy* and the *No Oxy* simulations show an increase in $\Delta[\text{HCOOH}]/\Delta[\text{CO}]$ as the plume evolves, the *All Oxy* simulated ratio is consistently 5 times higher than the *No Oxy* simulated ratio and therefore in much closer agreement with reported values [*Goode et al.*, 2000; *Mauzerall et al.*, 1998]. Although our calculated absolute values of this ratio for the *All Oxy* simulations still do not agree quantitatively with the limited observations available, this is not surprising as our model was not designed to specifically replicate either situation.

Our calculated values for (*All Oxy*) excess H_2O_2 in Table 7.3 are reasonably close to the 10 ppbv obtained in limited measurements “near” biomass-combustion plumes at altitudes less than 2 km during TRACE-A as reported by *Lee et al.* [1998]. This agreement is obtained without assuming any direct production of H_2O_2 from the fire itself. This is consistent with TRACE-A analysis by *Mauzerall et al.* [1998], who reported an inability to find evidence of direct emissions of hydroperoxides from biomass combustion, but indicated that their net photochemical production within the smoke-plume is sufficient to maintain enhancement ratios significantly above ambient, as is also found in our simulations, particularly in the *All Oxy* case.

Our calculated values of $\Delta[\text{O}_3]/\Delta[\text{CO}]$ of $\approx 6\%$ (for the $\Delta[\text{NO}]_0/\Delta[\text{CO}]_0 = 1\%$ case)

and $\approx 8\%$ (for the $\Delta[\text{NO}]_0/\Delta[\text{CO}]_0 = 2\%$ case) after 2.5 hr of photochemical processing are consistent with the $7.9 \pm 2.4\%$ $\Delta[\text{O}_3]/\Delta[\text{CO}]$ measured 2.2 ± 1 hrs downwind in Alaskan smoke plumes with an average $\Delta[\text{NO}]_0/\Delta[\text{CO}]_0$ of $\approx 1.5\%$ [Goode *et al.*, 2000]. Furthermore, the inclusion of oxygenated species substantially improves agreement between simulation and measurement; that is, *No Oxy* simulations predict a $\Delta[\text{O}_3]/\Delta[\text{CO}]$ of only 2-4% after 2.5 hr of processing.

While there is not yet an experimental data set with sufficient detail to wholly determine if the simulations are more accurate with or without oxygenates, based upon the limited number of examples above, when a comparison is possible, the addition of oxygenates to simulations does seem to improve agreement with measurement.

7.C.10. Summary of Diluting Smoke-Plume Simulations

Oxygenated organic compounds have been reported to be ubiquitous components of urban atmospheres and the free troposphere [Lewis *et al.*, 2000; Singh *et al.*, 1995; Tanner *et al.*, 1988], as well as the biomass-combustion smoke-plumes central to the work reported here. We have incorporated six oxygenates (formaldehyde, acetic acid, formic acid, methanol, phenol, and hydroxyacetaldehyde) that have been identified to be present in the largest amounts in biomass-combustion emissions [Griffith *et al.*, 1991; Yokelson *et al.*, 1996a, 1996b, 1997, 1999a; Goode *et al.*, 1999, 2000], into photochemical simulations of the evolution of a smoke-plume. There remain oxygenated and hydrocarbon-based species, such as terpenes, present in biomass combustion smoke [Yokelson *et al.*, 1996; Goode *et al.*, 1999] which have not been included in the simulations reported here due mainly to uncertainties in their abundance and photochemistry.

The primary effect of the addition of oxygenated organic species into biomass-

combustion smoke-plumes is to cause a decrease in NO_x -lifetime by a factor of ~ 2 via $\text{Rad} + \text{NO}_x$ termination reactions. The formation of PANs and nitrophenols represent a significant portion of the increase in $\text{Rad} + \text{NO}_x$ reactions due to oxygenate addition. Since *All Oxy* simulations occur under primarily NO_x -sensitive conditions, the increased availability of radicals also leads to an increase in hydroperoxide concentrations via $\text{Rad} + \text{Rad}$ termination reactions. The increase in hydroperoxides, as well as the preference for PAN-formation over HNO_3 , are of interest as these species are longer-term pollutant reservoirs of HO_x and NO_x , respectively, released into a regional atmosphere by biomass combustion.

The depletion of NO_x (via the addition of oxygenated organic species) to an environment which is already NO_x -sensitive results in complex behavior of $[\text{O}_3]$ and $[\text{OH}]$, depending upon initial $[\text{NO}_x]$. When the initial $[\text{NO}_x]$ is large enough to compensate for the increased removal of NO_x , the addition of oxygenates leads to an overall increase in the NO -to- NO_2 conversion reactions and therefore an increase in O_3 and OH (as shown in the $[\text{NO}]_0/[\text{CO}]_0 = 2\%$ simulations reported here). However, lower initial- NO_x concentrations may not be able to compensate for the increased removal of NO_x , leading to a decrease in NO -to- NO_2 conversion and a subsequent decrease in O_3 and OH (as exemplified in the $[\text{NO}]_0/[\text{CO}]_0 = 1\%$ simulations reported here). This intriguing result is contrary to previous VOC-NO_x models which show little dependence of O_3 production on $[\text{VOC}]$ under NO_x -sensitive conditions. This difference is attributed to the ability of the oxygenates to photolyze resulting in an additional direct source of radical-species which may not be compensated for by the $[\text{NO}_x]$ emissions.

These results demonstrate that directly-emitted oxygenated organic species alter the product distribution profile, including affecting longer-lived species such as O_3 , PANs, and

hydroperoxides. Hence, simulations intending to predict the quantities of various pollutants injected into regional atmospheres by biomass combustion, as well as those looking to understand the effects of biomass combustion on a global scale, need to include both direct emissions of oxygenated organic materials and a good estimate of initial $[\text{NO}_x]$.

Chapter 8

Results of Urban Simulations

8.A. Basis

The previous simulations of the photochemistry occurring within biomass-combustion smoke plumes show a rapid removal of NO_x , causing conditions within the plume to become quickly NO_x -sensitive. Because this removal of NO_x occurs due to plume dilution, as well as photochemistry, we naturally questioned what the effect would be of a NO_x -poor smoke-plume mixing with a NO_x -rich urban environment. Thus, we extended our modeling of biomass-combustion smoke plumes by building an urban model and allowing advection of a smoke plume into the urban airshed, a scenario which is fairly common within the United States. Owing to the Western Montana fires of 2000, we chose to use the Missoula valley as a representative example of such an occurrence. During these fires, smoke was funneled up the Bitterroot valley and entered the Missoula urban airshed. On occasion the smoke tended to remain within the airshed for some time before being advected out owing to overriding stagnant conditions. Hence our main purpose was to build a realistic urban model and conduct two sets of simulations in order to deduce: 1) the effect of the urban atmosphere upon smoke-plume chemistry; and 2) the impact of the (pre-processed) smoke-plume emissions upon the urban environment.

8.B. Urban Modeling

As discussed in section 6.B.2, we model the urban airshed using a simple (0-D) Eulerian box with planetary boundary layer (PBL) height variation (see Figure 6.1). The model uses the same mechanism of 702 reactions, the same photolytic data, and the same ambient air conditions as used in the diluting smoke-plume simulations. The wind speed was chosen to be 1 mile hr^{-1} in order to represent stagnant conditions. Standard deposition rates are given in Table 6.2 and source emissions rates were calculated at every time step according to equation 6.6 based upon reported Missoula city vehicular emissions (as described in 6.B.2).

There exists within our urban model a diurnal variation of both source emissions and the height of the PBL. This has the effect that while urban emissions are greater in the afternoon than in the morning (see Figure 6.2), the boundary layer height is also greater in the afternoon (see Figure 6.1), causing morning emissions to have a greater relative impact upon the urban atmosphere than do those occurring later in the day (Figure 8.1).

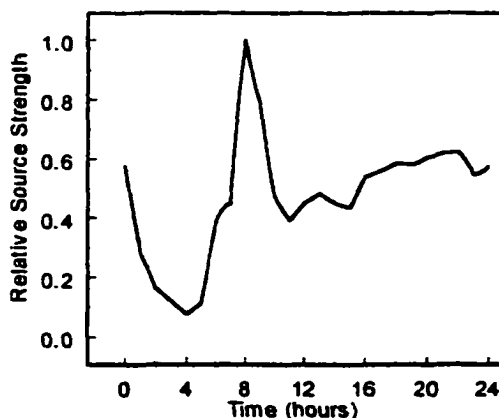


Figure 8.1 Effective source strength (*i.e.*, emission rate per unit volume) relative to the maximum as a function of time of day. This trace shows that while the morning emission rate is smaller than the afternoon rate, its effective impact upon the urban environment is greater owing to the lower height of the planetary boundary layer at that time.

This effective source strength, *i.e.*, the emission rate per unit volume, is depicted in Figure 8.1 on a relative (to the maximum rate) scale. Choosing a relative scale allows the depicted source strength to be independent of species identity. The impact of PBL height variation on source emission strength has important implications for the diurnal profiles of urban source species as present below.

8.B.1 Standard (VOC-Sensitive) Urban Model

Urban simulations using suitable source rates were initiated using ambient concentrations (see Table 6.1 for diurnally constant ambient conditions) and were allowed to run until a steady state was achieved (typically one day). The resulting steady-state diurnal variation for some tropospherically important species are shown in Figure 8.2.

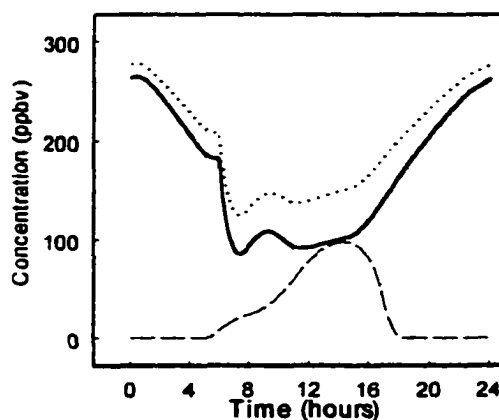


Figure 8.2 Diurnal variation of concentrations (ppbv) in the standard urban model for NO_x (solid line), NMHCs (dotted line), and O₃ (dashed line).

In this diagram [NO_x] and [VOCs] generally build-up during the night owing to emission in the absence of the highly active daytime photochemistry. The profiles of these primary emissions do begin to decrease after midnight as a result of their declining source strengths (Figure 8.1), coupled to replacement of urban air via advection of ambient concentrations into

the airshed. During the day, NO_x and VOC concentrations generally decrease further, owing to the tropospheric photochemical reaction cycle, leading to the production of secondary pollutants, most notably an afternoon (~ 2 pm) maximum in $[\text{O}_3]$ of ~ 100 ppbv. The influence of the relative source strength diurnal variation in the primary emissions of NO_x and VOCs is apparent by the morning (~ 8 am) 'bump' and the slow afternoon increase in the concentrations of these species.

Other important profiles that are not shown in Figure 8.2 are those for OH and HO_2 , which follow the same general behavior as O_3 . Additionally, while NO_2 concentrations (not shown) are substantial in the afternoon, the majority of O_3 has been depleted (predominately due to photolysis and reaction with NO, coupled with a decrease in photochemical production) by the time sunset occurs (~ 6 pm), thereby restricting NO_3 radical production. NO_3 concentrations (not shown) remain low (< 0.5 ppt) throughout most of this standard urban simulation, causing an inhibition of nighttime chemistry.

In comparison to the smoke-plume modeling results, primary emitted species, such as NO_x and VOCs, generally have greater concentrations within the urban environment than within the smoke plume. While, on the other hand, most intermediate, secondary, and end-product tropospheric species (*i.e.*, OH, HO_2 , O_3 , PANs, HNO_3 , and H_2O_2) have lower concentrations within the urban model than those calculated in the smoke model. These differences between the two models can be attributed to the dominate photochemical processing. That is, conditions within the smoke plume are governed by NO_x -sensitive chemistry, while those for the urban model are VOC-sensitive (as described in more detail below). Recall that the VOC-sensitive state is characterized by an overall reduced oxidizing

capacity as compared to the NO_x -sensitive state due to the limited availability of radical species. Under urban conditions the diurnal supply of NO_x due to vehicular emissions acts to deplete radical species concentrations, owing to the $\text{Rad} + \text{NO}_x$ reactions, as compared to the NO_x poor smoke plume. The limited availability of radical species acts in turn to keep O_3 and hydroperoxide concentrations low as a result of limited NO -to- NO_2 conversion and reduced $\text{Rad} + \text{Rad}$ reactions. These results are to be expected and lend confidence to the validity of the urban model.

8.B.2. O_3 Isopleth

The chemistry connecting the primary emissions, VOCs and NO_x , to the concentrations of secondary pollutants such as O_3 is very complex. A result of this complex chemistry is that the concentrations of secondary species are related to those of their precursors in ways that are, under many conditions, highly nonlinear. The dependence of O_3 production on the initial amounts of VOCs and NO_x is frequently represented by means of an O_3 -isopleth diagram. Such a diagram is a contour plot of daily maximum O_3 concentrations as a function of available VOCs and NO_x .

We began testing and investigating the urban model by scaling our source-emissions of NO_x (from 0.1 to 2.2) and VOCs (from 0.2 to 3.2) in order to create an O_3 isopleth diagram (Figure 8.3). (Note that a scaling of 1 for VOCs and NO_x represents the standard urban model as used in the previous section and in the 'urban plus smoke' simulations presented later). Our diagram compares well with those obtained from other models [see, for example, *Finlayson-Pitts and Pitts, 2000; Sillman, 2000; Seinfeld and Pandis, 1998*]. O_3 isopleths, such as Figure 8.3, clearly depict the nonlinear behavior of O_3 production and are

useful for describing VOC/NO_x sensitivity.

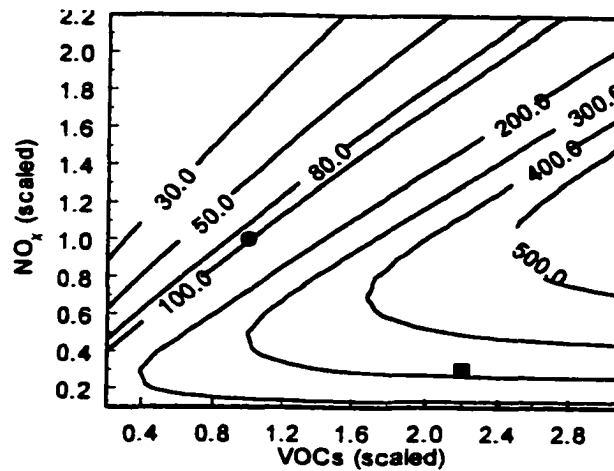


Figure 8.3 O₃-isopleth diagram (indicated isopleth concentrations are in ppbv) obtained using the urban model with scaled values of NO_x and VOC source emissions. Conditions for the standard urban model are denoted with the filled circle (VOC-sensitive), while those used in a 'scaled' urban model (discussed later) are marked by the filled square (NO_x-sensitive).

The lower, right-hand portion of the diagram depicts a region in which increasing the emission of NO_x leads to an increase in [O₃], while increasing VOC-loading has little effect upon [O₃]. Hence, model conditions which fall within this region of the diagram are processing under NO_x-sensitive conditions. On the other hand, the upper portion of the plot shows that an increase in VOCs causes an associated increase in O₃ production, while increasing NO_x causes a decrease in [O₃]. These two effects characterize an airshed to be VOC-sensitive. Since conditions within the standard urban model fall within this region of the diagram, the urban model is supposed to be VOC-sensitive, as is expected for an urban environment.

It is also interesting to note that O₃ production under VOC-sensitive processing tends to be lower in general than under NO_x-sensitive conditions (Figure 8.3). This effect can likely be attributed to the need for NO_x emissions, which are primarily in the form of NO, to be

converted to NO_2 in order to obtain net O_3 production. Under VOC-sensitive conditions there exists an inadequate supply of peroxy radical species to perform this conversion leading to an inhibition of O_3 production. However, under NO_x -sensitive conditions radicals are readily available, leading to rapid conversion of NO -to- NO_2 and increased net O_3 production.

In preparing the O_3 isopleth, it became apparent that as the emissions of NO_x are decreased and/or the emissions of VOCs are increased, the $[\text{O}_3]$ maxima occurs later in the day (Figure 8.4).

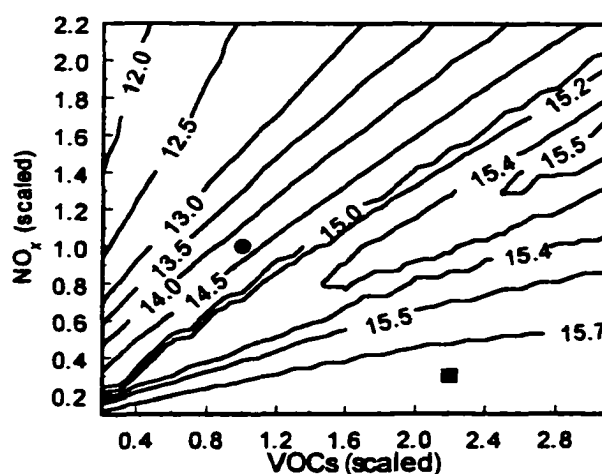


Figure 8.4 Isopleth diagram showing the time of day (hours) of the $[\text{O}_3]$ maximum (depicted in Figure 8.3) as a function of scaled NO_x and VOC emissions. Standard urban model, filled circle (VOC-sensitive); scaled urban model (discussed in 8.B.3), filled square (NO_x -sensitive).

This delay in the O_3 maxima, in addition to the general increase in O_3 production under NO_x -sensitive conditions, has important implications for nighttime chemistry. The production of NO_3 , the primary tropospheric oxidant in the absence of photolytic free radical sources, requires a simultaneous lack of NO and presence of both NO_2 and O_3 in an airmass. The later in the day the O_3 maximum occurs, and the larger the maximum is, the more likely there will be significant concentrations of O_3 available after sunset, thereby increasing the probability

of producing substantial amounts of NO_3 , and hence enhancing nighttime chemistry. As a means of testing this hypothesis, as well as our urban model, we investigated this effect by scaling our standard urban model, as described below.

8.B.3. Scaled (NO_x -Sensitive) Model

The impact of the time and magnitude of the O_3 maximum upon NO_3 concentration is illustrated in Figure 8.5, which shows the diurnal variations for NO_x , VOCs, O_3 and NO_3 in a scaled urban model.

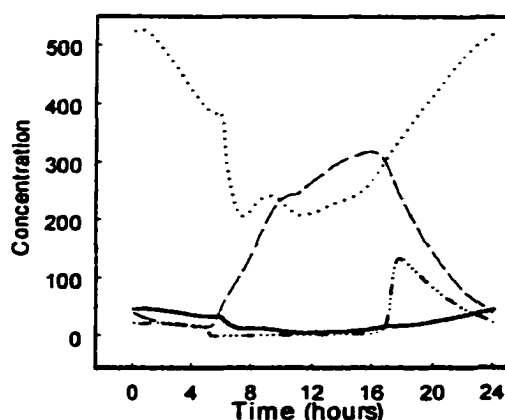


Figure 8.5 Diurnal variation of species concentrations in the scaled urban model for NO_x (ppbv), solid line; NMHCs (ppbv), dotted line; O_3 (ppbv), dashed line; and NO_3 (pptv), triple dot-dashed line.

By scaling the emission factors of VOCs by 2.2 and NO_x by 0.3 (*i.e.*, approximately doubling VOC emissions and halving NO_x emissions into the urban airshed throughout the day), we have shifted the time of the O_3 maximum from ~ 2 pm to ~ 4 pm (Figure 8.4), as well as shifting the overall photochemical processing from VOC-sensitive to NO_x -sensitive (Figure 8.3). This change in overall dominant photochemistry causes a substantial increase (\sim triple) in the $[\text{O}_3]$ maximum. This increase in the $[\text{O}_3]$ maximum, coupled with the delay in the time

of the peak, causes significant amounts of O_3 to become available throughout the night, leading to substantial nighttime concentrations of NO_3 . NO_3 peaks at ~ 150 ppt and remains above 25 ppt between sunset and sunrise in this scaled urban model, as opposed to peaking at ~ 2.5 ppt and otherwise remaining near 0 in the standard urban model. This affects not only nighttime VOC-oxidation, but also leads to a decrease in $[NO_x]$ even below that expected due to the decrease in emission factor (*i.e.*, the emission factor has decreased by a third, but $[NO_x]$ is decreased by a fifth) because NO_3 and its subsequent oxidative products represent added temporary sinks of NO_x .

8.B.4. Summary of Urban Modeling

Considerable effort has been applied to investigating the behavior of the urban model under various emission scenarios. The effects observed under differing emission conditions can be rationalized based upon the basic tropospheric cycle and known processing states, and are consistent with previous analyses [*Finlayson-Pitts and Pitts, 2000; Seinfeld and Pandis, 1998; Wayne, 1991*]. Predicted concentrations of tropospherically important species (*i.e.*, NO_x , O_3 , HO_x) are consistent with expected values, and the chemistry within the urban environment has been shown to be VOC-sensitive as would be expected. All of these features lend confidence to the model as representing a typical urban environment, suitable for use in an investigation of mixing between smoke plumes and urban airsheds.

8.C. 'Urban plus Smoke' Modeling

There are many variables which could be considered in the mixing of a smoke plume with an urban airshed. For example, on what time scale does the mixing process occur? How long have the smoke emissions been processed before encountering the urban airshed? At

what time of day does the processed smoke arrive in the city? What is the effect of the diurnal variation in smoke emissions and processed smoke concentrations? How quickly is the smoke plume advected into the city? And so forth. Some of these questions are beyond the scope of our modeling work; that is, they cannot be addressed within the approximations of our model. For instance, the time scale of mixing cannot be investigated within our well-mixed box approximation. Other variables have been fixed in order to reduce the complexity of the calculation (*e.g.*, the wind speed is set to 1 mile an hour). Nevertheless, there are other aspects of the problem that we have attempted to investigate within this simple modeling framework.

Beyond the large number of detailed variables, there are two major conceptual vantage points from which the mixing of a smoke plume with an urban airshed can be viewed: 1) the effect of the smoke contents on the urban chemistry, and 2) the effect of the urban emissions on the smoke-plume chemistry. Because we are using a simple 0-D box model (*i.e.*, with no spatial resolution), we have dealt with each of these viewpoints separately using different modeling techniques.

8.C.1. Effect of the Smoke on the Urban Airshed

In order to investigate the impact of the smoke plume upon urban chemistry, we initiated an urban simulation as above. On the third day, after the urban environment had reached a steady state, we changed the background ambient concentrations (Table 6.1) to smoke plume concentrations, such that, rather than 'clean' air being advected in, 'smokey' air was mixed in instead. We considered two main variables under this basic scenario: 1) the time of travel of the smoke plume (*i.e.*, the amount of time the initial smoke emissions had

to process before encountering the urban environment), and 2) the time at which the smoke plume arrives at the city.

8.C.1.a. Smoke Plume Time-of-Travel

We considered three lengths of time for the chemical processing of the initial smoke plume before reaching the city: 3 hr, 10 hr, and 15 hr. Because the wind speed is fixed at 1 mile an hour, these times represent distances of 3, 10, and 15 miles between the fire and the city. We assume that the initial fire emissions do not vary in time and are given by Table 7.2 (*All Oxy*, $\Delta[\text{NO}]_0/\Delta[\text{CO}]_0 = 2\%$). However, there will be a diurnal variation to the 'smokey' concentrations which are advected into the city. That is, emissions released at 1 AM will arrive at the city at 4 AM while those emitted at 1 PM will arrive at 4 PM. Between these two scenarios there will be a very substantial difference in the chemical speciation because the former is processed solely at night, while the latter is processed completely during the day, and therefore includes the influence of photolysis reactions. Thus, we conducted a series of smoke-plume simulations in order to determine the diurnal variation of the processed smoke concentrations for each specified time of travel (*i.e.*, 3 hr, 10 hr and 15 hr).

For each time of travel we carried out a total of 95 simulations. The simulations started every fifteen minutes from midnight (hour 0) to 11:45 PM and were of duration equal to the travel time. At the end of each simulation the final smoke plume concentrations for all species were tabulated. Referencing these values allowed determination of the diurnal variation of 'smokey' concentrations that are mixed into the urban environment. Some (O_3 , NO, NO_2 , and NMHCs) of these smoke-plume concentrations, after a specified time of travel, throughout a 24-hr period, are depicted in Figure 8.6.

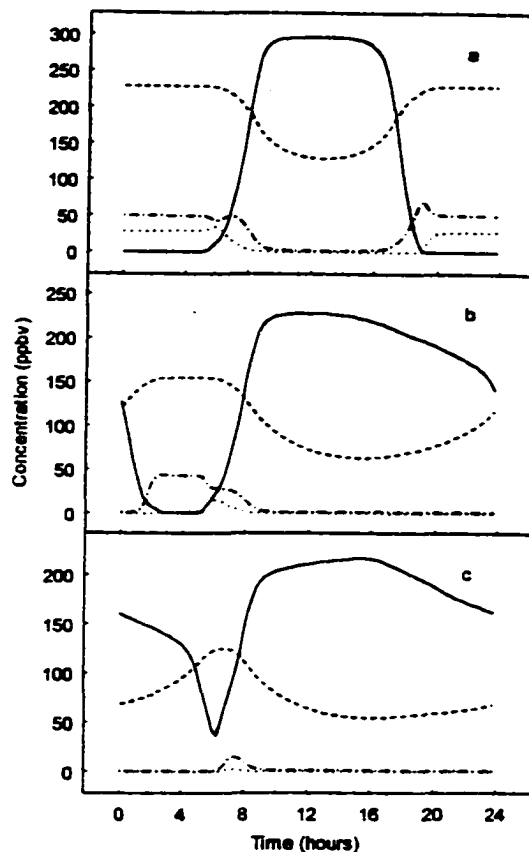


Figure 8.6 Concentrations of O_3 (solid lines), NO (dotted lines), NO_2 (dotted-dashed lines), and NMHCs (dashed lines) as a function of time of day, depending upon the length of processing time. Processing times are: (a) 3 hr; (b) 10 hr; (c) 15 hr. Traces show, in essence, two different regions depending upon the length of time the emissions were processed under the influence of daylight.

The basic shape of these traces is that of a step function with two distinct regions: a region of high $[O_3]$ and a region of low $[O_3]$. Each of these regions have associated high and low levels of other species. For example, the region of high $[O_3]$ has associated low levels of primary species, $[NO_x]$ and $[VOCs]$, but high levels of other secondary products (*e.g.*, OH , HNO_3 , etc.), and vice-versa for the low $[O_3]$ region. These regions are determined, in essence, by the extent to which the advected smoke emissions were processed under the influence of available sunlight. That is, advected emissions which were processed solely at

night will contribute high concentrations of NO_x and VOCs, with associated low levels of O_3 , owing to little chemical processing and leading to the low $[\text{O}_3]$ region (and vice versa for the high $[\text{O}_3]$ region owing to substantial photochemical processing).

8.C.1.b. Smoke Plume Time-of-Arrival

Given the diurnal variation of advected smoke-plume concentrations for three different travel times, a series of simulations were conducted that were designed to investigate the effect of the smoke plume upon the urban airshed as a function of smoke-plume arrival time. As mentioned earlier, the basic procedure for these simulations was to initiate an urban simulation and allow advection of the smoke plume into the urban environment on the third day. The advection of the smoke plume was accomplished by switching (at a given time) the wind concentrations from those of ambient conditions to those within a specifically aged smoke plume.

The effect of arrival time for every hour throughout a day was investigated for each of the three time-of-travel scenarios. Because O_3 is the species of primary importance in urban environments due to its detrimental effects on human and vegetative health, our analysis is focused on the impact of the smoke plume upon urban $[\text{O}_3]$. Figure 8.7 depicts the maximum in $[\text{O}_3]$ for days three and four of the simulations (*i.e.*, the day of arrival and the following day) as a function of time of arrival.

We notice, first of all, that the mixing of the smoke plume with the urban airshed always causes an increase in O_3 production; the longer the travel time, however, the less effect the smoke plume has. This most likely is due to photochemical processing and dilution of the smoke plume, both of which act to deplete the supply of radical species (as well as O_3 itself)

which the smoke plume provides to the urban environment. The $[O_3]$ maximum on the day of arrival of the smoke plume is only affected if the plume arrives previous to the time of the usual O_3 peak (*i.e.*, previous to ~ 3 pm) (Figure 8.7a). The $[O_3]$ maximum for the following day is consistently higher than the $[O_3]$ maximum for the arrival day, and shows little dependence upon the time of arrival, signifying that the urban airshed has once again reached a steady state (Figure 8.7b). While longer smoke plume processing times lead to smaller increases in O_3 production, the increases in $[O_3]$ for all investigated travel times are quite substantial.

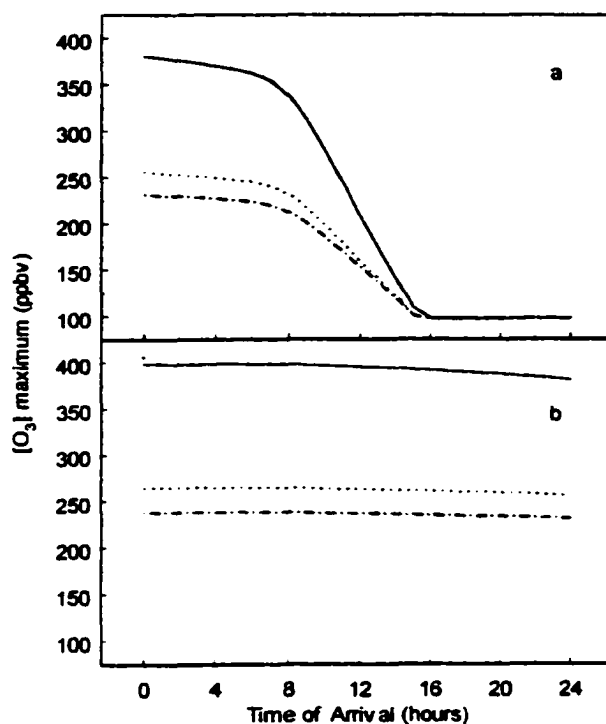


Figure 8.7 Daily $[O_3]$ maximum for an urban environment as a function of time-of-arrival of a smoke plume into the urban airshed based upon a 3 hr (solid line), 10 hr (dotted line), or 15 hr (dotted-dashed line) time-of-travel for the smoke plume. (a) $[O_3]$ maximum on the day of arrival; (b) $[O_3]$ maximum on the following day (given that smoke is continually advected into the urban environment). Traces show a general increase in maximum $[O_3]$ regardless of the time-of-travel for the smoke plume (provided that the smoke arrives previous to the time of the $[O_3]$ maximum).

8.C.1.c. Summary of the Effects of the Smoke on the Urban Airshed

We have investigated two primary variables in the advection of a smoke plume into an urban environment; that of the processing time that the smoke plume has experienced before reaching the city, and that of the time of arrival of the smoke plume into the urban airshed. We find that regardless of these two variables the introduction of 'smokey' air into an urban environment acts to increase O₃ production; although if the smoke arrives after the peak in [O₃] for that day, its effect is delayed until the following day. In fact, the impact of the smoke plume on O₃ production is generally greater the day after arrival than on the day of arrival, most likely due to the additional photochemical processing time. In a situation in which a fire continues to burn for several days, continuously supplying the city with advected 'smokey' conditions, it seems that the chemistry within the urban environment reaches an alternate steady state within a day or so. As an added note, some simulations were conducted using a wind speed of 5 mph, but the overall behavior was approximately the same as for the 1 mph simulations. These simulations are of greatest interest to forest managers and city officials in regard to prescribed, as well as natural, burns and their effect upon downwind urban communities and human health.

8.C.2. Effect of the City on the Smoke Plume

Because the variation of the PBL is accounted for in the urban simulations, but not in the smoke simulations, there is an added complexity in modeling the influence of the urban environment upon smoke-plume chemistry. That is, the urban model is an Eulerian (*i.e.*, fixed reference) box model which includes PBL height variation. However, the smoke plume simulations use a Lagrangian (*i.e.*, moving reference) model approximation in which the

modeled box is assumed to move with the boundary layer, as well as with the wind. These models were chosen to best fit the particular situation, but nevertheless combining them requires some consideration. The above situation (*e.g.*, the influence of the smoke plume on the city) is more easily adapted because it is only a matter of switching the advected air from 'normal' ambient air to 'smokey' air. From the viewpoint of the urban influence on smoke-plume chemistry, the adaptation is more complicated because the strength of the urban source emissions is regulated by the variation of the PBL height, but the PBL height variation is not accounted for in our smoke plume model.

To best accommodate this complication the scenario depicted in Figure 8.8 is chosen.



Figure 8.8 Schematic of the basic scenario for modeling the influence of the city on the smoke plume. Illustration shows simulation starting with the packet, initially containing biomass combustion emissions, being advected into an urban airshed and remaining for some period of time before being advected out. Notice that the moving packet only covers a portion of the fixed urban box model at any given point in time. [Adapted from Seinfeld and Pandis, 1998].

The smoke plume simulation is initiated as before (see section 7.C) beginning at midday. At 3 PM, when the PBL height variation as used in the urban simulations reaches and maintains its maximum (see Figure 6.1), a packet of processing smoke-plume emissions enters the city.

The box is assumed to cover only a certain percentage (10%) of the entire urban domain as it moves through and, as such, only that percentage of the urban source terms enter the box through its base. In addition to the added source emissions, the 'normal' ambient air concentrations which are used in the (horizontal) smoke plume dilution are switched to urban-air conditions during the period of time the packet is within city limits. At 6 PM the smoke plume is assumed to leave the city and the simulation returns to the standard smoke plume model described in section 7.C.

8.C.2.a. Simulated Effects

Simulated results for several tropospherically important species are shown in Figure 8.9. In these traces $[\text{HO}_2]$, $[\text{H}_2\text{O}_2]$ and [methyl-PAN] are used to exemplify all peroxy radicals, all hydroperoxides, and all PAN-species, respectively. They represent the primary constituents of these groups, and therefore embody a reasonable approximation to the temporal behavior of the group as a whole. Additionally, these traces show the temporal variation in concentrations for both the standard urban and standard smoke-plume simulations, as well as for the simulated effect of the city on the smoke-plume. In the following discussion we compare the 'smoke+city' simulation to the standard smoke-plume simulation in order to evaluate the effect of the urban environment on the smoke plume.

To begin, we notice that both the NMHCs (Figure 8.9a) and the total NO_x (Figure 8.9b) concentrations within the smoke plume are increased due to the influence of the urban emissions. This increase in the 'fuels' of tropospheric photochemistry leads to an increase in calculated $[\text{O}_3]$ (Figure 8.9c). As might be expected from simulations of the effect of the smoke on the city, the percentage increase in simulated O_3 is greater the day after the

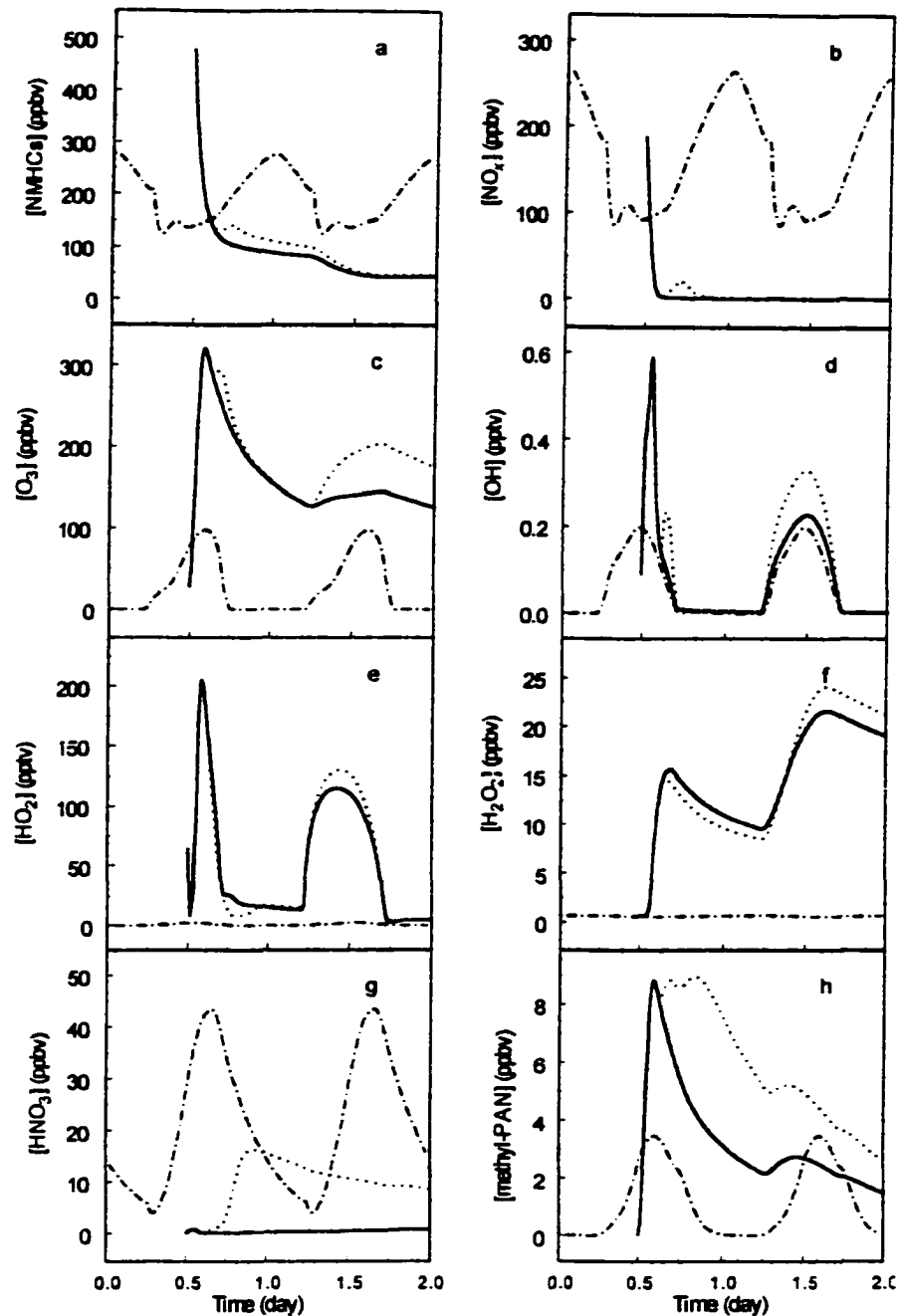


Figure 8.9 Influence of the urban airshed upon smoke-plume photochemistry (dotted lines), as represented by: (a) [NMHCs] (ppbv), (b) [NO_x] (ppbv), (c) [O₃] (ppbv), (d) [OH] (pptv), (e) [HO₂] (pptv), (f) [H₂O₂] (ppbv), (g) [HNO₃] (ppbv), (h) [methyl-PAN] (ppbv). The modeled smoke-plume is assumed to be advected into the urban environment at 3 PM and advected out at 6 PM on the first day. Traces also show temporal profiles for the standard smoke-plume model (solid lines) and the standard urban model (dotted-dashed line) for comparison.

introduction of the added emissions (when the modeled packet is actually no longer within the city) than at the time of introduction, presumably owing to added photochemical processing. The increase in O_3 production leads to a corresponding increase in $[OH]$ (Figure 8.9d), while the increase in $[NO_x]$ causes an initial decrease in $[HO_2]$ (Figure 8.9e) due to increased $Rad + NO_x$ reactions. This first-day decrease in $[HO_2]$ causes a corresponding decrease $[H_2O_2]$ (Figure 8.9f), although both peroxy radicals and hydroperoxides are increased by the second day when NO_x levels have again been depleted. This increase is also likely tied to the increase in VOC-loading and $[OH]$, the primary 'fuels' for peroxy radical formation. The previously mentioned increase in $Rad + NO_x$ reactions, owing to the sudden increased supply of NO_x from urban emissions, leads to an increase in NO_x -reservoir species, HNO_3 (Figure 8.9g) and PANs (Figure 8.9h).

8.C.2.b. Summary of the Effect of the City on the Smoke Plume

The urban environment overall acts to replenish NO_x concentrations within the smoke plume, causing photochemical processing conditions within the plume to switch to a more VOC-sensitive regime (*i.e.*, increased $Rad + NO_x$ termination reactions and decreased $Rad + Rad$ reactions) for a period of time. Eventually, however, as generally occurs in plume evolution, conditions return to NO_x -sensitive processing, but with increased 'fuel' loading, thereby leading to even further elevated concentrations of secondary species, such as O_3 , H_2O_2 , HNO_3 , and PANs, than is observed in our basic smoke plume models.

Chapter 9

Conclusions

9.A. Summary

We have been predominantly concerned with incorporating several oxygenated organic species into a model of biomass-combustion smoke-plume photochemistry. In doing so we found some interesting results which lead us to also investigate the impact of an urban environment upon smoke plume photochemistry. To these ends we developed two models, via modifications to the NCAR 'Master Mechanism,' in order to describe the temporal evolution of both a biomass combustion smoke plume and an urban airshed. In the case of the smoke plume, we chose to use a Lagrangian approximation, which simulates the temporal evolution of an initial set of concentrations within a modeled box domain that moves with the wind, as it is particularly suited for such a situation. On the other hand, an urban environment is spatially fixed and, as such, is more accurately modeled under an Eulerian approximation in which concentrations within a fixed modeling domain are simulated as wind is advected through the box and species emission and deposition are exchanged through the cell base. We have included additional terms to describe the diurnal variation of the planetary boundary layer in the urban airshed model and to describe the horizontal expansion of the plume in the smoke plume model.

9.B. Biomass Combustion Smoke Plume Simulations

9.B.1. Conclusions

We found the inclusion of the six dominant oxygenated organic species (CH_2O , CH_3OH , CH_3COOH , HCOOH , $\text{C}_6\text{H}_5\text{OH}$, and $\text{CH}_2(\text{OH})\text{CHO}$) into a smoke-plume model to lead primarily to an decrease in NO_x lifetime. This has important implications for the oxidizing capacity of the smoke-plume because NO_x catalyzes O_3 production and the availability of O_3 determines the oxidizing ability of the troposphere (through its role as the primary source OH radicals). Through analysis of species concentrations and reaction rates, it seems that the decrease in NO_x lifetime results from an increase in the production of radical species both through the tropospheric reaction cycle and through direct photolysis. The increase in the removal rate of NO_x and the production of radical species causes the transition from VOC- to NO_x -sensitive photochemistry to occur more quickly in the oxygenated smoke plume as compared to a smoke plume that does not include oxygenated organic species and also leads to an increase in the production of NO_x and HO_x reservoir species (*e.g.*, PANs and H_2O_2). This latter effect has important implications for regional and even possibly global tropospheric chemistry as these species may be transported over long distances before re-releasing their photochemically active reserves. The combination of these effects strongly indicates that the inclusion of oxygenated organic species, overlooked in previous biomass combustion smoke plume modeling, is a necessity in order to accurately account for the impacts of biomass combustion upon overall local-to-global tropospheric chemistry.

9.B.2. Further Work

On a whole our simulations of biomass combustion smoke plumes have provided the

first indications of the importance of oxygenated organic species in terms of smoke plume photochemistry and its impact upon the global troposphere. These results stem mostly from their effect upon NO_x concentrations, the catalyst of tropospheric photochemistry. These first indications, while intriguing, also appeal for further investigation. Improvements which could be made to the current model include, but are not limited to, the following. (1) Characterization and inclusion of the photochemistry of nitrophenols since the addition of the oxygenates, namely phenol, leads to their production. (2) Expansion of the hydrocarbon profile used here to include species of C_4 and greater. (3) Vertical stratification of the smoke-plume to account for the effect of plume 'haziness' on actinic (photon) flux infiltration (the model used here assumes clear-sky conditions, which is only strictly representative of the top of the smoke plume). (4) Variation of the planetary boundary layer height; this could most easily be accommodated within the vertically stratified smoke plume. (5) Integration of a model to describe aerosol chemistry into our current chemical mechanism. Considering the vast quantities of particulates, and therefore nucleation sites, emitted by combustion the inclusion of aerosol chemistry seems especially important for accurate modeling of smoke-plumes. (6) The development and implementation of techniques to reduce the photochemical mechanism since the current model is too computationally expensive to be available for use in larger, global models.

9.C. 'City plus Smoke' Simulations

9.C.1. Conclusions

The advection of a smoke plume into an urban environment replenishes the depleted NO_x concentrations, as well as providing additional [VOCs]. This increase in the 'fuels' of

tropospheric chemistry leads to an increase in the production of O_3 for both the smoke plume (even beyond the period of time that the smoke plume is within the urban airshed) and the urban environment. This has important implications for regional and global tropospheric chemistry. The increase in the oxidizing capacity within the smoke plume leads to an increase in the production of global NO_x and HO_x reservoir species, while the increase in O_3 production within an urban region can impact vegetative and human health. This latter effect is of particular importance to forest managers and city officials both for the planning of controlled burns or in the advising of residents downwind of natural burns.

9.C.2. Further Work

The implications of our simulations modeling the mixing between an urban environment and a smoke plume are of considerable ‘real-world’ interest, but, once again, provide only a first glance upon the reality of the situation. These results call for further investigations and monitoring. For example: (1) Investigations into the time scales of mixing between the smoke plume and the urban airshed. (There is an implicit assumption within our model that, once the plume has been advected in, the smoke is well-mixed across the entire urban airshed.) (2) Vertical stratification of the urban airshed to work in conjunction with the vertically stratified smoke plume. (3) Experimental verification of simulated ‘urban plus smoke’ conditions, including downwind urban plume measurements. (4) Development of a ‘look-up table’ for forest managers and city officials to aid in deciding the optimum conditions and times for planning prescribed burns.

9.D. Closing Remarks

Thousands of chemical species are continually being emitted from the Earth’s surface

and those with lifetimes less than about a year are destroyed within the troposphere. Understanding the chemistry that occurs within the troposphere is therefore a fundamental piece of understanding the interactions and transformations of matter within the natural world.

Fire is an integral part of this natural world as on any given day some part of the world is on fire. This burning of biomass is well-known to be an important source of trace gases and particulates into the atmosphere. Understanding the subsequent chemistry occurring due to this influx is, therefore, an integral part of understanding the chemistry of the troposphere as a whole. We believe our detailed photochemical modeling and analysis has provided further insight into the early photochemistry occurring within biomass combustion smoke plumes and their mixing with urban environments. It is our hope that this understanding provides a piece in building a solid foundation upon which future, larger, more accurate models are based.

Bibliography

- Anderson, H. E., Aids to determining fuel models for estimating fire behavior, *Gen. Tech. Rep. INT-122*, U. S. Department of Agriculture, Forest Service, Intermountain Forest and Range Experiment Station, Ogden, UT, 1982.
- Andreae, M. O., *et al.*, Biomass-burning emissions and associated haze layers over Amazonia, *J. Geophys. Res.*, *93*, 1509-1527, 1988.
- Andreae, M. O., A. Chapuis, B. Cros, J. Fontan, G. Helas, C. Justice, Y. J. Kaufman, A. Minga, and D. Nganga, Ozone and Aitken nuclei over equatorial Africa: Airborne observations during DECAFE 88, *J. Geophys. Res.*, *97*, 6137-6148, 1992.
- Andreae, M. O. B. E. Anderson, D. R. Blake, J. D. Bradshaw, J. E. Collins, G. L. Gregory, G. W. Sachse, and M. C. Shipham, Influence of plumes from biomass burning on atmospheric chemistry over the equatorial and tropical South Atlantic during CITE 3, *J. Geophys. Res.*, *99*, 12,793-12,808, 1994.
- Babbitt, R. E., D. E. Ward, R. A. Susott, W. M. Hao, and S. P. Baker, Smoke from western wildfires, 1994, In *Fire Management Under Fire (Adapting to change): Proceedings of the 1994 Interior West Fire Council Meeting and Program*, edited by K. Close and R. A. Bartlette, pp. 51-60, International Association of Wildland Fire, Fairfield, WA, 99012, 1998.
- Brasseur, G. P., J. J. Orlando, G. S. Tyndall, *Atmospheric chemistry and global change*, Oxford University, New York, NY, 1999.
- Chatfield, R. B., and A. C. Delany, Convection links biomass burning to increased tropical ozone: However, models will tend to overpredict O₃, *J. Geophys. Res.*, *95*, 18473-

18488, 1990.

Chatfield, R. B., J. A. Vastano, H. B. Singh, and G. W. Sachse, A general model of how fire emissions and chemistry produce African/oceanic plumes (O₃, CO, PAN, smoke) in TRACE-A, *J. Geophys. Res.*, *101*, 24279-24306, 1996.

Crutzen, P. J., and M. O. Andreae, Biomass burning in the tropics: Impact on atmospheric chemistry and geochemical cycles, *Science*, *250*, 1669-1678, 1990.

Crutzen, P. J., and G. R. Carmichael, Modeling the influence of fire on atmospheric chemistry, in *Fire in the Environment: The Ecological, Atmospheric and Climatic Importance of Vegetative Fires*, edited by P. J. Crutzen and J. G. Goldammer, pp. 89-105, Wiley & Sons, New York, NY, 1993.

Crutzen, P. J., Overview of tropospheric chemistry: Developments during the past quarter century and a look ahead, *Faraday Discuss.*, *100*, 1-21, 1995.

Csanady, G. T., *Turbulent diffusion in the environment*, D. Riedel, Hingham, MA, 1973.

DeGroot, W. F., W.-P. Pan, M. D. Rahman, and G. N. Richards, First chemical events in pyrolysis of wood, *J. Anal. Appl. Pyrolysis*, *13*, 221-231, 1988.

Delmas, R. A., A. Mareco, J. P. Tathy, B. Cros, and J. G. R. Baudet, Sources and sinks of methane in the African savanna, CH₄ emissions from biomass burning, *J. Geophys. Res.*, *96*, 7287-7299, 1991.

Fearnside, P. M., N. Leal, Jr., and F. M. Fernandes, Rainforest burning and the global carbon budget: Biomass, combustion efficiency, and charcoal formation in the Brazilian amazon, *J. Geophys. Res.*, *98*, 16,733-16,743, 1993.

Field, R. J., P. G. Hess, L. V. Kalachev, and S. Madronich, Characterization of oscillation

- and a period-doubling transition to chaos reflecting dynamic instability in a simplified model of tropospheric chemistry, *J. Geophys. Res.*, *106*, 7553-7565, 2001.
- Finlayson-Pitts, B. J., and J. N. Pitts, Jr., *Chemistry of the Upper and Lower Atmosphere*, Academic Press, San Diego, 2000.
- Fischer, W. C., Photo guide for appraising downed woody fuels in Montana forests, *Gen. Tech. Rep. INT-96*, U. S. Department of Agriculture, Forest Service, Intermountain Forest and Range Experiment Station, Ogden, UT, 1981.
- Fishman, J., and T. A. Carney, A one-dimensional photochemical model of the troposphere with planetary boundary-layer parameterization, *J. Atmos. Chem.*, *7*, 351-376, 1984.
- Fuller, M. *Forest fires: An introduction to wildland fire behavior, management, firefighting, and prevention*, Wiley & Sons, New York, 1991.
- Gaylor, H. P., *Wildfires: prevention and control*, Prentice-Hall, Maryland, 1974.
- Gear, C. W., *Numerical Initial Value Problems in Ordinary Differential Equations*, Prentice-Hall, New Jersey, 1971.
- Gifford, F. A., Horizontal diffusion in the atmosphere: A Lagrangian-dynamical theory, *Atmos. Environ.*, *16*, 505-512, 1982.
- Goode, J. G., R. J. Yokelson, R. A. Susott, and D. E. Ward, Trace gas emissions from laboratory biomass fires measured by open-path Fourier transform infrared spectroscopy: Fires in grass and surface fuels, *J. Geophys. Res.*, *104*, 21237-21245, 1999.
- Goode, J. G., R. J. Yokelson, D. E. Ward, R. A. Susott, R. E. Babbitt, M. A. Davies, and W. H. Hao, Measurements of excess O₃, CO₂, CO, CH₄, C₂H₄, C₂H₂, HCN, NO, NH₃,

- HCOOH, CH₃COOH, HCHO, and CH₃OH in 1997 Alaskan biomass burning plumes by airborne Fourier transform infrared spectroscopy (AFTIR), *J. Geophys. Res.*, *105*, 22,147-22,166, 2000.
- Griffith, D. W. T., W. G. Mankin, M. T. Coffey, D. E. Ward, and A. Riebau, FT-IR remote sensing of biomass burning emissions of CO₂, CO, CH₄, CH₂O, NO, NO₂, NH₃, and N₂O, in *Global Biomass Burning: Atmospheric, Climatic and Biospheric Implications*, edited by J. S. Levine, pp. 230-39, MIT Press, Cambridge, MA, 1991.
- Hao, W. M., and M.-H. Liu, Spatial and temporal distribution of tropical biomass burning, *Global Biogeochem. Cycles*, *8*, 495-503, 1994.
- Hao, W. M., D. E. Ward, G. Olbu, and S. P. Baker, Emissions of CO₂, CO, and hydrocarbons from fires in diverse African savanna ecosystems, *J. Geophys. Res.*, *101*, 23,577-23,584, 1996.
- Hindmarsh, A. C., ODEPACK: A systematized collection of ODE solvers, in *Scient. Comput.*, edited by R. S. Stepleman, pp. 55-64, North-Holland, Amsterdam, 1983.
- Hoffa, E. A. , D. E. Ward, W. M. Hao, R. A. Susott, and R. H. Wakimoto, Seasonality of carbon emissions from biomass burning in Zambian savanna, *J. Geophys. Res.*, *104*, 13,841-13,853, 1999.
- Holzinger, R., C. Warneke, A. Hansel, A. Jordan, W. Lindinger, D. H. Scharffe, G. Schade, and P. J. Crutzen, Biomass burning as a source of formaldehyde, acetaldehyde, methanol, acetone, acetonitrile, and hydrogen cyanide, *Geophys. Res. Lett.*, *26*, 1161-1164, 1999.
- Hough, A. M., The production of photochemical pollution in southern England and the effect

- of vehicle exhaust emission control strategies, *AERE REP R-12069*, Harwell Lab., London, 1986.
- Hurst, D. F., D. W. T. Griffith, and G. D. Cook, Trace gas emissions from biomass burning in tropical Australian savannas, *J. Geophys. Res.*, *99*, 16,441-16,456, 1994.
- Jacob, D. J., S. C. Wofsy, P. S. Bakwin, S.-M. Fan, R. C. Harriss, R. W. Talbot, J. D. Bradshaw, S. T. Sandholm, H. B. Singh, E. V. Browell, G. L. Gregory, G. W. Sachse, M. C. Shipham, D. R. Blake, and D. R. Fitzjarrald, Summertime photochemistry of the troposphere at high northern latitudes, *J. Geophys. Res.*, *97*, 16421-16431, 1992.
- Jacob, D. J., *et al.*, Origin of ozone and NO_x in the tropical troposphere: A photochemical analysis of aircraft observations over the south Atlantic basin, *J. Geophys. Res.*, *101*, 24235-24250, 1996.
- Jacobson, M. Z., *Fundamentals of atmospheric modeling*, Cambridge, New York, 1999.
- Keller, M., D. J. Jacob, S. C. Wofsy, and R. C. Harriss, Effects of tropical deforestation on global and regional atmospheric chemistry, *Clim. Change*, *19*, 139-158, 1991.
- Kleinman, L. I., Low and high NO_x tropospheric photochemistry, *J. Geophys. Res.*, *99*, 16831-16838, 1994.
- Kleinman, L. I., P. H. Daum, J. H. Lee, Y.-N. Lee, L. J. Nunnermacker, S. R. Springston, L. Newman, J. Weinstein-Lloyd, and S. Sillman, Dependence of ozone production on NO and hydrocarbons in the troposphere, *Geophys. Res. Lett.*, *24*, 2299-2302, 1997.
- Kley, D., Tropospheric chemistry and transport, *Science*, *276*, 1043-1045, 1997.
- Koppmann, R., A. Khedim, J. Rudolph, D. Poppe, M. O. Andreae, G. Helas, M. Welling, and

- T. Zenker, Emissions of organic trace gases from savanna fires in southern Africa during the 1992 Southern Africa Fire Atmosphere Research Initiative and their impact on the formation of tropospheric ozone, *J. Geophys. Res.*, *102*, 18879-18888, 1997.
- Lee, M., B. G. Heikes, and D. J. Jacob, Enhancements of hydroperoxides and formaldehyde in biomass burning impacted air and their effect on atmospheric oxidant cycles, *J. Geophys. Res.*, *103*, 13201-13212, 1998.
- Lephardt, J. O., and R. A. Fenner, Characterization of pyrolysis and combustion of complex systems using fourier transform infrared spectroscopy, *Appl. Spect.*, *34*, 174-185, 1980.
- Lewis, A. C., N. Carslaw, P. J. Marriott, R. M. Kinghorn, P. Morrison, A. L. Lee, K. D. Bartle, and M. J. Pilling, A larger pool of ozone-forming carbon compounds in urban atmospheres, *Nature*, *405*, 778-781, 2000.
- Lobert, J. M., D. H. Scarffe, W. M. Hao, T. A. Kuhlbusch, R. Seuwen, P. Warneck, and P. J. Crutzen, Experimental evaluation of biomass burning emissions: Nitrogen and carbon containing compounds, in *Global biomass burning: Atmospheric, climatic, and biospheric implications*, edited by J. S. Levine, pp. 289-304, MIT Press, Cambridge, Mass., 1991.
- Madronich, S., Photodissociation in the atmosphere 1: Actinic flux and the effects of ground reflection and clouds, *J. Geophys. Res.*, *92*, 9740-9752, 1987.
- Madronich, S., and J. G. Calvert, The NCAR master mechanism of gas phase chemistry- Version 2.0, *NCAR Tech. Note, NCAR/TN-333+STR*, National Center for Atmospheric Research, Boulder, Colo., 1989.

- Madronich, S., and J. G. Calvert, Permutation reactions of organic peroxy radicals in the troposphere, *J. Geophys. Res.*, *95*, 5697-5715, 1990.
- Mauzerall, D. L., D. J. Jacob, S.-M. Fan, J. D. Bradshaw, G. L. Gregory, G. W. Sachse, and D. R. Blake, Origin of tropospheric ozone at remote high northern latitudes in summer, *J. Geophys. Res.*, *101*, 4175-4188, 1996.
- Mauzerall, D. L., J. A. Logan, D. J. Jacob, B. E. Anderson, D. R. Blake, J. D. Bradshaw, B. Heikes, G. W. Sachse, H. Singh, and B. Talbot, Photochemistry in biomass burning plumes and implications for tropospheric ozone over the tropical south Atlantic, *J. Geophys. Res.*, *103*, 8401-8423, 1998.
- McKenzie, L., W. M. Hao, G. N. Richards, and D. E. Ward, Measurement and modeling of air toxins from smoldering combustion of biomass, *Environ. Sci. Technol.*, *29*, 2047-2054, 1995.
- Nance, J. D., P. V. Hobbs, L. F. Radke, and D. E. Ward, Airborne measurements of gases and particles from an Alaskan wildfire, *J. Geophys. Res.*, *98*, 14,873-14,882, 1993.
- Olcese, L. E., and B. M. Toselli, Fast and reliable numerical methods to simulate complex chemical kinetic mechanisms, *Int. J. Chem. Kinet.*, *30*, 349-358, 1998.
- Olson, J., *et al.*, Results from the intergovernmental panel on climatic change photochemical model intercomparison (PhotoComp), *J. Geophys. Res.*, *102*, 5979-5991, 1997.
- Penner, J. E., R. E. Dickerson, and C. A. O'Neil, Effects of aerosol from biomass burning on the global radiation budget, *Science*, *256*, 1432-1434, 1992.
- Poppe, D., M. Wallasch, and J. Zimmermann, The dependence of the concentration of OH on its precursors under moderately polluted conditions: A model study, *J. Atmos.*

- Chem.*, 16, 61-78, 1993.
- Poppe, D., R. Koppmann, and J. Rudolph, Ozone formation in biomass burning plumes: Influence of atmospheric dilution, *Geophys. Res. Lett.*, 25, 3823-3826, 1998.
- Pyne, S. J., *Fire in America: A cultural history of wildland and rural fire*, Princeton, New Jersey, 1982.
- Richardson, J. L., J. Fishman, and G. L. Gregory, Ozone budget over the Amazon: Regional effects from biomass burning emissions, *J. Geophys. Res.*, 96, 13073-13087, 1991.
- Ryan, P. W. , and C. K. McMahon, Some chemical and physical characteristics of emissions from forest fires, in *69th APCA Annual Meeting*, Air Pollut. Control Assoc., Portland, OR, June 27 - July 1, 1976.
- Schmidt, B., Missoula county environmental health department, 301 W. Alder, Missoula, MT 59802.
- Segar, K., Missoula city office of planning and grants, 435 Ryman, Missoula, MT 59802.
- Seinfeld, J. H., and S. N. Pandis, *Atmospheric chemistry and physics: From air pollution to climate change*, Wiley & Sons, New York, 1998.
- Sillman, S., J. A. Logan, and S. C. Wofsy, A regional scale model for ozone in the United States with subgrid representation of urban and power plant plumes, *J. Geophys. Res.*, 95, 5731-5748, 1990.
- Sillman, S., The use of NO_y, H₂O₂, and HNO₃ as indicators for ozone-NO_x-hydrocarbon sensitivity in urban locations, *J. Geophys. Res.*, 100, 14175-14188, 1995.
- Sillman, S., The relation between ozone, NO_x and hydrocarbons in urban and polluted rural environments, *Atmos. Environ.*, 33, 1821-1845, 1999.

- Singh, H. B., M. Kanakidou, P. J. Crutzen, and D. J. Jacob, High concentrations and photochemical fate of oxygenated hydrocarbons in the global troposphere, *Nature*, 378, 50-54, 1995.
- Stocks, B. J., B. W. von Wilgen, W. S. W. Trollope, D. J. McRae, J. A. Mason, F. Weirich, and A. L. F. Potgieter, Fuels and fire behavior dynamics on large-scale savanna fires in Kruger National Park, South Africa, *J. Geophys. Res.*, 101, 23,541-23,550, 1996.
- Stull, R. B., *An introduction to boundary layer meteorology*, Kluwer Academic, Dordrecht/Norwell, MA, 1988.
- Talbot, R. W., K. M. Beecher, R. C. Harriss, and W. R. Cofer III, Atmospheric geochemistry of formic and acetic acids at a midlatitude temperate site, *J. Geophys. Res.*, 93, 1638-1652, 1988.
- Tanner, R. L., A. H. Miguel, J. B. de Andrade, J. S. Gaffney, and G. E. Streit, Atmospheric chemistry of aldehydes: Enhanced peroxyacetyl nitrate formation from ethanol-fueled vehicular emissions, *Environ. Sci. Technol.*, 22, 1026-1034, 1988.
- Thompson, A. M., K. E. Pickering, D. P. McNamara, M. R. Schoeberl, R. D. Hudson, J. H. Kim, E. V. Browel, V. W. J. H. Kirchoff, and D. Nanga, Where did tropospheric ozone over southern Africa and the tropical Atlantic come from in October 1992? Insight from TOMS, GTE TRACE-A, and SAFARI 1992, *J. Geophys. Res.*, 101, 24251-24278, 1996.
- Trollope, W. S. W., L. A. Trollope, A. L. F. Potgieter and N. Zambatis, SAFARI-92 characterization of biomass and fire behavior in the small experimental burns in Kruger National Park, *J. Geophys. Res.*, 101, 23,531-23,539, 1996.

- von Salzen, K., H. G. Leighton, P. A. Ariya, L. A. Barrie, S. L. Gong, J.-P. Blanchet, L. Spacek, U. Lohmann, and L. I. Kleinman, Sensitivity of sulphate aerosol size distributions and CCN concentrations over North America to SO₂ emissions and H₂O₂ concentrations, *J. Geophys. Res.*, *105*, 9741-9765, 2000.
- Ward, D. E. , R. A. Susott, J. B. Kauffman, R. E. Babbitt, D. L. Cummings, B. Dias, B. N. Holben, Y. J. Kaufman, R. A. Ramussen, and A. W. Setzer, Smoke and Fire characteristics for cerrado and deforestation burns in Brazil: BASE-B experiment, *J. Geophys. Res.*, *97*, 14,601-14,619, 1992.
- Wayne, R. P., *Chemistry of Atmospheres* (2nd ed.), Oxford, Great Britain, 1991.
- Wennberg. P. O., *et al.*, Hydrogen radicals, nitrogen radicals, and the production of O₃ in the upper troposphere, *Science*, *279*, 49-53, 1998.
- Whitten, K. W., K. D. Gailey, and R. E. Davis, *General Chemistry*, Saunders, New York, 1988.
- Wofsy, S. C., G. W. Sachse, G. L. Gregory, D. R. Blake, J. D. Bradshaw, S. T. Sandholm, H. B. Singh, J. A. Barrick, R. C. Harriss, R. W. Talbot, M. A. Shipham, E. V. Browell, D. J. Jacob, and J. A. Logan, Atmospheric chemistry in the arctic and subarctic: Influence of natural fires, industrial emissions, and stratospheric inputs, *J. Geophys. Res.*, *97*, 16,731-16,746, 1992.
- Woodbury, G., *Physical Chemistry*, Brooks/Cole, California, 1997.
- Worden, H., R. Beer, and C. P. Rinsland, Airborne infrared spectroscopy of 1994 western wildfires, *J. Geophys. Res.*, *102*, 1287-1299, 1997.
- Yokelson, R. J., D. W. T. Griffith, and D. E. Ward, Open-path FT-IR studies of large-scale

- laboratory biomass fires, *J. Geophys. Res.*, *101*, 21067-21080, 1996a.
- Yokelson, R. J., D. W. T. Griffith, J. B. Burkholder, and D. E. Ward, Accuracy and advantages of synthetic calibration of smoke spectra, in *Optical Remote Sensing for Environmental and Process monitoring*, pp. 365-376, Air and Waste Manage. Assoc., Pittsburgh, PA, 1996b.
- Yokelson, R. J., D. E. Ward, R. A. Susott, J. Reardon, and D. W. T. Griffith, Emissions from smoldering combustion of biomass measured by open-path Fourier transform infrared spectroscopy, *J. Geophys. Res.*, *102*, 18865-18877, 1997.
- Yokelson, R. J., D. W. T. Griffith, R. A. Susott, and D. E. Ward, Spectroscopic studies of biomass fire emissions, in *Proceedings of the 13th Conference on Fire and Forest Meteorology*, vol. 1, pp. 183-196, Int. Assoc. of Wildland Fire, Fairfield, WA, 1998.
- Yokelson, R. J., J. G. Goode, D. E. Ward, R. A. Susott, R. E. Babbitt, D. D. Wade, I. Bertschi, D. W. T. Griffith, and W. M. Hao, Emissions of formaldehyde, acetic acid, methanol, and other trace gases from biomass fires in North Carolina measured by airborne Fourier-transform infrared spectroscopy, *J. Geophys. Res.*, *104*, 30109-30125, 1999a.
- Yokelson, R. J., R. A. Susott, R. E. Babbitt, D. E. Ward, and W. M. Hao, Trace gas emissions from specific biomass fire-types, in *START Synthesis Workshop on Greenhouse Gas Emission, Aerosols and Land Use and Cover Change in Southeast Asia*, edited by T. Moya, 60-68, SARCS, IGAC, LUCC, IGBP China-Taipei, Taipei, 1999b.